Synthesis and Analysis
of Thin Films
for Perovskite Solar Cells

Dissertation

Zur Erlangung des Grades
“Doktor der Naturwissenschaften“
im Promotionsfach Chemie

Am Fachbereich Chemie, Pharmazie und Geowissenschaften
der Johannes Gutenberg-Universität Mainz

Vorgelegt von

Alexander Klasen

geb. In Berlin

Februar 2020

Dekan Prof. Dr

Erster Berichterstatter

Zweiter Berichterstatter

Tag der mündlichen Prüfung

Eidesstattliche Erklärung

Die hier vorliegende Arbeit wurde im Zeitraum von Oktober 2015 bis März 2020 unter Leitung von [redacted] der Johannes Gutenberg-Universität Mainz und [redacted] am Max-Planck-Institut für Polymerforschung Mainz angefertigt.

Hiermit versichere ich an Eides statt, dass die vorliegende Arbeit selbstständig verfasst und nur unter Zuhilfenahme der im Literaturverzeichnis genannten Quellen angefertigt wurde.

Mainz, den 23.03.2020

Alexander Klasen

„Das habe ich noch nie vorher versucht,
also bin ich völlig sicher, dass ich es schaffe.“

Pippi Langstrumpf

Für meine Familie,
die nicht bei Verwandschaft endet.

Acknowledgments

First of all, I would like to thank [redacted] and [redacted], who gave me the opportunity to work not in one but in two inspiring groups. They provided me with a challenging and very interesting project and supported me with interesting and helpful discussions.

Furthermore, I would like to thank [redacted], who was an awesome supervisor who enriched me with invaluable and fascinating discussions abound science and beyond. I am thankful for the help and encouragement and an always-open door when help was needed. And special thanks for demonstrating tirelessly the practical and stylistic benefits of wearing slippers in the institute on a daily basis.

Thanks to [redacted] for the helpful, interesting and funny discussions and especially for accepting me as an honorary “[redacted]knecht”. Thanks for the contagious good mood and enthusiasm for scanning force microscopy, solar cells, or good drinks.

In that regard, I would also like to thank [redacted], who provided me with valuable help and discussions and proofread parts of my thesis.

I would like [redacted] and [redacted] for enriching my work with valuable help concerning the terahertz spectroscopy and being reliable and resourceful co-operation partners. In this regard, I would also like to thank [redacted] for the scientific help and discussions concerning x-ray photoelectron spectroscopy which resulted in very fruitful cooperation. Also thanks to [redacted] and [redacted], who also helped with the XPS measurements.

Thanks to the fantastic guys, who dared to work under my supervision, who enriched me in science and simple as great people.

Thanks to my buddy [redacted], for being a helpful and funny student assistant and doing his bachelor thesis with us. Thanks to [redacted], who not only provided a fascinating master thesis but also an abundance of inside jokes which made him truly one of my “favorite comrades.” Also thanks to [redacted], [redacted], [redacted] and [redacted] for the great help and fun during their internships.

Thanks to my fantastic colleagues at the [redacted], that became good friends and companions in misfortune when facing the ups and downs of the scientific world: [redacted], [redacted] and [redacted]. Especially cheers to my awesome office mates from the beginning: [redacted] You made the workplace a second home. And thanks to the people, who carry on the torch in our office: [redacted] You are worthy successors in both work and leisure time.

Special thanks also to [redacted], who kept on being an awesome guy.

I also would like to thanks the people from AK [redacted], who also made me feel welcome and being a part of their group, too, although I visited them far more scarcely than I wished for.

Thanks to [redacted], who are not only great guys but can also recognize the different emergencies when beer and when an ambulance is needed.

A special thanks also to [redacted] who are not only colleagues from the beginning but also great friends, and who again proofread my work.

Lastly, I would like to thank all my friends that became family over the years, my beloved brothers, their awesome wives, and my beloved mother. They carried me in difficult times and enriched the most beautiful moments even further. They were and are a blessing and fill my heart with joy.

Contents

Abstract

Perovskite solar cells belong to a novel generation of printable solar cells that are promising for future energy production due to high efficiency and low production costs. However, fast degradation and difficult reproducibility still prevent commercialization on a large scale and calls for further research of the interplay between the different components of such a cell.

Within this work, I present a guideline for how to synthesize state-of-the-art $MAPbI_3$ based perovskite solar cells (PSC) with a record efficiency of 19.5%. I elaborate a procedure for how to study the charge transport properties through different layers of PSC with conductive scanning force microscopy (cSFM) and focus on the semiconducting metal oxides layers $F:SnO_2$ and TiO_2. UV-ozone or plasma-treatment alters the surface properties and thus the local conductance perpendicular through these layers. Moreover, different plasma-treatments alter the migration properties of oxygen vacancies differently through an $F:SnO_2$ / TiO_2 interface. Lastly, I present how cSFM can be utilized as a synthesis tool for modifying the surface of semiconducting metal oxides locally.

In chapter 2, I exhibit the theory of perovskite solar cells and how the properties of the different layers influence the basic cell parameters, e.g. the short circuit current density J_{SC}, the open-circuit voltage V_{OC}, the fill factor FF and the efficiency. Moreover, I discuss that slow solvent evaporation of the perovskite precursor solvent hinders the reproduction of highly efficient solar cells and explain how different approaches target the issues. For the case of the compact electron transport layer TiO_2, I explored the limits of increasing the solar cell performance by minimizing film thickness. Furthermore, I present an optimized combination and adaptation of several reported recipes from literature for synthesizing $MAPbI_3$ based solar cells.

In chapter 3, I expound a procedure for measuring semiconducting metal oxides as $F:SnO_2$ and TiO_2 with a peak force based conducting scanning force microscopy (cSFM). When using this procedure, the influence of tip erosion on the measured current is negligible, even after measuring over 3 million individual force-distance curves on hard materials like metal oxides. Moreover, quantitative comparable cSFM measurements can be obtained to characterize different TiO_2 films that reproduce I-V characteristics of metal oxides on a local scale. Furthermore, I studied the decrease of the local conductance of TiO_2 thin films over time due to contamination in ambient conditions.

In chapter 4, I discuss the influence of different surface treatments on the local conductivity of $F:SnO_2$ and TiO_2 layers with cSFM. In particular, I demonstrated with X-ray photoelectron spectroscopy how surface defects like fluorine dopants and oxygen vacancies are affected by UV-ozone treatment, oxygen-plasma treatment or argon-plasma treatment. Terahertz spectroscopy measurements confirm that bulk properties of thin films remain virtually unaffected by surface treatments. Based on these insights, I present an easy procedure for increasing the local conductance of $F:SnO_2$ substrates and TiO_2 thin films by up to two orders of magnitude with UV-ozone treatment.

In chapter 5, I demonstrate how the surface of TiO_2 and $F:SnO_2$ can be locally patterned with cSFM. Consecutive cSFM measurements on the same area induce local charges under the cantilever tip. Local changes in the work function also occur in humid conditions that quench surface charges, as verified with Kelvin probe force microscopy. In the second part of chapter 5, I demonstrate that oxygen plasma treatment of $F:SnO_2$ substrates creates an undoped SnO_2 interlayer that acts as an additional electric resistance at the $F:SnO_2$ / TiO_2 interface. Argon-plasma treatment removes an undoped SnO_2 interlayer. In TiO_2 thin films, surface-oxygen vacancies provide electrical pathways for electrons across the TiO_2 surface and lead to non-local surface charging with consecutive cSFM measurement. Bulk oxygen-vacancies can migrate through the $F:SnO_2$ / TiO_2 interface. As a consequence, I demonstrate a switchable electric resistance of an $F:SnO_2$ / TiO_2 array.

In conclusion, my work provides an overview of the basics of perovskite-based solar cells and a guideline for how to synthesize $MAPbI_3$ based solar cells. I identify eight different effects that occur when measuring the local conductance of semiconducting metal oxides with cSFM and discuss how these effects could be used in future applications.

Zusammenfassung

Perovskitsolarzellen (*perovskite solar cells,* PSC) gehören zu einer neuen Generation von druckbaren Solarzellen, die aufgrund hoher Effizienzen und geringer Produktionskosten zu vielversprechenden Kandidaten für eine zukünftige Stromversorgung gehören. Jedoch verhindern eine schnelle Degradation und eine schwierige Reproduzierbarkeit bisher eine großtechnische Kommerzialisierung. Es besteht daher der Bedarf nach einem tieferen Verständnis für die Wechselwirkung der verschiedenen Komponenten einer solchen Zelle.

Im Rahmen meiner Arbeit präsentiere ich einen Leitfaden zur Synthese $MAPbI_3$ basierte Solarzellen mit einer Rekordeffizienz von 19.5 %. Ich demonstriere, wie der Ladungstransport durch verschiedene Schichten von PSC untersucht werden kann mittels leitfähiger Rasterkraftmikroskopie (*conducting scanning force microscopy,* cSFM). Hierbei fokussierte ich mich auf die beiden halbleitenden Metalloxide $F:SnO_2$ und TiO_2. UV-Ozon- oder Plasma-Behandlung modifizieren die Oberflächeneigenschaften dieser Oxide und beeinflussen damit die Leitungseigenschaften senkrecht durch die entsprechende Schicht. Verschiedene Plasmabehandlungen haben einen unterschiedlichen Einfluss auf die Migration von Sauerstofffehlstellen durch die $F:SnO_2$ / TiO_2 Grenzfläche. Schließlich demonstriere ich, wie cSFM als ein Synthesewerkzeug eingesetzt werden kann, um die Oberfläche von Metalloxiden lokal zu manipulieren.

Kapitel 2 umreißt die Grundlagen zu Perovskitsolarzellen und wie die Eigenschaften der verschiedenen Schichten die Kurzschlussstromdichte (short circuit current density) J_{SC}, die Leerlaufspannung (open-circuit voltage) V_{OC}, den Füllfaktor FF und die Effizienz einer Solarzelle beeinflussen. Darüber hinaus lege ich dar, wie eine langsame Verdampfung des Perowskitpräkursor-Lösungsmittels die Synthese von effizienten Solarzellen behindert. Anschließend biete ich einen Überblick verschiedener Ansätze aus der Literatur, um diese

Problematik zu umgehen. Am Beispiels der Elektronenstransportschicht TiO_2 untersuchte ich die Grenzen der Optimierung einer Perowksitsolarzelle durch bloße Minimierung der Schichtdicke. Außerdem präsentiere ich eine optimierte Kombination und Adaption verschiedener Ansätze aus der Literatur zur Synthese $MAPbI_3$ basierter Solarzellen.

Im Kapitel 3 präsentiere ich eine Anleitung zur Messung halbleitender Metalloxidschichten wie $F{:}SnO_2$ und TiO_2 mittels Kraft-Abstandskurven basierter cSFM. Dieser Ansatz minimiert die Spitzenerosion des Cantilevers beim Vermessen harter Oberflächen wie Metalloxide und ermöglicht vergleichbare Strommessungen selbst nach über 3 Millionen Kraft-Abstandskurven. Darüber sind quantitativ vergleichbare cSFM Messungen zugänglich, um verschiedene TiO_2 Schichten zu charakterisieren und Strom-Spannungskennlinien auf lokaler Ebene reproduzieren zu können. Darüber hinaus erforsche ich den Abfall der lokalen Leitfähigkeit von TiO_2 Dünnschichten über mehrere Stunden aufgrund von Oberflächenkontamination in Umgebungsbedingungen.

In Kapitel 4 untersuche ich den Einfluss verschiedener Oberflächenbehandlungen auf die lokale Leitfähigkeit von $F{:}SnO_2$ und TiO_2 Schichten mittels cSFM. Zusätzlich verwendete ich Röntgenphotoelektronenspektroskopie (*X-ray photoelectron spectroscopy*, XPS) um zu untersuchen, wie Oberflächendefekte wie Sauerstofffehlstellen oder Fluor-Dotierungen beeinflusst werden durch UV-Ozon-Behandlung, Argon-Plasmabehandlung oder Sauerstoff-Plasmabehandlung. Terahertz Spektroskopie Messungen bestätigen, dass die Bulk-Eigenschaften dieser Dünnfilme nach Oberflächenbehandlungen unverändert bleiben. Basierend auf diesen Beobachtungen präsentiere ich eine einfache Vorschrift, um die lokale Leitfähigkeit von $F{:}SnO_2$ Substraten and TiO_2 Dünnschichten um bis zu zwei Größenordnungen zu erhöhen.

Im Kapitel 5 beschreibe ich, wie die Oberfläche von TiO_2 and $F{:}SnO_2$ mittels cSFM lokal modifiziert werden kann. Aufeinanderfolgende cSFM Messungen erzeugen Oberflächenladungen örtlich begrenzt unter der Cantileverspitze. Eine lokale Änderung der Austrittsarbeit ist auch bei einer hohen Luftfeuchtigkeit mittels Kelvin-Sonde-Kraftmikroskopie (*kelvin probe force microscopy*, KPFM) nachweisbar, obwohl Oberflächenladungen durch Wasser ausgelöscht werden. Im zweiten Teil des Kapitel 5 demonstriere ich, dass Sauerstoff-Plasmabehandlung eine dünne Zwischenschicht aus undotiertem SnO_2 erzeugt, die einen zusätzlichen elektrischen Widerstand an der $F{:}SnO_2$ / TiO_2 Grenzfläche verursacht. Argon-Plasmabehandlung entfernt solch eine undotierte SnO_2 Schicht. Darüber hinaus zeige ich, dass Oberflächen-Sauerstofffehlstellen einen Leitungspfad für Elektronen auf TiO_2 Dünnschichten erzeugen. Dadurch wird Ladung parallel über die Oberfläche transportiert wird und die Oberfläche wird nicht nur örtlich begrenzt aufgeladen. Außerdem können Sauerstofffehlstellen durch die $F{:}SnO_2$ / TiO_2 Grenzfläche migrieren. Als Folge demonstriere ich einen schaltbaren elektrischen Widerstand einer TiO_2 Dünnschicht auf einem $F{:}SnO_2$ Substrat.

Zusammengefasst liefert meine Arbeit einen Überblick über die Grundlagen von Perowskitsolarzellen und einen Leitfaden zur Synthese $MAPbI_3$ basierter Zellen. Ich identifizierte acht verschiedene Effekte, die während einer cSFM Messung auftreten können und diskutiere Anwendungsmöglichkeiten für diese Effekte.

Chapter 1: Introduction

We as a species reached a new millennium and look back on an over 12.000 year-long history since first civilization emerged.[1] We form complex societies that made a sophisticated division of labor necessary and shaped our world so drastically, that some even would call the present geologic era as “man-made”, the Anthropocene. We achieved much. From several agriculture revolutions to modern gene-therapy based approaches to cure cancer, modern technology almost tripled the average human life span from 33 years in paleolithic times to an average of 82.6 years in Japan in 2019. We span a global web of ultrafast, digital communication, that allows us to transfer entire libraries over continents within a split second. We set foot on extraterrestrial soil.

Yet, despite all these wonderous achievements, one thing remains unchanged: Since the dawn of mankind, we burn carbon-containing materials to enable heating, electricity, mobility, etc. for energy. From the archaic campfire to modern coal power plants, we burn resources to fuel our daily life. In 2017 the primary energy consumption consisted of over 85 % of fossil carbon-based energy sources like coal, natural gas, and oil. This use of fossil energy gives rise to a multitude of problems.

The first problem is quite obvious. Fossile coal, gas and oil do not regrow. Or at least, regrowth does not occur in a relevant time frame, hence the adjectives “fossil”. And we consume these finite resources incredibly fast.

In a study from 2015, H. Mohr et al. analyzed the global energy production as well as the known and potential deposits for fossil energy carriers. They estimated a “low“- and “best-guess scenario” for the global fossil fuel production.[2] Even the best guess scenario predicted a soon-to-come shortage since the production may already peak before the year 2025 and continuously decline after that (Figure 1). Since numerous basic chemicals derive from oil, that are needed for goods and daily life products like polymers, dyes, glue, drugs and many others, a shortage of these basic chemicals might threaten our living standard.

Therefore, for future energy supply, a renewable source is needed.

Another main problem associated with burning carbon-based materials on the large-scale has gained much attention within the last years. The human-caused emission of carbon dioxide changes the earth’s atmosphere and causes climate change.[3] Since the beginning of the industrial revolution, human energy consumption increased the concentration of CO_2 in the atmosphere from 280 ppm to over 400 ppm.[4] Carbon dioxide acts as a greenhouse gas due to its ability to absorb infrared radiation from the sun, that otherwise would be reflected back into space.[3] Among climate scientists, over 90 % share the consensus that this human-made increase of carbon dioxide in earth’s atmosphere causes recent global warming.[5]

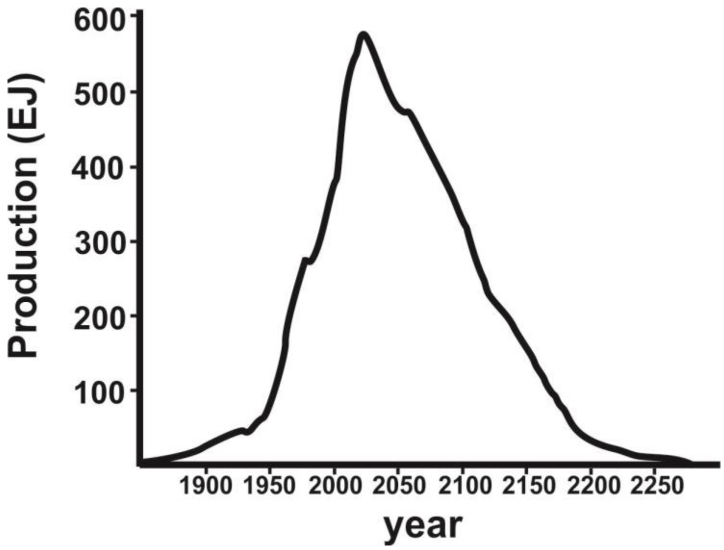

Figure 1: "best-guess" scenario of global fossil fuel production. [2]

With a rising world population and increasing energy consumption in developing countries, additional and renewable energy sources are desperately needed. Solar power can be one way to feed the evergrowing world hunger for energy. Lewis et al. pointed out that approximately $4.3 \cdot 10^{20}$ J of solar energy reaches the earth's surface in merely one hour, which exceeded the annual worldwide primal energy consumption of $4.1 \cdot 10^{20}$ J (2001).[6]

However, one popular argument against solar power is its price. Solar cells are believed to be too expensive to compete with other means of energy production. Especially monocrystalline silicon solar cells require several energetically expensive production steps like an elaborate purification and crystal growth technique. Nevertheless, this argument is not true anymore. Within the last decade, a remarkable decline in the price of solar cells occurred. One way of comparing the price of electric power quantitatively is the so-called levelized costs of electricity (LCOE). The LCOE aims to compare quantitatively the price per kilowatt-hour for different means of energy production. It is defined as the sum of costs over the lifetime divided by the sum of electrical energy produced over the lifetime.[7] Thus, LCOE increases with increasing initial investment costs, maintenance and fuel expenditures and decreases with longer lifetime and generated energy.

A recent study from the Fraunhofer Institute in Freiburg compared the LCOE of different means of energy production in Germany.[8] The authors found a broad range of LCOE for photovoltaic systems (PV) from 11.54 $€_{\text{Cents}}$ / kWh in northern Germany for small rooftop systems to 3.71 $€_{\text{Cents}}$ / kWh in southern Germany for ground-mounted utility-scale systems (Figure 2).[8] While small rooftop systems still exhibit higher production costs than fossil energy production as brown coal and hard coal, utility-scale systems are already able to outcompete any other technology.

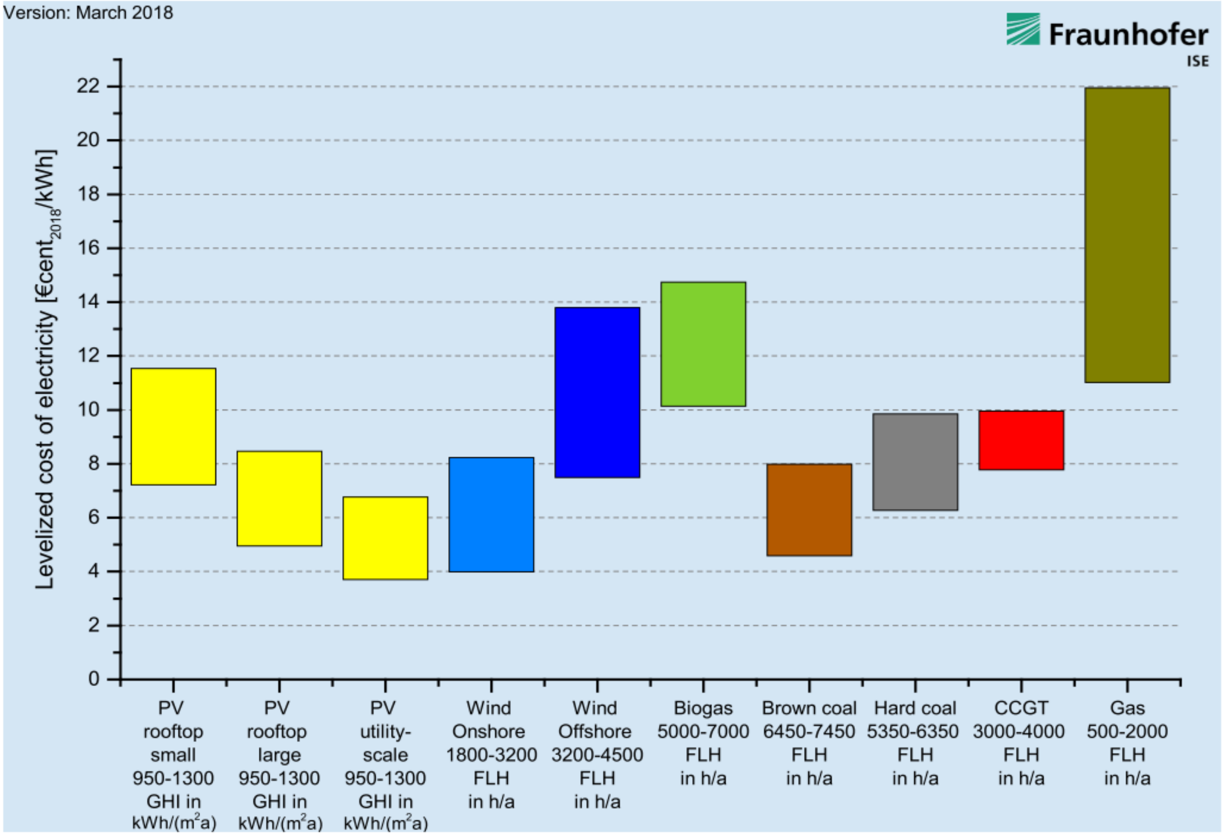

Figure 2: "LCOE of renewable energy technologies and conventional power plants at different locations in Germany in 2018".[8] The comparison covers photovoltaic systems (PV), wind turbines, biogas, brown coal or lignite, hard coal, combined cycle power plants (CCGT) and fossil methane gas.

Perovskite solar cells (PSC) are a novel class of thin-film solar cells that could be a route to mass-producing cheap and efficient solar cells that could a leading role in our energy supply.

Since the first report of a perovskite solar cell in 2009, the scientific community witnessed an unprecedented rise of record efficiency over the last decade from a few percents to 25.2 % in 2019 (Figure 3, red curve with yellow dots).[9,10] In comparison, silicon-based solar cells were first reported in 1941 and it took almost 80 years to increase the efficiency from less than 1 % to 26.1 % (Figure 3, blue curve with filled squares).[11] Moreover, in contrast to classic silicon-based solar cells, every functional layer of these highly efficient solar cells is solution-processable which renders these cells printable in a "role-to-roll" approach at low production costs.[12] Since 2018, record perovskite solar cell efficiency outperformed all other thin technologies as CIGS (copper indium gallium selenide) and CdTe based cells (Figure 3, green curves). These prerequisites might enable the mass production of extremely low-cost solar cells.

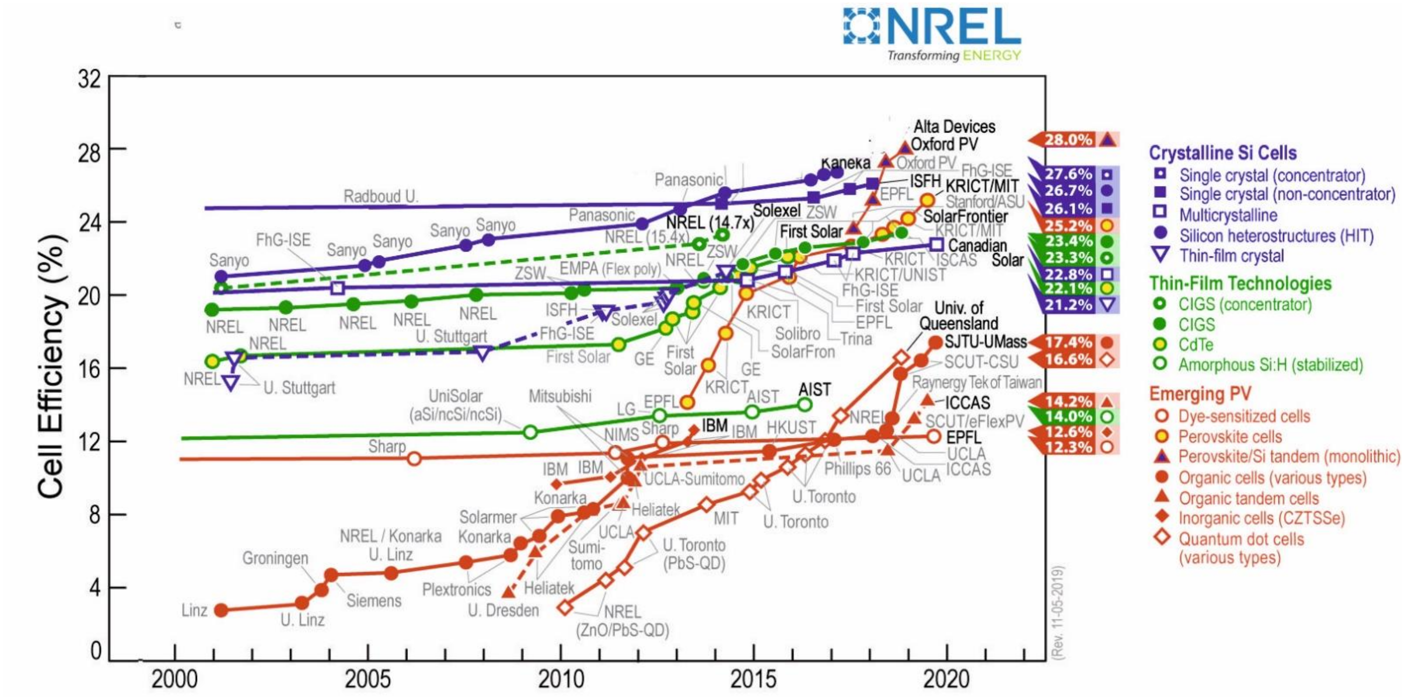

Figure 3: Cropped section of the NREL record efficiency chart (Dec. 2019).[10]

However several issues have to be overcome in order to pave the way for mass production.

One major obstacle is the challenging reproducibility which is reflected in a broad distribution in solar cell efficiency for the same recipe.[13] In chapter 2, I discuss the major obstacles for synthesizing homogeneous and reproducible perovskite solar cells and how to overcome these obstacles. Furthermore, I present a thorough adaptation of different synthesis routines in order to solar cell efficiency up to 19.5 % for $MAPbI_3$.-based solar cells.

Another challenge is the need for improved stability of perovskite solar cells.[14] Recent publications underline the crucial role the different interfaces play for perovskite solar cells.[15] Interface properties determine the charge migration through the perovskite layer and can cause unwanted internal reactions.[16,17] Yet, further understanding of the role of interfaces is needed. In chapter 3, I discuss how cSFM is suited to investigate the charge transfer characteristics of surfaces and interfaces of different layers of a perovskite solar cell. Moreover, I present a routine for how to quantitatively compare the local conductance of semiconducting metal oxides as fluorine-doped tin dioxide and titanium dioxide.

In chapter 4, I demonstrate how the interface transport properties of $F:SnO_2$ and TiO_2 films can be easily modified with simple, clean and easy plasma or UV-ozone treatment and how this affects the solar cell efficiency.

In chapter 5, I demonstrate, that surface modification also alters the transport properties for oxygen vacancies within the layers. I present how the modification of metal oxide surfaces can be applied for applications beyond solar cells. Furthermore, I investigate, how cSFM can be applied beyond pure analytic application and serve as a synthetic tool in modifying local electronic characteristics.

Therefore, my work presents a toolbox for synthesizing and analyzing thin films for perovskite solar cells and understanding the role of interfaces for transport characteristics through the layers. The presented synthesis and analysis can be adopted for related energy applications that apply an array of semiconducting metal oxide layers like light-emitting photodiodes, thin-film transistors, and memristors.

Chapter 2: The Perovskite Solar Cell - Fundamentals and Synthesis

2.1 Introduction

Perovskite solar cells (PSC) are part of the family of thin-film solar cells that first have been published in 2009 by A. Kojima et al.[18] Their fundamental advantage to other solar cells is the promise of cheap and facile fabrication of PSC. In contrast to classic monocrystalline or polycrystalline silicon solar cells, the precursors for PCS do not require an energetic intensive purification step and ultra-pure quality.[19] Other thin-film technologies like copper indium gallium selenide solar cells, cadmium telluride or gallium arsenide require rare and expensive elements, whereas perovskite solar cells only consist of earth-abundant elements. One of its main components is lead, which is cheaper than silver, copper and even nickel, tin and zinc.[20] Another advantage of PSC is the printability of each component, which enables fast and easy roll-to-roll processes.[13]

This chapter is aiming to provide the necessary fundamentals for understanding perovskite solar cells and gives context for the research I am presenting in my work. Furthermore, I display how to synthesize each layer of state-of-the-art $MAPbI_3$ based perovskite solar cell.[1]

2.2 The working principle of a solar cell

The perovskite solar consists of the cathode, an electron transport layer, a photon-absorber, a hole transport layer, and the anode.

The perovskite solar cell is a layered system where each component conducts a different role. The eponymous element of PSC is the central perovskite layer (Figure 4, green layer). It absorbs visible light and promotes an electron from the valance band into the conduction band (Figure 4 b). Both the excited electron and the remaining hole on the valance band can migrate through the perovskite layer until they reach its boundaries. The photon-absorbing layer is sandwiched between two neighboring “transport layers” or “charge-selective layers”. One layer exclusively conducts electrons and thus is called the “electron transport layer” (ETL; gray layer in Figure 4). The other layer solely transports holes and is accordingly called the “hole-transport layer” (HTL, red layer in Figure 4).

---

[1] It has to be noted, that parts of the following chapters, especially the preparation of the individual layers, is based on my publication from 2019.[52]

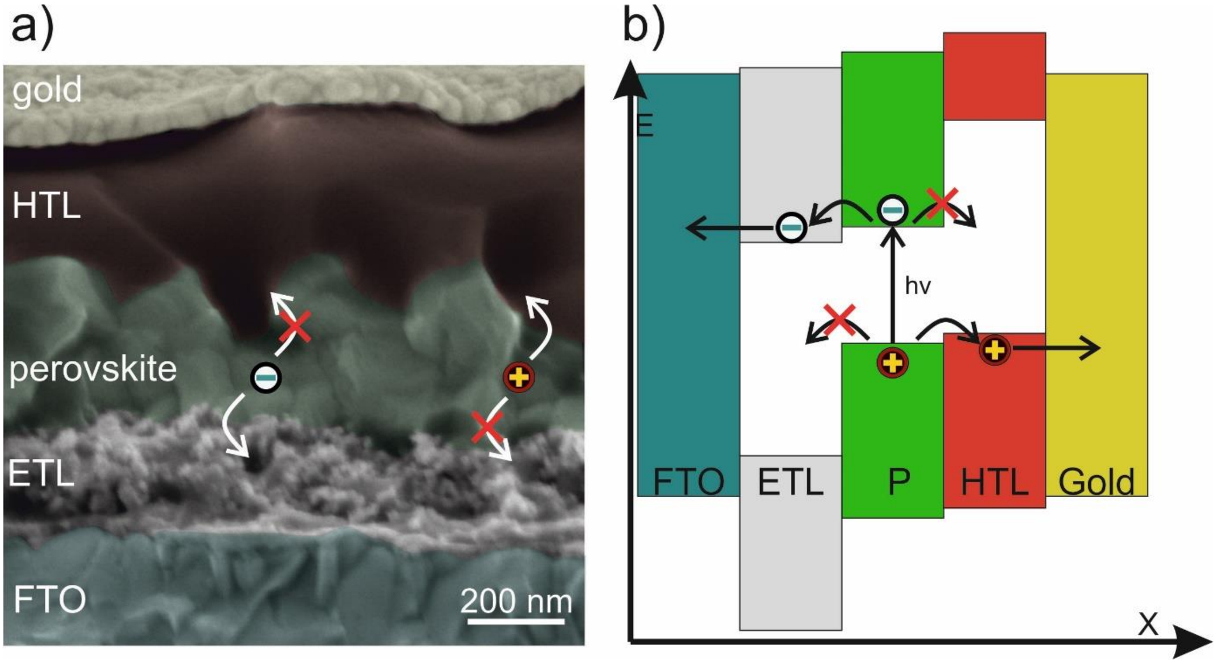

Figure 4: a) General structure of a perovskite solar cell, demonstrated on a colored SEM image. The lowest layer, the bottom electrode, is composed of fluorine-doped tin oxide (FTO; teal layer) and acts as a foundation for every other layer. The FTO substrate is covered with an electron transport layer (ETL; gray layer) followed by the photon-absorbing perovskite-layer (green layer). The next layer, the hole transport layer (HTL; red layer) is covered with the top electrode, a thin gold film (yellow layer). b) Band diagram of a perovskite solar cell. Light passes through the FTO layer and the ETL and is absorbed by the perovskite layer (green), where an electron is promoted from the valence band into the conduction band. Excited electrons can migrate into the conduction band of the electron transport layer. Since the hole transport layer has no corresponding energy level, that layer act as an electron blocking layer. The photon-generated electrons migrate from the ETL into the bottom electrode, the FTO. The remaining hole in the valence band of the perovskite layer is filled with electrons from the valence band of the hole transport layer. This process corresponds to migration of holes from the perovskite layer into the hole transport layer (red). Since the ETL has no corresponding energy level, that layer acts as a hole blocking layer. The holes migrate from the HTL into the gold electrode.

Next to the ETL is the bottom electrode, which in most cases is composed of fluorine-doped tin oxide F:SnO_2 (FTO, Figure 4 teal layer). Electrons are transported into the FTO, which acts as the anode. Next to the HTL is the top electrode, which is mainly a thin gold film (Figure 4, yellow layer). It collects the holes and thus acts as the cathode.

In literature, four main parameters are used to quantify the properties of a solar cell:

- The open circuit potential V_{OC},
- The short circuit current density J_{SC},
- The fill factor FF,
- The conversion efficiency η.

These parameters are determined with a J-V-measurement (Figure 5). For such a measurement, the solar cell is illuminated with a calibrated spectrum and intensity (AM1.5G standard; with an incident power density of 100 mW /cm^2). Simultaneously, an external bias is applied while the current is measured. The current plot over the applied bias is called the J-V-curve.

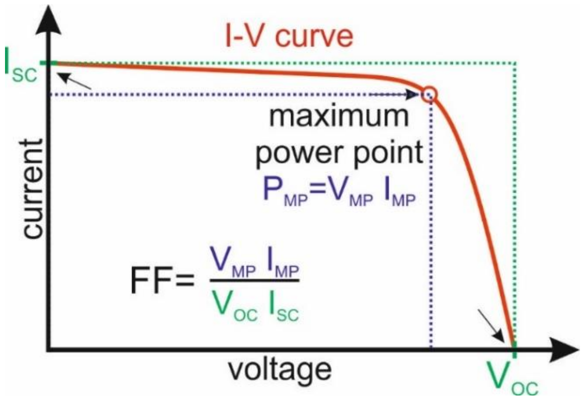

Figure 5: The I-V curve of a solar cell.

V_{OC}, J_{SC}, FF, and η are extracted from the I-V curve and will be explained in more detail below.[21] Further detail on how an I-V-curve was conducted is given at the end of this chapter.

2.2.1 The short circuit current I_{SC}

The short circuit current I_{SC} is the maximum current, a cell provides at zero electric load.

The first parameter for quantifying the solar cell performance is the short circuit current I_{SC}.[21] It describes the current a solar cell provides at short circuit conditions with zero electric load. I_{SC} is proportional to the number of generated free charge carriers. In general, the more light is absorbed, the more free charge carriers are created and thus the higher the short circuit current is. Several factors influence the absorption of light and generation of charge carriers:

- **The area of the solar cell:**
  The larger the active area of a solar cell is, the more light is absorbed. Accordingly, more charge carriers are created and I_{SC} increases. In order to compare cells independent of their respective area, the short-circuit density is normalized. Dividing I_{SC} by the active area yields the short-circuit current density J_{SC}. During this work, the active area was defined by a shadow mask with a 3 x 3 mm² hole.
- **The light source:**
  The intensity and energetic spectrum of the light source influence the generation of charge carriers. The higher the incident intensity and fraction of shorter wavelengths in the spectrum, the more light is absorbed. For comparison, a standardized intensity of 100 mW/cm_2 with a standardized AM 1.5G spectrum similar to the solar spectrum is applied.
- **The bandgap:**
  The major material property of the solar cell that influences J_{SC} is the optical bandgap of the photon-absorber. More photons are absorbed and have sufficient energy to

promote an electron from the valence band to the conduction band the smaller the bandgap is. Thus, J_{SC} increases with a decreasing bandgap.

- The collection probability:
  The probability, that light interacts with the solar cell and is consequentially absorbed is called the collection probability. It is determined by the attenuation coefficient of the absorber material and its thickness. Thus, the higher the coefficient and the thicker the absorber material, the higher I_{SC} is.
- The optical properties:
  Reflection and refraction both influence the solar cell performance. In commercial silicon-based solar cells, antireflective coatings are used to minimize optical losses due to reflection at the air/cell interface. Shading of the photon-absorber by other components of the solar cell also affects the J_{SC}. Therefore, every layer that is before the photon-absorber in the path of the incident light must be as transparent as possible.
- Losses mechanisms
  Several issues can occur in a perovskite solar cell that causes a low J_{SC}. A high electric resistance within the solar cell or at the contacts reduces the measured current. Moreover, the recombination of charge carriers at defects within the perovskite layer or at the interfaces reduce the short circuit current density.

2.2.2 The open cell voltage V_{OC}

The open cell voltage describes the maximum voltage, a cell provides at open-circuit conditions.

Another key parameter of solar cells is the open cell voltage V_{OC}. [21] It describes the maximum potential difference, that a solar cell generates at zero current (e.g. at open circuit conditions).

The optical bandgap of the absorber:

The main limitation of the V_{OC} is the bandgap of the photon-absorber. The higher the bandgap of the absorber is, the higher the potential difference between both electrodes can be and thus the larger the V_{OC} becomes. Therefore, maximum efficiency requires a trade-off between a large band for high V_{OC} and a small bandgap to enable high J_{SC}.

The Shockley-Queisser-limit

Schockley and Queisser calculated the upper theoretical limit for solar power conversion efficiency as a function of the bandgap and found a maximum conversion efficiency for a bandgap of 1.0-1.5 eV (Figure 6).[22]

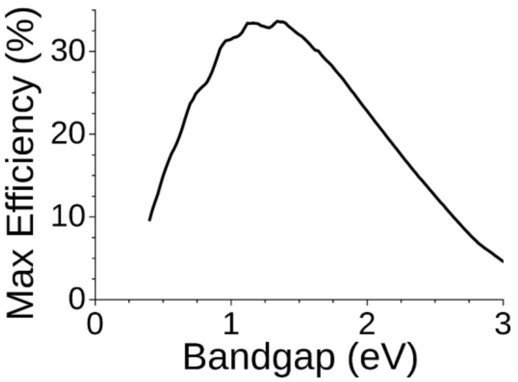

Figure 6: The maximum power conversion efficiency of solar cells as a function of the bandgap of the photon-absorber.[22]

Such a bandgap represents an optimal tradeoff for maximum V_{OC} and J_{SC} and is determined by the solar spectrum, the relative intensities and absorption and light scattering of the atmosphere. The maximum efficiency a solar cell can achieve with one absorber is around 33%. This circumstance is called the Shockley-Queisser-limit. However, so-called tandem solar cells with two or more absorbers can have higher efficiency.

The band alignment of the charge selective layers

However, in real devices, the band alignment of the charge selective layers determines the actual V_{OC}, too.

For Perovskite solar cells, the V_{oc} is limited by the potential difference of the upper valence band edge of the hole transport layer and the lower conduction band edge of the electron transport layer (Figure 7)[23].

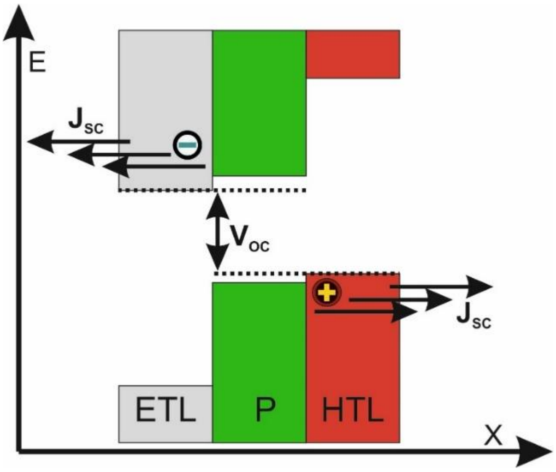

Figure 7: The dependence of the V_{OC} and J_{SC} on the bandgap of the photon-absorber and the band alignment of the charge selective layers.

Defects of the photon-absorber

Additionally, the film quality of the perovskite layer influences the V_{OC}. Defects within the perovskite layer can create energy states within the bandgap, which reduces the V_{OC}. However, the influence of defects on the V_{OC} is small due to the long lifetimes of trapped charge carriers.[24] Careful control of the synthesis conditions can reduce the number of surface defects and thus increase V_{OC}.[24] Furthermore, high amounts of humidity reduce the perovskite film-quality and thus the V_{OC}.[25]

2.2.3 The fill factor FF

The fill factor is the ratio of the ideal and actual power output of a solar cell.

The fill-factor determines the maximum power output of a solar cell. [21] It is defined as the ratio of the actual maximum power output, a solar cell yields, and the theoretical maximum power output of the product of V_{OC} and I_{SC} (Figure 8).

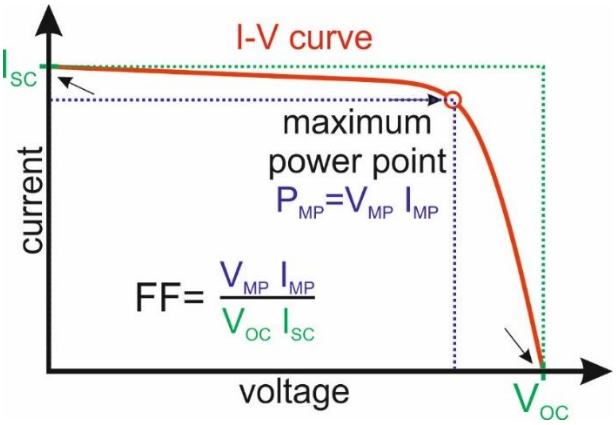

Figure 8: The short circuit current, open-circuit voltage, maximum power point and fill factor derived from an I-V-curve.

Therefore, the fill factor characterizes the “idealness” of a solar cell. Graphically, the fill factor is the ratio of the maximum power output MP (violet square, Figure 8) and the product of the maximum current density and maximum voltage (green square)

$$FF=\frac{V_{MP}\cdot I_{MP}}{V_{OC}\cdot I_{SC}}\ .$$

The “squareness” of the I-V curve increases with increasing FF. Accordingly, the area underneath the curve increases, which is the maximum power output. The fill factor is decreases with high series resistance and low shunt resistance (see below).[23]

The shunt resistance:

The shunt resistance describes the electric resistance of a solar cell against internal short circuit currents; alternative pathways for photon-generated charges, that act as power losses. Such power losses occur due to pinholes in one or several layers. Defects like pinholes minder the rectifying properties of the semiconducting layers by providing additional pathways for the recombination of charge carriers. If a pinhole is in the perovskite layer, for example, the ETL TiO_2 and the HTL Spiro are in direct physical contact. An electron from the TiO_2 layer can recombine with a hole from the spiro layer at such an interface. A low shunt resistance is reflected in a steeper negative slope in the upper part of the I-V curve (Figure 9 magenta line).

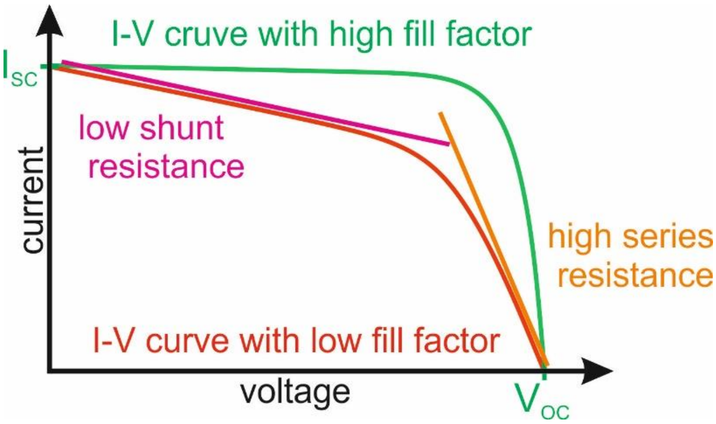

Figure 9: The influence of the shunt resistance and the series resistance on the shape of the I-V curve. An I-V-curve with a high fill factor is compared to an I-V-curve with a low fill factor. A low shunt resistance steepens the negative slope before the maximum power point (magenta line). A high series resistance steepens the negative solar after the maximum power point (orange line).

The series resistance:

The series resistance describes the internal electric resistance that charge carriers have to overcome during standard operation of a solar cell. Photon-generated electrons have to overcome the electric resistance of the perovskite layer, the ETL, the bottom electrode and any respective interfacial resistance. In the case of the charge selective layers, the electric resistance increases with layer thickness. A thick TiO_2 layer, for example, exhibits a high electric resistance which leads to increased series resistance and thus a low fill factor. Accordingly, the charge selective layers must be coated as thin as possible. However, the risk of pinholes increases with decreasing layer thickness, which causes decreased shunt resistance. Therefore, an optimal film thickness must be found for each respective layer. A high series resistance is reflected in a steep negative slope in the lower part of the I-V-curve (orange line, Figure 9).

2.2.4 Efficiency

Arguably the most important parameter of a solar cell is its efficiency in converting light into electric energy. [21] It is defined as the ratio of the power output of the solar cell compared to the energy of the incident radiation. With the maximum power output $P_{max} = V_{OC} \cdot I_{SC} \cdot FF$ follows: $\eta = \frac{V_{OC} \cdot I_{SC} \cdot FF}{P_{in}}$.

Therefore, a high open cell voltage, short circuit voltage and fill factor results in high efficiency.

2.3 The layers of a perovskite solar cell

The most common architecture of perovskite solar cells consists of five different layers: a bottom electrode, an electron transport layer, the photon-absorbing perovskite layer, a hole transport layer and the top electrode. Each layer must meet certain requirements, which will be discussed in this chapter. Additionally, the energetic level of the respective valance bands and conduction band require a good alignment for optimal charge transfer and potential output.

2.3.1 The bottom electrode: the transparent metal oxide electrode FTO

The bottom electrode, the cathode is in most cases fluorine-doped tin dioxide.

The first layer of a perovskite solar cell is the bottom electrode. It must meet several requirements since it acts both as the first functional layer of the cell and as the foundation on top of which every other layer is coated. The bottom electrode requires a sufficiently high mechanical and thermal stability in order to endure the synthesis and annealing conditions for every following layer. It needs high transparency for visible light in order to maximize the illumination of the photon-absorbing layer. And lastly, the bottom electrode requires a high conductance that allows transport of photo-generated electrons. Thin films of highly doped semiconducting metal oxides like indium/tin oxide (ITO) or fluorine-doped tin oxide (FTO) on glass substrates meet these requirements.

Properties and structure

´

$F:SnO_2$ is an n-type semiconductor that crystallizes in the rutile structure.

Within this work, I mainly used commercial FTO from Sigma-Aldrich due to several advantages compared to ITO. FTO does not need the rare element indium, which enables lower production costs of FTO substrates compared to ITOs. Moreover, FTO combines a higher chemical and thermal stability compared to ITO and can easily withstand temperatures above 500 °C while being unsolvable in any organic solvent.[26,27]
Fluorine doped tin oxide has a bandgap well above 3 eV which renders the material transparent for visible light. FTO substrates are commercially available with a transmittance of 80-82 % for visible light with a low electric resistance of approximately 7 Ω/sq.[28]

Tin dioxide crystallizes in the rutile structure, where each tin ion is surrounded by six oxygen ions with an octahedron configuration (Figure 10). Corner sharing octahedrons form a three-dimensional network. In fluorine-doped SnO_2 substrates (FTOs), a small amount of oxygen lattice ions are substituted with fluorine ions. Fluorine possesses one valence electron more compared to oxygen, which is only loosely bound to the fluorine atomic core. Such a foreign atom creates filled donor level just below the conduction band from which electrons are easily promoted into the conduction band.[29]

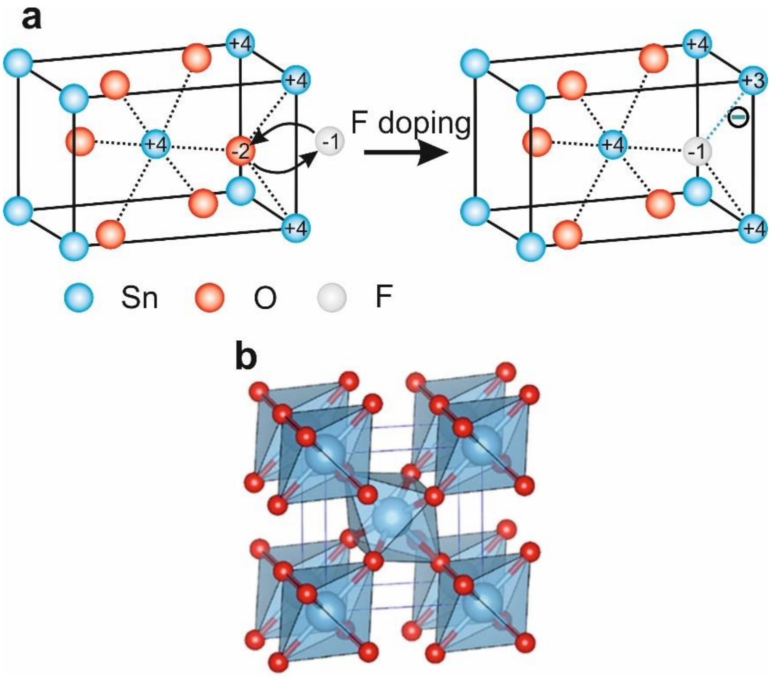

Figure 10: a) The unit cell of tin dioxide. The conductivity is increased by n-type doping: oxygen ions are partially substituted with fluorine ions. b) SnO_2 crystallizes in the rutile structure, in which corner-sharing octahedrons form a three-dimensional network.

Thus, fluorine atoms act as n-dopants in the SnO_2 host lattice by increasing the number of charge carriers. As a result, conduction increases.

Another advantage of F:SnO_2 is the energetic level of the lower conduction band edge. For an n-type semiconductor, this lower band edge is linked to the so-called Fermi-level. The Fermi-level describes the hypothetical energy level that is filled with a 50% probability at thermodynamic equilibrium. Sub-conduction band energy levels increase the Fermi-level (Figure 11). Therefore, the work function is tunable with doping.

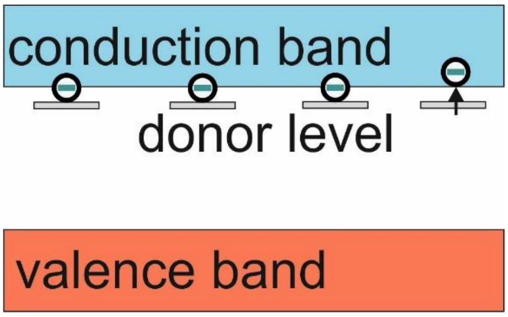

Figure 11: Schematic diagram of a semiconductor with n-type doping.

FTO preparation for perovskite solar cells

The FTO layer is removed on one edge of the substrate prior to cleaning and plasma treatment.

The FTO electrode must be patterned for usage in a perovskite solar cell to avoid electric contact with the top gold electrode contact.[2] The completed cells are contacted with gold clasps when measuring their efficiency. Since the thickness of all functional layers combined is below 1 µm, these layers are easily penetrated when applying a mechanical force to secures the gold clasps in place. Penetration of the upper electrode and every following layer down to the substrate would lead to a short circuit if the FTO is not removed beforehand. Therefore, one side must be etched free of the FTO, which later carries the gold contact in the completed solar cell.

For etching the FTO substrate, the whole substrate is tightly covered with Capton-tape® except for 5 mm of one edge (Figure 12). The area without tape is then evenly covered with a small pile of zinc powder. Hydrochloric acid with a concentration of 3 mol/L is dispersed onto the edge. A pipette is used for dispersing the acid/powder slurry to guarantee full coverage of the substrate. The substrate is rinsed carefully with plenty of water after 1 min of reaction time. The Capton tape is subsequently removed and the substrates are marked with numbers by scratching on the glass side with a diamond pen.

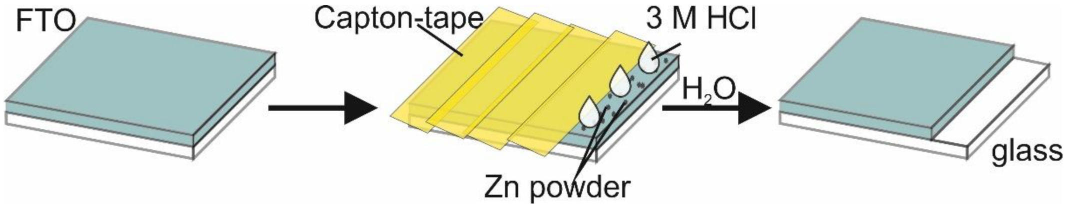

Figure 12: Patterning of the FTO substrate.

Cleaning of the substrate

Proper cleaning of the substrate is vital for efficient solar cells (Chapter 3). The substrates were cleaned manually by scrubbing each side with water and Hellmanex® for 15-20 s each. Any residue of detergent was removed by flushing the substrates excessively with hot tap water (T=51 °C), followed by highly purified water (Milli-Q). At this point, the FTO covered glass slide must not show any smears, salt residues or other visible contamination. Each substrate was subjected to argon- or-oxygen-plasma treatment for 30 min directly prior to the cell synthesis with a power output of 300 W at a gas pressure of 0.15 mbar. (Plasmaprozessor 200-G TePla Technics Plasma GmbH; Chapter 4).

---

[2] 2 It has to be noted, that parts of this chapter, especially the preparation of the individual layers, is based on my publication from 2019.[52]

2.3.2 The electron transport layer Titan dioxide

The electron transport layer has to meet ambivalent requirements. It needs to be highly conducive for electrons while being insulating for any photon-generated holes. Similar to the bottom electrode, the ETL requires enough chemical and thermal stability to endure the synthesis conditions of every following layer. Since the path of the incident light passes through the ETL before reaching the photon-absorbing layer, the ETL must exhibit high transparency. Both the transparency and charge selective properties require a large bandgap with a conduction band that is aligned with the conduction band of the photon-absorber (Figure 13).

Properties and structure

The n-type semiconductor TiO_2 anatase is used as the electron transport layer.

In general, TiO_2 meets the requirements for an ETL in PSC. The energy level of its lower conduction band edge at -4.0 eV is aligned with the conduction band of $MAPbI_3$ 3.9 eV. [30,31] An upper valance band edge of TiO_2 at -7.2 eV creates a bandgap of 3.2 eV that prevents the absorption of visible light. [30,31] Since the upper valence band edge of the perovskite at -5.44 eV lies within approximately the center of the bandgap of TiO_2, this metal oxide efficiently blocks photon-generated holes of the perovskite layer (Figure 13). [32]

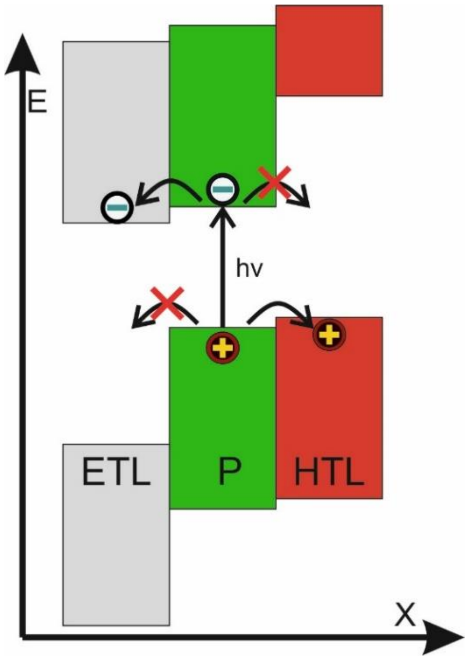

Figure 13: Band diagram of the perovskite layer (green), the electron transport layer (gray) and the hole transport layer (red).

Thus, electrons in the conduction band of $MAPbI_3$ are extracted into TiO_2, whereas holes are efficiently blocked.[33] TiO_2 is widely used because it is chemically more stable than organic ETLs or other metal oxide semiconductors like ZnO.[34] Once formed, TiO_2 only dissolves in strong acids and withstands temperatures of over 500 °C. [35,36] Furthermore, TiO_2 readily forms smooth and pinhole-free films that enable efficient electron extraction with a *PCE* over 23% for mixed cation based perovskite solar cells.[37] Depending on the temperature, pressure and chemical environment, TiO_2 mainly crystalizes in three major modifications: anatase, rutile and brookite.[38] Among those modifications, anatase exhibits the highest electron mobility, highest electron affinity and the biggest band gap.[39,40]

Moreover, anatase forms at temperatures below 500 °C, whereas rutile is formed at temperatures above 600 °C.[41] A lower annealing temperature reduces the energy needed as well as the thermal stress on the FTO substrate. These properties make anatase the favorable TiO_2 modification for ETL in perovskite solar cells. Within the anatase crystal, a titanium ion is surrounded by six oxygen ions in an octahedral formation. Each octahedron shares an edge with four neighboring octahedrons (Figure 14 b).

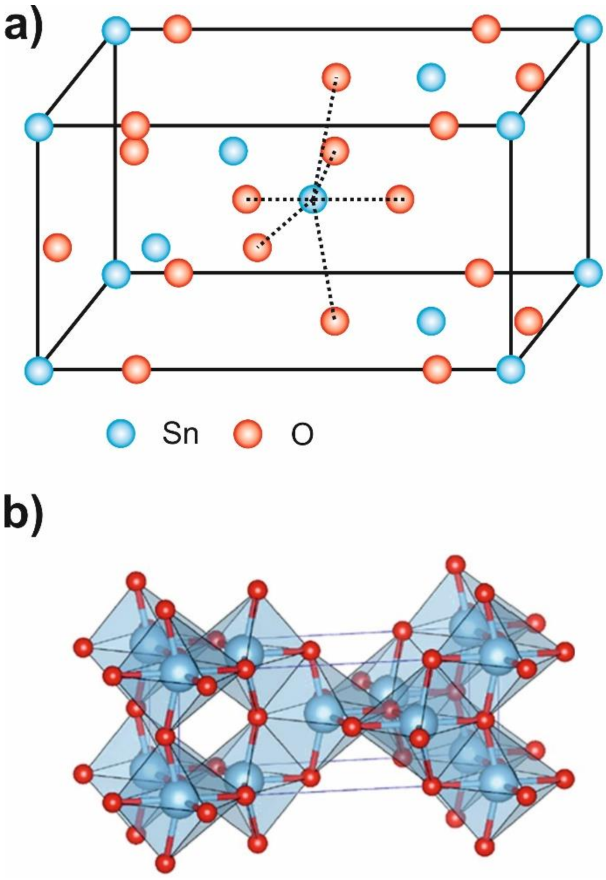

Figure 14: a) The anatase unit cell and b) the anatase structure.[42]

Preparation of TiO_2 thin films

TiO_2 thin films are spin-coated with aqueous $TiCl_4$ solution.

The application of TiO_2 for thin-film technologies requires a reproducible method that is easy, cheap, reproducible and versatile. In literature, TiO_2 thin films have been synthesized using various methods from spray coating, chemical bath deposition, sputtering and spin-coating.[43–46]

Within this work, I solely used spin-coating for synthesis because I found spin-coating easier and more reliable than comparable methods. Commonly used spray coating based techniques are influenced by the nozzle geometry, the spraying angle, the substrate’s temperature, the composition of the carrier gas and thus require more practice and setup control than simple spin-coating.[47–50]
Spin-coating needs only a fraction of the solution compared to a chemical bath.[51] Although 90% of the initial volume is lost during spin-coating, only 80 µL of the solution is needed for a substrate with a size of 2.5 x 2.5 cm². For dip-coating substrates with the same size, a dipping volume of at least 10 ml is needed. Finally, a spin-coater is cheaper to purchase and maintain with a lower energy consumption compared to thermal evaporation based approaches.[45]

Solution preparation

$TiCl_4$ is added slowly to frozen deionized H_2O in a dry ice/acetone bath.

I mainly used an aqueous $TiCl_4$ solution as a precursor for TiO_2 thin film synthesis.[52] It is a well-established system that can be easily spin-coated and form fast and reproducible pinhole-free TiO_2 thin films.[46]

Since $TiCl_4$ reacts strongly with water, it must be added very carefully. I prepared a 2 M stock solution by cooling down 10 ml of highly purified water in a dry ice/acetone bath until it was frozen. Over approximately two minutes, 2.19 ml of $TiCl_4$ (Sigma-Aldrich, 99,9% trace metal basis) was slowly added to the ice with a syringe. The vial must be kept in liquid nitrogen, freezing the $TiCl_4$ almost instantly. Note, I did not use a cannula on the syringe when adding the $TiCl_4$ to the water because the cannula plugs easily.

The mixture was allowed to melt very slowly by removing the vial from the ice bath and submerging it back again repeatedly. Simultaneously, I carefully shook the vial. During this procedure, any potential built up of pressure in the vial must be released carefully. The yellowish frozen $TiCl_4$ dissolves slowly at the water interface until a clear, colorless, precipitation-free solution is formed. Finally, the solution was filtered with a PTFE syringe filter and stored at -15 °C. The solution stays liquid at these temperatures. For a 1 M, 0.75; and 0.5 M solution, the 2 M stock solution was diluted with the respective amount of highly purified water without any further cooling. The diluted solutions were also stored at -15 °C. At these temperatures, these solutions became solid.

Spin-coating procedure

Spin coated $TiCl_4$ solution is annealed at 500 °C in air.

All TiO_2 thin films were synthesized in ambient conditions on freshly cleaned and plasma cleaned substrates. For solar cell synthesis and cSFM measurements, one small area opposite to the edged FTO area was kept uncoated. For that, a piece of Scotch Tape® was placed on one edge of the substrate (Figure 15). The substrates were transferred to the spin-coater directly after plasma-cleaning treatment and application of the scotch tape. 80 µL of the aqueous $TiCl_4$ solution was dispersed on the substrates.

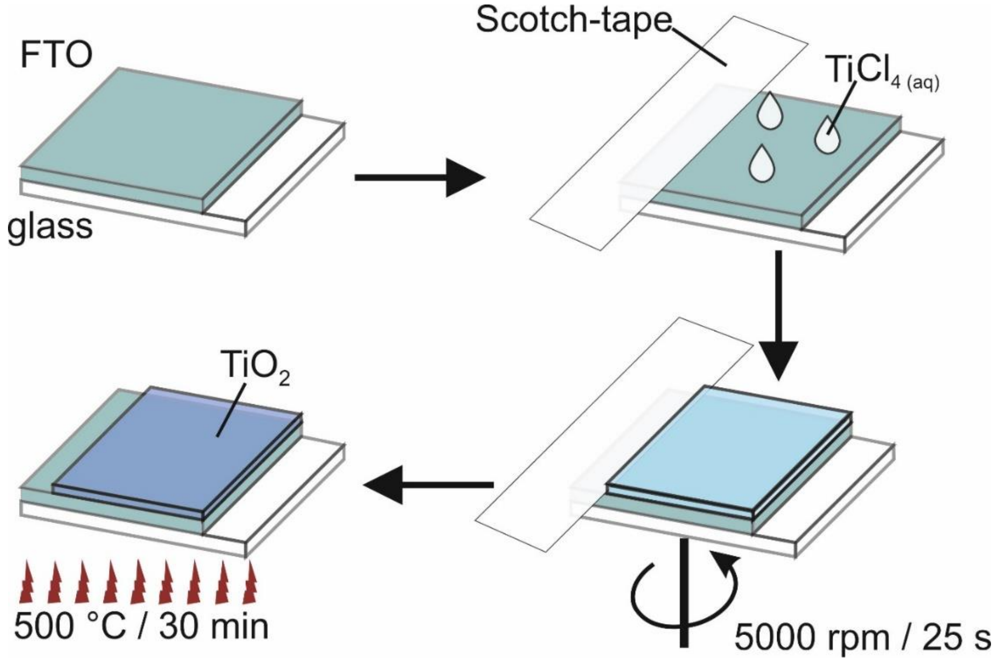

Figure 15: Synthesis of a TiO_2 thin film on an FTO substrate.

The substrates were rotated immediately at 5000 RPM for 30 s. The Scotch-Tape® was removed resulting in a TiO_2 free area.

The freshly formed films were dried at 150 °C at a hotplate in air and annealed at 500 °C at a high-temperature hotplate in air for 30 min according to the following temperature program:

- **125 °C for 1 min with a ramping time of 5 min**
- **225 °C for 1 min with a ramping time of 5 min**
- **325 °C for 1 min with a ramping time of 5 min**
- **425 °C for 1 min with a ramping time of 5 min**
- **500 °C for 30 min with a ramping time of 5 min**
- **Cooling down naturally to RT**

After the substrates cooled down to 150 °C naturally, they were subjected to an additional 30 min of UV-ozone treatment (see Chapter 4).

Minimizing the TiO_2-c layer

The electron transporting TiO_2 layer must be as thin as possible for reducing the bulk electric resistance while exhibiting no pinholes for efficient hole blocking properties.

The electron transport layer requires a high conductance for electrons while efficiently blocking photon-generated holes. Therefore, the TiO_2 films should have a high bulk electrical conductance, which enables fast and efficient charge collection rates from the perovskite photo-absorbing layer.[53,54] Film thickness is a key attribute that determines a multitude of properties of a thin film like the electric resistance and optical transmittance. Since the electric conductance decreases with increasing film thickness, the TiO_2 layer must be as thin as possible to minimalize the electric resistance for electrons. However, the thin film must exceed a certain thickness in order to prevent the formation of pinholes. Otherwise, photon-generated holes of the perovskite film can migrate through the pinholes of the TiO_2 layer to the FTO electrodes and create short circuits. For high efficient solar cells, the thickness of the compact TiO_2 is usually under 35 nm.[37] Most groups focused on spray-coating for synthesizing the TiO_2 thin film. In this part, I demonstrate that spin-coating is also suited to producing sufficient thin films.

M. Chakraborty described an empirical expression for the film thickness of spin-coated polystyrene thin films.[55]

$$d = \frac{K\eta^{\gamma}C^{\beta}}{\omega^{\alpha}}$$

The film thickness *d* depends on four basic parameters: the evaporation rate of the solvent, which is represented by a calibration constant *K*; the concentration of the precursor solution *C*, the intrinsic viscosity of the solution η; and the rotational speed (number of rotations per minute) ω. The exponent factors α, β, and γ are influenced by the solvent, the temperature, the spin-coated substance, the surface and have to be determined experimentally. The intrinsic viscosity and the evaporation rate also mainly depend on the solvent. Therefore, three main parameters can be varied in order to influence the film thickness: the solvent, the angular velocity, and the concentration. Water is a preferred solvent since it is cheap, non-toxic and easily purified. The angular velocity cannot be arbitrarily increased since the vacuum of the spin-coater fails to secure the substrate in place above a certain threshold of angular velocity. Thus, the most feasible approach to reduce the film thickness is by reducing the concentration of the precursor solution.

A sacrificial 5 nm gold layer between a glass substrate and a TiO_2 thin film allows measuring the TiO_2 film thickness easily.

In order to identify the optimal precursor concentration, I prepared samples from a 2 M, a 1 M, a 0.75 M and a 0.5 M concentration and compared the resulting layer thickness (Figure 16).

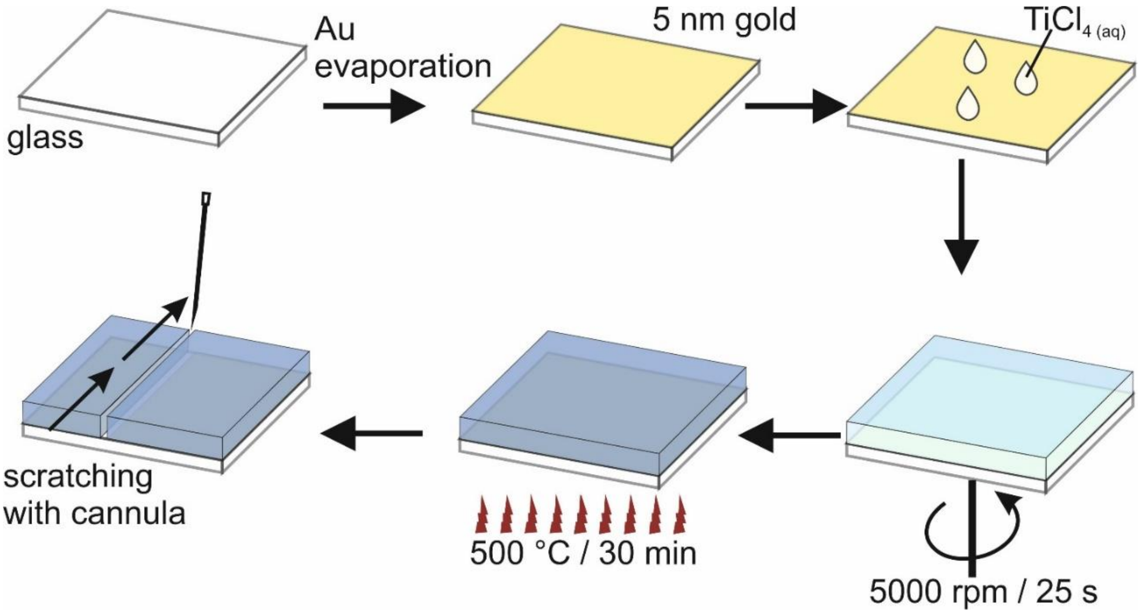

Figure 16: Measurement of the layer thickness of a TiO_2 thin film on a glass substrate. A thin intermediate gold layer reduced adhesion between glass and TiO_2 and enable partial removal of the TiO2 with a cannula.

In order to measure the TiO_2 layer thickness, a glass slide was coated with a 5 nm thick layer of sacrificial gold that has low adhesion to the glass surface. The gold surface was covered with the respective precursor and treated as described above. After annealing at 500 °C, the Au/TiO_2 film was scratched away with a metal cannula. Each film was measured with a profilometer (KLA-Tencor Stylus Profiler Modell P7) at three different spots of each sample (Figure 17).

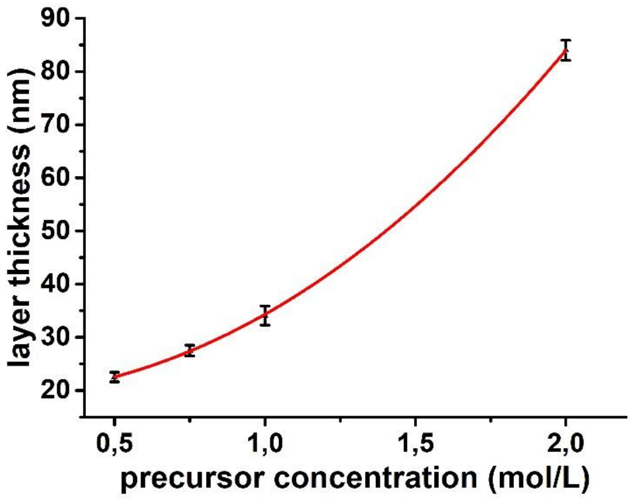

Figure 17: The dependence of the layer thickness on the precursor concentration of TiO2 thins films. The red line represents a customized fit using OriginPro 9.1.

A 2 M precursor solution resulted in a film thickness of 84.0 ± 1.9 nm. For a 1 M solution, a layer thickness of 34.1 ± 1.8 nm was measured. A thickness of 27.5 ± 1.1 nm was synthesized with a precursor concentration of 0.75 M. A TiO_2 thin film made from a 0.5 M solution had an average thickness of 22.5 ± 0.9 nm. However, the three measured profiles for the 0.5 M solution showed huge variations with a layer thickness below 5 nm. Thus, the film was not hole-free but patchy and therefore not suited for perovskite solar cells.

In order to estimate the experimental dependence of the layer thickness on the concentration, the data were fitted using origin and a customized function $d = a + b \cdot C^{\beta}$

Here, *d* represents the layer thickness, *C* the concentration and β the experimental exponent factor. The parameters *a* and *b* depend on the angular velocity, the viscosity, their experimental exponent factors and a generic calibration constant. For an aqueous $TiCl_4$ solution with different concentrations at ambient conditions in my setup, an experimental dependence of the layer thickness was found with $d = (19.1 \pm 0.4) + (15.1 \pm 0.5) \cdot C^{(2{,}10 \pm 0{,}04)}$.

A concentration of 0.75 M $TiCl_4$ in H_2O yielded the minimum film thickness without pinholes.

It would be expected, that parameter a was equal zero since with the concentration c = 0 the resulting thickness d must also be 0. However, for a non-ideal film formation, no infinite thin films can be formed. When the concentration falls below a certain threshold, no pinhole, compact film is formed but isolated patches of TiO_2. Interestingly, a = (19.1 ± 0.4) is very close to the average film thickness of 22.5±0.9 nm which was achieved with a concentration of 0.5 M $TiCl_4$. I hypothesize, that the parameter a can be understood as the theoretical minimum for a compact thin film formation under the given conditions (e.g. the intrinsic viscosity *η,* and the number of rotations per minute *ω* and the calibration constant *K*, that depends on the ambient temperature, humidity, and evaporation rate due to airflow within the spin-coater). However, this theoretical minimum is practically not achievable due to local dewetting, creeping effects and due to the rough FTO surface.

In conclusion, a further decrease of the concentration would not lead to a thinner, compact film, but to more pinholes or patches. One way of further decreasing the thickness of a compact film would be in varying the other parameters. The number of rotation can only be increased to 6000 rpm, before the substrate is flung off the spin-coater chuck. The vacuum, that holds the substrate in place, is too weak to enable a higher rotation velocity. Therefore, decreasing the viscosity, or increasing the evaporation rate of the solvent via increasing the airflow through the spin-coater may be a route for further reducing the film thickness.

Synthesis of a TiO_2 mesoporous layer

A commercial TiO2 rutile nanoparticle paste was diluted with ethanol and spin-coated.

Many groups coat an additional mesoporous layer on top of the compact TiO_2 electron transport layer. For that, a diluted paste containing TiO_2 rutile nanoparticle is spin-coated onto the compact TiO_2 electron transport layer and then sintered at 500 °C for 30 min (Figure 18).[56]

This additional layer affects the solar cell performance is several ways. Cells with a mesoporous geometry have an increased efficiency compared to a planar architecture and exhibit a lower hysteresis of measured efficiency of forward and backward scans.[57] The mesoporous layer enlarges the interface area between the ETL and the perovskite layer and thus facilitate charge transport of electrons from the perovskite into the ETL.[58] David O. Scanlon et al reported a lower work function of anatase compared to rutile by 0.2 eV. This difference facilitates charge transport from the rutile particle into the anatase and thus facilitates the charge separation, which prevents recombination.[39]

Within my work, I constructed both planar and mesoporous cells.

Precursor preparation

For spin-coating a mesoporous TiO_2 layer, I prepared a precursor dispersion by diluting 0.2 g of commercially 30NRD paste (Dyesol®) with 1.2 g of p.A. ethanol.[59] This paste consists of 30 nm-sized TiO_2 nanoparticles and surfactants. The precursor was excessively shaken until the paste was completely dispersed. Then, the dispersion was treated in an ultrasonic bath for 30 min. The TiO_2-c covered substrates were transferred to the UV-ozone cleaner directly after they cooled down to 150 °C. The TiO_2 thin film was subjected to 30 min of UV-ozone treatment and immediately transferred to the spin-coater.

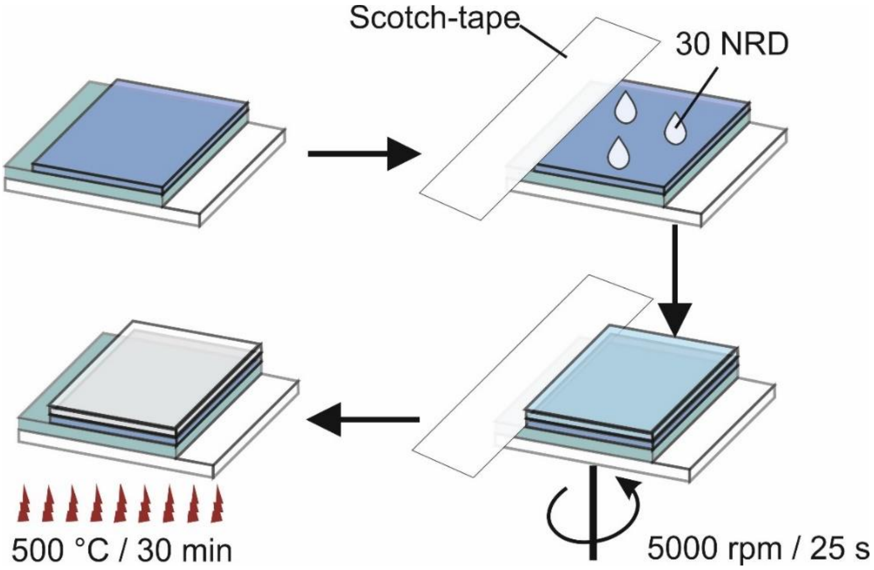

Figure 18: Synthesis of a TiO2 mesoporous film on a TiO_2 thin film on an FTO substrate.

Spin-coating

The edge that was not covered with compact TiO_2 was again covered with Scotch-Tape® prior to the spin-coating. The diluted 30NRD paste was dispersed onto the substrates which then were spin-coated immediately at 5000 rpm for 30 s. The mesoporous layer was annealed with the same program as the compact TiO_2 thin films.

2.3.3 The photon-absorbing perovskite layer

$CH_3NH_3PbI_3$ crystallizes in the perovskite structure, is processable from solution and possesses optimal parameters for the absorption of visible light.

The perovskite layer acts as the photon-absorbing layer within a solar cell. Several requirements must be met by the photon-absorber. As Shockley and Queisser calculated, a bandgap between 1.1-1.5 eV enables the highest theoretical power conversion efficiency.[22] High charge carrier diffusion length enables low recombination and efficient charge extraction.[60,61] The absorber must be easy to process and synthesize while only consisting of earth-abundant materials for low production costs. A high extinction coefficient reduces the required film thickness.

Mixed organic/inorganic halide Perovskite films meet these requirements. $CH_3NH_3PbI_3$ ($MAPbI_3$) was first utilized as a photon-absorber for solar cells by A. Kojima et al. in 2009 and remains the gold standard for perovskite solar cells.[18] This material has a bandgap close to the optimum with 1.52 eV The upper valance band edge of -5.44 eV aligns with the upper valance band of a variety of organic p-type semiconductors. [62,63] The lower conduction band edge of -3.93 eV aligns with several n-type semiconductors as TiO_2, SnO_2 and ZnO.[30,62]. $MAPbI_3$ exhibits strong absorption in the visible spectrum with a reported penetration depth for 550 nm light of approximately 660 nm.[64] A diffusion length for electrons and holes above 175 µm was reported for single crystals[65] and over 1 µm for polycrystalline films.[60]. $MAPbI_3$ is processable from solution, which enables synthesis with standard printing techniques like spin-coating, spray-coating, dip-coating, and blade coating.[66–69].

The perovskite structure consists of three different ions: two cations A and B and one anion X with the general chemical formula of ABX_3. In mixed organic/inorganic perovskite, Pb^{2+} acts as the B cation and is surrounded by an octahedron of I- ions, which represent the X anion. The octahedrons form a corner-sharing three-dimensional network. The cuboctahedron void is occupied by the methylammonium A-cation. (Figure 19)

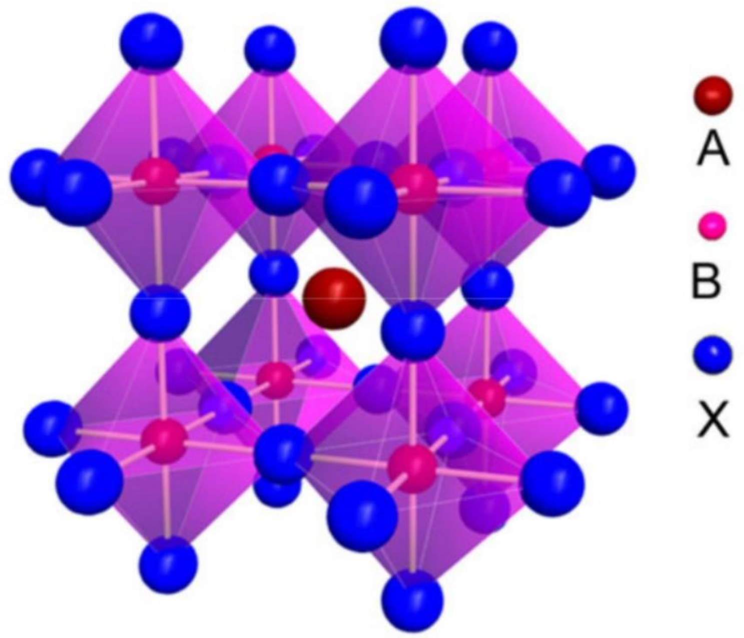

Figure 19: The perovskite structure. [70]

Both the cations and the anions can be partially or fully substituted with a variety of different ions according to the empirical Goldschmidt-rules:[71,72]

- One ion can be replaced with another when the radii do not differ more than 15 %
- The ion with the smaller ion radius is preferentially incorporated of two different ions with the same charge.
- The ion with the higher charge is preferentially incorporated of two different ions with similar radii but different charges.

In recent studies, the A cation methylammonium was substituted with formamidinium, rubidium, Caesium. [73–75] Substitution of the B cation Pb^{2+} with a less toxic candidate is desireable but proofed to be difficult.[76–80] The most promising candidate is Sn^{2+} which is inferior in stability and efficiency.[80] The X cation I- was substituted with chloride or bromide.

Full substitution, however, leads to a drastic change of bandgap from 1.53 eV for $MAPbI_3$ to 2.24 eV and 2.97 eV for $MAPbBr_3$ and $MAPbCl_3$.[81] Partial substitution, however, enables a tunable bandgap suited for applications as tandem solar cells with two different photon-absorbers.[82]

Since the aim of my work was to further the understanding of charge transport through the layers, I focused exclusively on the “gold-standard” $MAPbI_3$.

Synthesis of a $CH_3NH_3PbI_3$ layer

The film quality of the perovskite layer is mainly determined by two parameters: a sufficient high thickness and the absence of pinholes. High efficient cells have a film thickness of approximately 500 nm, which enables high absorption of visible light and thus increase the number of photo-generated charge carriers.[83] Pinholes cause direct electric contact between the opposite charge-selective layers, which create short circuit pathways. Therefore, the perovskite layer must be pinhole free.

Perovskite thin-film synthesis was conducted with spin-coating based approaches. As explained above Minimizing the TiO_2-c layer, the film thickness depends on the rotational speed *ω,* the intrinsic viscosity of the solution *η,* the concentration of the solution c and the evaporation rate of the solvent, which is represented in the calibration constant K (*Minimizing the TiO2-c layer*). [55]

A long crystallization period favors the formation of isolated single grains instead of a homogeneous film.

However, the resulting film thickness and quality are far more dependent on the ambient conditions during spin-coating for the perovskite synthesis than compared to thin-film synthesis of TiO_2. A multitude of different approaches have been published for synthesizing perovskite thin films, ranging from simple one-step synthesis, solvent annealing, solvent engineering, and vacuum flash approaches, to two-step synthesis as two-step spin-coating, chemical bath deposition or thermal evaporation.[84–90] The variety of different published approaches is an indicator in itself that the reproduction of certain recipes in different laboratories can be challenging. Moreover, a unifying theoretical understanding of all the parameters that influence the initial film formation is still required.

Since such a unifying understanding of the crystallization dynamics of perovskite thin films is beyond the scope of this work, the respective issues are not discussed here in detail. However, when comparing different approaches, I identified one major issue that prevents the formation of a high-quality perovskite film: a slow evaporation rate of the solvent during spin-coating. A slow evaporation rate is, in particular, a problem for perovskite synthesis, since one of the main precursors, PbI_2, has a very low solvability in most solvents. Only a few solvents enable concentrations above 0.5 mol/L that enable sufficient high film thickness for solar cells. The most frequently used solvents are dimethylformamide (DMF), dimethylsulfoxide (DMSO) and gamma-butyrolactone (GBL). DMF has a boiling point of 153 °C, DMSO boils at 189 °C, and GBL at 204 °C. Such a high boiling point coincides with low vapor pressure and thus a slow evaporation rate.

If the evaporation rate of the solvent is slow during spin-coating, the supersaturation of the solvent film occurs slowly. Thus, random occurring nucleation sites are surrounded by the precursor solution that enables sufficient high ion mobility for Ostwald ripening. As a result, few isolated grains with several micrometer diameters are formed instead of a homogeneous film.[91] In contrast, a fast evaporation rate results in a fast supersaturation, which leads to even distribution of nucleation sites. As a result, a homogeneous, pin-hole free film is formed (Figure 20).

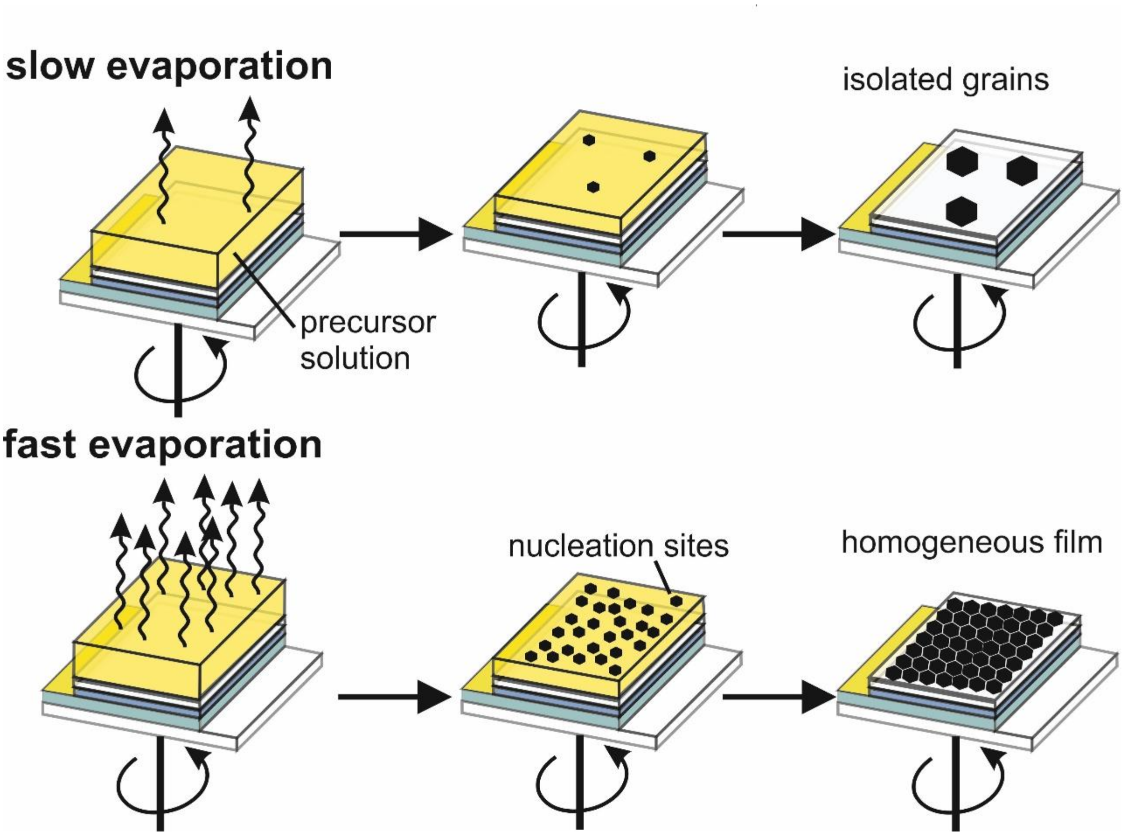

Figure 20: The influence of the evaporation rate on film quality. Slow evaporation leads to a slow supersaturation and therefore a prolonged nucleation time frame. As a result, isolated grains are formed due to Ostwald ripening. Rapid evaporation of the solvent leads to a fast supersaturation and thus to an even distribution of nucleation sites. A homogenous film percent.

Several approaches have been conducted in order to prevent the formation of isolated grains either by increasing the evaporation rate or by delaying the formation of nucleation sites (Figure 21).

High angular velocity and a solvent engineering process enable a homogeneous film formation.

R. Kang et al reported, that a higher rotational speed leads to higher evaporation and thus to better film quality.[92] N. J. Jeon et al. were the first to apply a solvent engineering approach for spin-coating perovskite films.[66] For that approach, a so-called antisolvent is dripped onto the spinning, precursor-coated substrate (Figure 23). This antisolvent does not solve the perovskite precursors but is miscible with DMF and DMSO. As a result, the solvents are washed out, while precipitating the precursors and thus accelerating the supersaturation of the solution, which leads to the formation of a homogeneous film. Another common approach targets the choice of solvents for the precursor solution. DMF has the lowest boiling point of the three mainly used solvents and thus has the fastest evaporation rate.

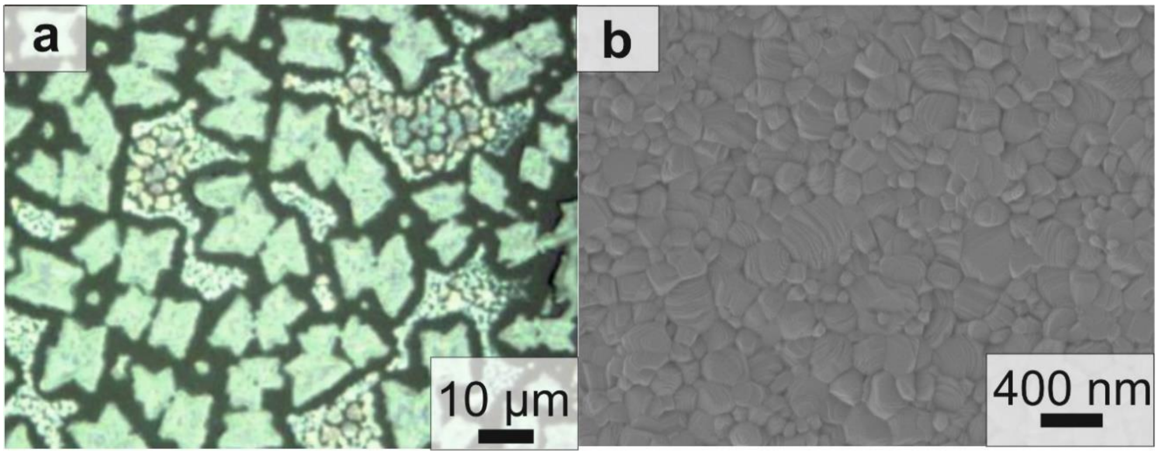

Figure 21: The grain size depending on the evaporation rate of the solvent during spin-coating. a Representative laser-microscope image of isolated $MAPbI_3$ grains on FTO. I spin-coated from a 0,66 M $MAPbI_3$ solution in DMF at 2000 rpm without any extra treatment.[91] A slow evaporation rate lead to the formation of isolated single grains.
b Representative SEM image of a homogeneous $MAPbI_3$ film spin-coated from a 1 M DMF solution at 5000 rpm with a solvent engineering approach and toluene as an antisolvent. A faster evaporation rate and forced precipitation due to the antisolvent causes a smooth film formation

Accordingly, the publications with the highest reported efficiency use DMF as the main solvent.[93,94] However, DMSO is reported to form a Lewis-base adduct with PbI_2. [95] This adduct easily forms a pinhole-free intermediate film, that keeps isolated Pb-I octahedron in a quasi-liquid state and thus inhibits the formation of nucleation sides. This intermediate film enables a stable end even distribution of precursor with low mobility until further evaporation of the DMSO at elevated temperatures leads to a formation of a perovskite thin film. [95] Although perovskite films are normally annealed at 100 °C, a preceding drying step at 50 °C enforces the formation of an intermediate film and thus prevents the nucleation of isolated single grains. [96] The temperature of the glovebox also influences the evaporation rate. It has been reported, that film quality increases, if the temperature within the box is above 24 °C. [82,97] The evaporation rate of the precursor film also depends on the solvent vapor within the spin-coater / glove box atmosphere. I increased the gas exchange of the glovebox by increasing the nitrogen feed pressure from 0.5 bar to 2 bar and thus established a sufficient high constant nitrogen influx into my glovebox. Therefore, by reducing the accumulation of solvent vapor, I increased the reproducibility of high-quality films. Moreover, removal of the spin-coater lid leads to an increased gas circulation within the spin-coater and proofed to be crucial for improving the reproducibility of film quality due to improved gas exchange between spin-coater volume and glove box volume (Figure 22). Lastly, I noticed that the temperature of the nitrogen influx was higher in summer than compared to winter. In August, I measured a gas temperature of 25 °C whereas in January, the gas temperature was around 18 °C. This increased gas temperature coincided with a higher achieved solar cell efficiency.

Figure 22: The indicated area is normally covered with a lid. Removal of that lid leads to improved gas exchange between spin-coater and glovebox.

Therefore, my approach (as displayed above) represents a careful adaptation and combination of a multitude of reported recipes that enabled me to prepare state-of-the-art $MAPbI_3$ solar cells with an efficiency of 19,5 %.[52,66,82,92–99] [3]

Substrate preparation

Perovskite thin films were coated on freshly synthesized TiO_2 films. After the mesoporous TiO_2 films were cooled down to 150 °C after annealing at 500 °C, they were subjected to 30 min of UV-ozone treatment. The substrates were transferred into the flow-box immediately after the treatment and dried at 100 °C for 30 min in order to remove any adsorbed water.

---

[3] This recipe was also reported in 2019.[52]

Flowbox and spin-coater preparation

Two hotplates were located in the glovebox and switched on two hours in advance to the film synthesis. The smaller one was set to 50 °C, the bigger one to 100 °C. Before film synthesis, the ambient temperature within the flow box should be at least 25 °C.[82,97] In order to achieve constant atmospheric conditions within the box, i.e. no accumulation of solvent vapor in the atmosphere, I established a constant nitrogen influx. The feed valve was set to 2 bar. The spin-coater lid was removed prior to any film synthesis.

Precursor preparation

For the perovskite precursor solution, 553 mg PbI_2 (Sigma-Aldrich, beads, -10mesh 99.999 % trace metal basis) and 188 mg MAI (Dyesol) were dissolved in 0.8 ml DMF (Sigma-Aldrich, 99 %) and 0.2 ml DMSO (Sigma-Aldrich 99.5 %) resulting in a 1.2 M solution.[95] The choice of the lead precursor is critical for film quality. The purity grade "metal basis" only refers to the amount of metal contaminations. Several non-metal or metalloids like H, B, C, B, O, F, Si, P, S, Cl, As, Se, Br, Te, and At may not be considered. Thus, PbI_2 might be contaminated with $PbCO_3$, PbS, and $PbSO_4$. When using "standard" 99.99 % metal basis purity PbI_2 (Fisher, Alfa Aeser, Sigma Aldrich), even low concentrations like 0.5 M $MAPbI_3$ in DMF did not form clear solutions. Though syringe filters may render a clear solution they are not sufficient in achieving a high film quality. Commercially available filters have a minimum pore size of 0.2 µm. Thus, particles with a size of up to 200 nm can pass the filter and be incorporated into the formed perovskite film. The average film thickness of a 1.2 M $MAPbI_3$ is around 300-500 nm. Therefore, foreign particles with a size of up to 200 nm significantly influence the thin film quality. In this work, I used commercially resublimated PbI_2 Sigma-Aldrich, beads, -10 mesh 99.999 % trace metal basis).

Spin-coating

After the substrates were dried in the flow box at 100 °C, they were cooled down to RT. Subsequently, they were covered with 80µL of the precursor solution and spun at 500 rpm for 10 s and at 4000 rpm for 25 s.[52,99] After the substrates were spun for 10 s at 4000 rpm a volume of 150 µL of toluene are dropped at the still rotating substrates.[66] The Eppendorf tip should be vertical with a distance to the surface of under 1 cm. The solvent must be added dropwise over approximately 3 s at the center of the spinning substrate. This step must be conducted in a careful manner since it determines the resulting perovskite film quality. The resulting perovskite precursor film should be clear with no visible roughness at this point. The substrates were immediately placed onto a hotplate at 50 °C.[96]

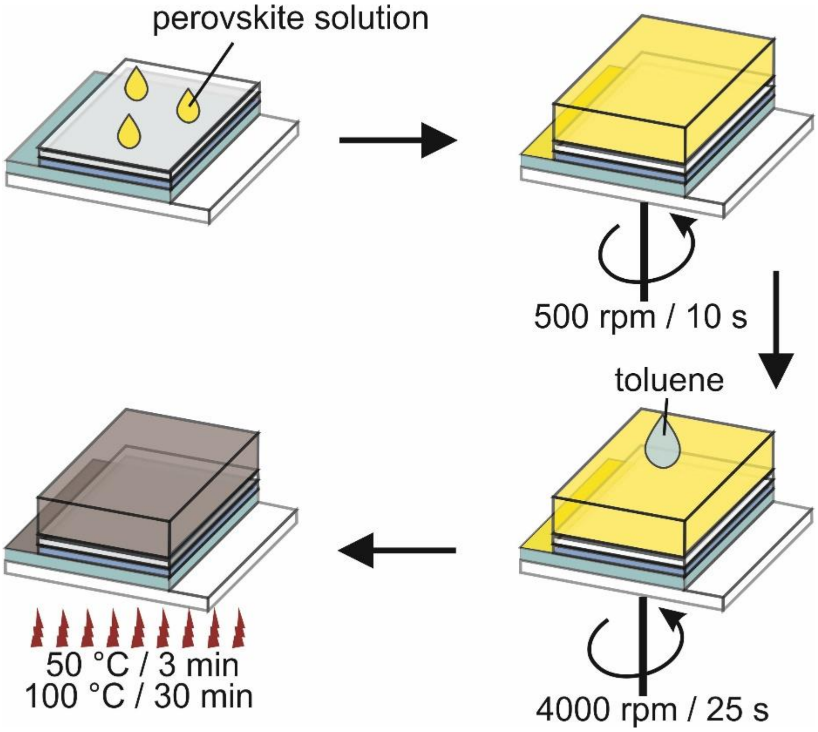

Figure 23: Synthesis of a perovskite film on a TiO_2 mesoporous film.

After 3 min, the light yellow film changed to an orange color. The substrates were annealed at 100 °C for 30 min resulting in an almost black, highly reflecting perovskite layer with a film thickness of approximately 500 nm.[98]

2.3.4 The hole transport layer Spiro-OMeTAD dioxide

"Spiro-OMeTAD" is a p-type organic semiconductor that possesses a good alignment of its HOMO and LUMO level with the bands of the perovskite photon absorber.

The second charge selective layer is the so-called hole-transport layer. The HTL must efficiently block electrons while transporting photon-generated holes from the perovskite layer to the anode.[100] For that, the material needs p-type semiconducting properties with a valance band edge that aligns with the valence band of the perovskite layer. Additionally, the bandgap of the HTL must be larger than the bandgap of the perovskite. In that case, the lower states of the conduction band of the perovskite are energetically within the bandgap of the HTL. Accordingly, no energy levels of the HTL align with the conduction band of the perovskite, which inhibits the transport of photon-excited electrons through the HTL (Figure 13). Since the HTL is coated on top of the perovskite layer, it needs to be solvable in orthogonal solvents that do not etch or solve the perovskite layer. Here, the non-polar solvent toluene was applied.

The commercially available organic compound N2,N2,N2′,N2′,N7,N7,N7′,N7′-octakis(4-methoxyphenyl)-9,9′-spirobi[9H-fluorene]-2,2′,7,7′-tetramine (spiro-OMeTAD) meet these requirements (Figure 24). This compound is solvable in nonpolar solvents as chlorobenzene or toluene that do not solve the perovskite.

Spiro-OMeTAD is an organic semiconductor with a HOMO-level at -5.22 eV and a LUMO-level at approximately -2.3 eV [101] [30] Adding Li-TFSI to Spiro-OMeTAD acts as p-type doping, which facilities the partial oxidation of the hole transport material by oxygen of the atmosphere.[102] This oxidation leads to an increase of the conductivity by 100-fold.[102]
S. N. Habisreutinger et al. further demonstrated, that the addition of 4-tert butyl pyridine further improves the HTL / perovskite interface and increases solar cell efficiency.[102]

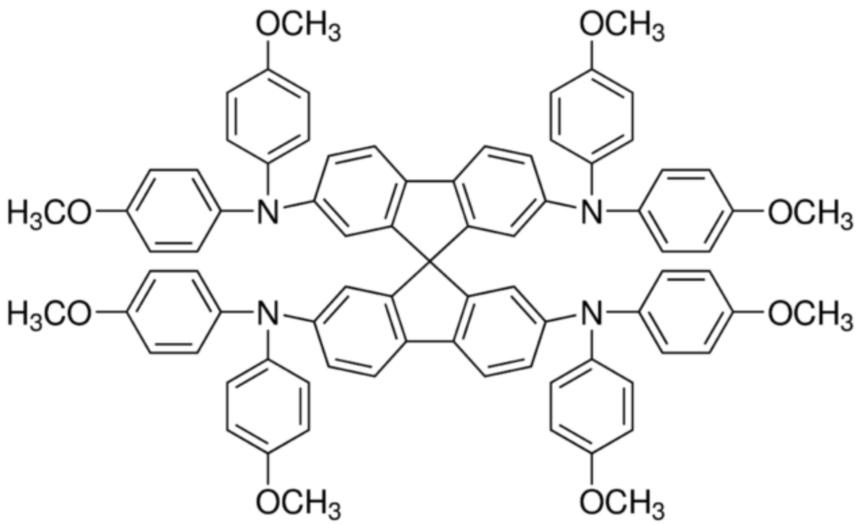

Figure 24: Chemical structure of N2,N2,N2′,N2′,N7,N7,N7′,N7′-octakis(4-methoxyphenyl)-9,9′-spirobi[9H-fluorene]-2,2′,7,7′-tetramine - Spiro-OMeTAD

On the downside, Spiro-OMeTAD crystallizes at higher temperatures which leads to deteriorating film quality and cell efficiency.[103] Moreover, the dopant Li-TFSI is hygroscopic, which leads to an increased tendency to attract water from ambient conditions and accelerate the degradation of solar cells.[104] Z. Li et al. found evidence, that Li^+ ions also migrate through the Spiro layer into the perovskite layer and negatively impact PSC performance.[105] Therefore, further research is required for increasing the cell stability. However, addressing these stability issues is beyond the scope of this work. Spiro-OMeTAD is widely used and exhibits the highest reported efficiency. It is commercially available and well-studied. J.-W. Lee et al. provided a very recent review of strategies to increase the stability of perovskite solar cells. Addition of sterically demanding side chains or fluorine side groups lead to improved thermal stability.[106,107] Substitution of Li-TFSI with Zn-TFSI also leads to an increased lifetime.[108]

In Conclusion, Spiro-OMeTAD and derivatives promising candidates in achieving stable and high efficient solar cells, despite still existing challenges regarding the stability.

Synthesis of the Spiro-OMETAD layer

"Spiro-OMeTAD" is spin-coated and oxidized in dry air overnight.

After the perovskite layer has been annealed, the substrates were cooled down to RT.

Precursor preparation

For the hole transport precursor, I dissolved 72.3 mg of 2,2′,7,7′-tetrakis(N,N- di-p-methoxyphenylamino)-9,9′-spirobifluorene (spiro-OMeTAD, Sigma-Aldrich, 99 % HPLC) with 28.8 µL of *tert*-butyl pyridine (*t*BP, Sigma-Aldrich, 96 %) and 17.5 µL of Li-bis(trifluoromethanesulfonyl)imide (Li-TFSI, Sigma-Aldrich 96 %) solution (520 mg in 1 ml acetonitrile) in 1 ml of chlorobenzene (Sigma-Aldrich, 99.8 %).The vial was tightly closed in dry air, sealed with parafilm and put into the direct sunlight for approximately 2 h. This step promotes the oxidation of the spiro-OMETAD and thus increases its hole-conductance.

Spin-coating

I dispersed 80 µL of HTL solution on the perovskite film (Figure 25). The substrates were spin-coated at 4000 rpm for 15 s. The samples were kept in dry air for 16 h in a desiccator in order to fully dry and oxidize the HTL film.

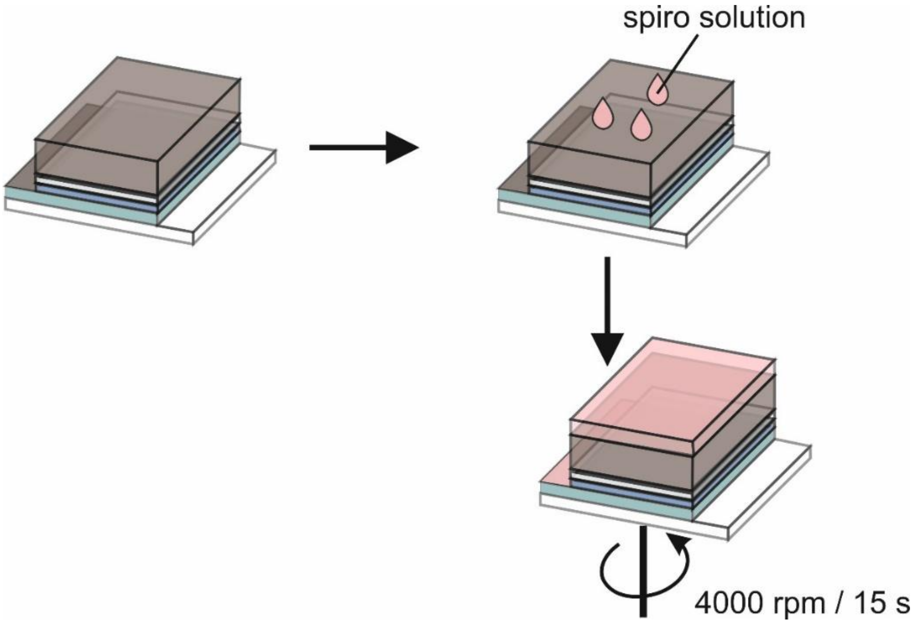

Figure 25: Synthesis of a Spiro-OMETAD film on a perovskite film.

2.3.5 The top electrode

The top electrode, the anode is in most cases a thin gold layer.

The requirements on the top electrode are less rigorous than on the bottom electrode. The anode must be stable, cheap, and easy to coat without damaging the layers underneath. Since the optical path of the illuminating light does not pass this electrode, it does not need to be transparent (Figure 4). However, J. Krantz et al point out, that a reflective back contact increases the light-harvesting efficiency.[109]

Typically, thin metal films are thermally evaporated onto the Spiro layer. F. Behrouznejad et al. studied the effect of different metal electrodes on the solar cell performance.[110] They constructed perovskite solar cells and applied either Ni, Cu, Cr, Au, Ag or P as the top electrode. The noble metals Au, Ag and Pt, yielded the highest efficiency, whereas cells with an Au top electrode demonstrated the highest lifetime. The authors attributed the differences in efficiency to the respective work function of the metal. Shunt resistance and open circuit voltage decreased with decreasing work function. K Domanski et al reported, that different metal electrodes possess different tendencies for releasing ions that migrate from the top electrode into the hole transport layer or perovskite layer and thus cause degradation.[111]

Thermal evaporation of the gold electrodes

After drying and oxidizing overnight in a desiccator, the spiro-covered substrates were placed into custom made shadow masks with three distinct electrodes that had an active area size of 4 x 4 mm² (Figure 26). A thin seed gold layer of 2 nm was thermally evaporated with a rate of 0.3 Å/s to reduce the thermic stress to the spiro layer.[94] Then, a 50 nm thick gold layer was evaporated with a rate of 1.2 Å/s. [112] The back contact area that remained uncoated with neither TiO_2 nor Au was carefully cleaned with a Q-tip and acetonitrile.

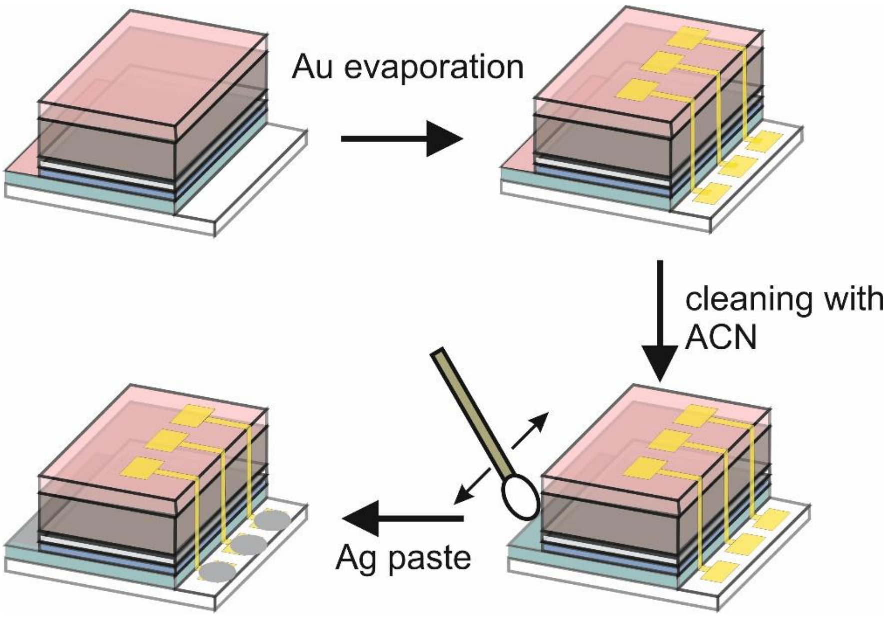

Figure 26:Thermal evaporation of Au electrodes.

2.3.6 JV measurements of Perovskite solar cells

I applied the silver paste on each electrode to improve the contact when measuring JV curves.[52] I used a solar simulator (ASTM class ABA Technologies SunLite TM) with a source meter (Keithley 2400). JV curves were recorded by varying the external bias from - 0.1 V to 1.2 V with 8.6 mV steps and a scan rate of 43 mV/s for the forward and backward scan. The cells were neither illuminated nor set under an external bias prior to any measurements. All measurements were conducted under ambient conditions. Each active pixel was covered with a shadow mask that defined the active area with a 3 x 3 mm² hole.

State-of-the-art $MAPbI_3$ based solar cells

I constructed a perovskite solar cell consisted of an FTO bottom electrode, a compact TiO_2 thin film with a mesoporous TiO_2 layer as the ETL, a $MAPbI_3$ layer as the photon-absorber, a Spiro-OMeTAD as the HTL and a 50 nm thick gold film as the top electrode. An adaptation of different published approaches enabled me to construct $MAPbI_3$ based solar cells with a peak efficiency of 19.5 %. (Figure 27).

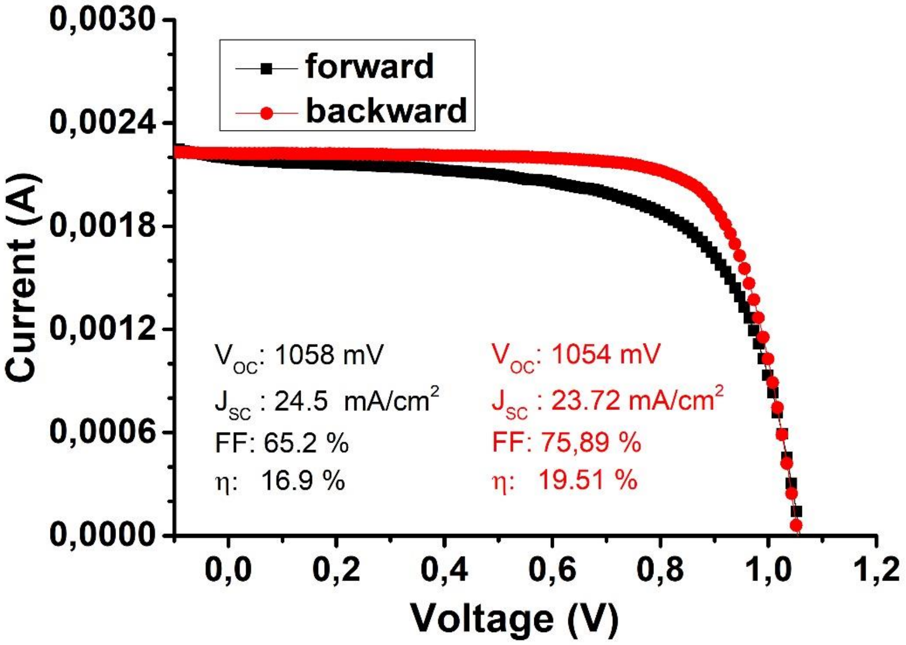

Figure 27: The forward and backward J-V-curve of my record cell using a mesoporous architecture and $MAPbI_3$ *as the photon-absorber. As common in* $MAPbI_3$ *based solar cells, this cell also displays a hysteresis in the JV. The origins of this hysteresis are beyond the scope of my work and are discussed elsewhere.*[17]

2.4 Conclusion

This chapter is aiming to provide the fundamentals for understanding the theory of solar cells in generals. In the first part, I discuss the four main parameters of a solar cell in general: the short circuit current density J_{SC}, the open cell potential V_{OC}, the fill factor FF and the cell efficiency. Furthermore, I explain, how the properties of the different layers affect these parameters. In the second part, I explain the working principle of the perovskite solar cell on the basis of its functional layers: the bottom F:SnO_2 electrode (FTO), the electron transport layer (ETL), the photon-absorbing perovskite layer, the hole transport layer (HTL) and the top metal electrode. For each layer, I discuss in detail the respective requirements and how they are met. Lastly, I display my synthesis approach for each layer that enabled me in construction –state-of-the-art $MAPbI_3$ based solar cells with a record efficiency of 19.5 %.

My work demonstrates the complexity of perovskite solar cell synthesis. The sheer number of different approaches for synthesizing each individual layer alone reflects the difficulty of reproducing any published recipe in different laboratories. The synthesis of each individual layer must be carefully adapted to the local ambient conditions. One often overlooked issue is the crucial influence of the local conditions within the spin-coater, e.g. the dimensions of the spin-coater volume, gas exchange with the surrounding glove box, local solvent vapor pressure, and substrate geometry. All these parameters influence the evaporation of the solvent during spin-coating which in turn critically influences the initial film formation and thus the overall film quality. Future publications should aim to either provide this information in order to facilitate the development of this exciting topic.

Chapter 3: Comparing the conductance of semiconducting metal oxides with cSFM quantitatively

3.1 How to compare the local conductance with cSFM

cSFM is a versatile tool to study the local conductance of thin films.

High efficient solar cells require transport layers with low electric resistance for the respective charge carrier while effectively blocking the opposite charge carriers. In the case of TiO_2, these films need a high conductance for electrons while blocking holes. A common way of evaluating thin films for PSC is the indirect approach to construct a full solar cell. There a low-quality TiO_2 films result in low efficient solar cells and vice versa. Moreover, the differences in interfaces between a high-quality and a low-quality TiO_2 thin film like the wettability could trigger differences in the subsequently deposited layers. However, this evaluating method has several disadvantages. In order to study the quality of one particular layer, five individual layers have to be synthesized. Thus random occurring defect in one layer may affect the total efficiency and produce distorted results for another layer. In addition, it takes far more time and consumes more energy and chemicals to produce a complete solar cell compared to a single TiO_2 thin film. Thus, a method is desired that allows a direct comparison of simple TiO_2 films on FTO.

A standard way of measuring the conductance or impedance is the four-point probes method. However, this method is not suited to probe the conductance of thin films of PSC due to two issues. First, the conductance of many thin films such as a 30 nm thick TiO_2 thin film is too low, to be measured macroscopically. The minimal threshold of measurable currents is above 10 nA for most devices which translates to a conductance below 10 MΩ. Second, the migration of charge carriers occurs perpendicular across the different layers within a solar cell. The four-point probes method measures the conductance parallel to a layer within the bulk. Thus, even if successful, the four-point probes method does not yield the conductance through the TiO_2 but instead the inter- or intra-grain conductance.

In this work, I evaluate semiconducting metal oxide thin films using conductive scanning microscopy (cSFM). This method gives access to information about the local morphology and adhesion as well as the local conductance. Therefore, different approaches in preparing such thin films can be compared and evaluated in regard to their electric resistance for electrons and hole blocking properties. I demonstrated that cSFM produces reproducible current values that allow both qualitatively and quantitatively comparison. In addition, macroscopic *IV* characteristics can be reproduced on a microscopic scale when measuring local *IV*-curves.

Accordingly, this chapter is aimed to explain the basics of the specific version of conductive scanning force microscopy that I used to study the surface and conductance of different materials.It has to be noted, that parts of this chapter are based on my publication from 2019.[52]

3.1.1 Working Principle of the peak force based JPK QI mode

For the “QI-mode” of JPK Nanowizard 4, a single force-distance curve is measured for each individual pixel.

For conductive scanning force microscopy, I used a JPK Nano Wizard IV to map the local conductance through the film. The maximum measurable current was 120 nA. The noise level of the current was approximately 1.5 pA. For cSFM, I used Pt/Ir alloy coated tips (Bruker, SCM-Pit V2) with a nominal spring constant of 3 N/m and a work function of approx. 3.9 eV.[113]

The cSFM was operated in the quantitative imaging mode (Figure 28 a). This mode records a force-distance curve at each pixel of an image. In detail, the SFM-tip is brought into contact with the sample surface at a defined setpoint force. In cooperation with E. Johannes, I studied the influence of setpoint force on the measured current.[114] He reported on his bachelor thesis an increase of current with increased setpoint force and identified a force of at least 15 nN to be optimal in order to achieve reproducible high currents. Within this work, I applied setpoint forces between 15-20 nN (Figure 28 b, black curve). This force guaranteed good electric contact between the tip and the surface.

Furthermore, these forces were observed to neither damage the tip nor the surface for at least 3 million pixels *(see below: The influence of tip erosion for the QI mode).* Simultaneously, the electrical current was measured during each force-distance curve at a tip-sample voltage of in the range of -2 V to 2 V *(*Figure 28 *b, red curve).* For the retraction from the surface, a defined length indicates for the z-piezo depending on the roughness of the surface. Standard z-length varied from 100 nm for smooth Au surfaces to 500 nm for rough perovskite films. The measured current increases in most cases after the tip-sample contact until a maximum current value was measured at the highest contact force. This increase of current with increasing setpoint force can be attributed to two factors: an increase of the contact area between tip and cantilever as well as penetration of any residual low-conducting contamination on the tip or surface. As a representative value for the local conductance, we used the maximum current value of the approach curve. After the maximum setpoint force is reached, the tip retracts from the sample surface (Figure 28 a, step 2) and is moved to the next pixel (Figure 28 a, step3), where the procedure is repeated. The duration needed to perform a full force-distance curve on one individual pixel is called pixel-time. Depending on the individual sample a tradeoff must be found between fast scanning speed and a low noise level of cantilever deflection. E. Johannes reported a slight increase of measured current with increased pixel time up to a pixel time of 10 ms.[114] Within this work, I chose a pixel time of 7 – 10 ms.

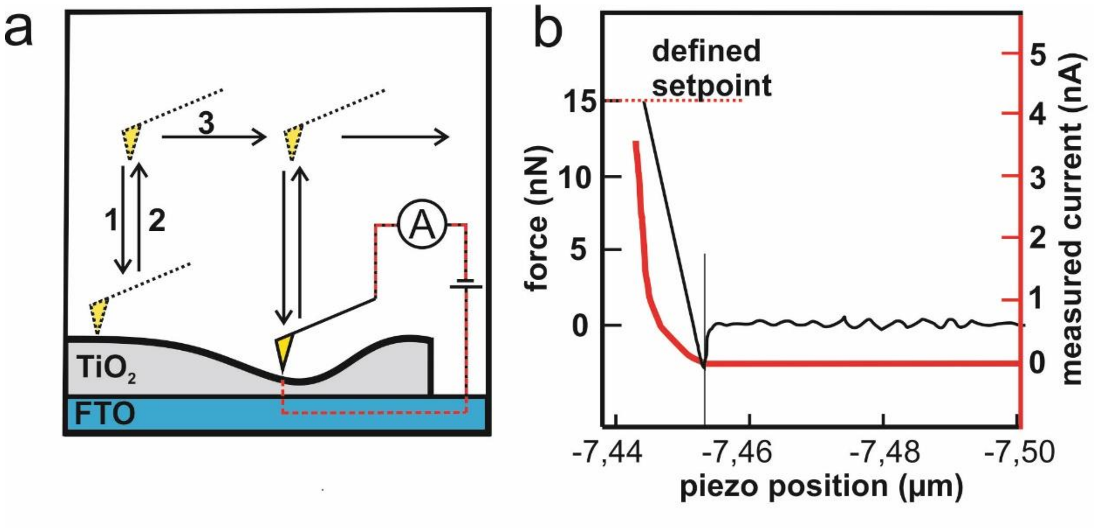

Figure 28: a) Working principle of the "Quantitative Imaging" peak fore- cSFM mode: For each pixel, a single force-distance curve is measured, consisting of an extension (1) and retraction curve (2), before the tip moves to the next pixel (3). A current image is compiled from the maximum current during the extension curves. b)shows an exemplary force-distance curve with the respective current curve (red) for a high conducting pixel of an annealed and UV-ozone treated TiO_2 thin film on FTO. In this particular example, a maximum current of 3.6 nA was measured with an applied external bias of 1 V and a setpoint force of 15 nN.

To rule out the influence of individual cantilever tips and different measurement conditions, every series of measurements was conducted on the same day within a few hours with the same cantilever. Thereby, I was able to compare absolute values for similar samples, which were prepared for one set of experiments. Although absolute current values varied slightly for different sets of preparations of similar samples, the relative changes were reproducible.

During a "QI" mode-cSFM measurement, the force and the flow of current are recorded over the complete circle. Thus, two curves are produced while a single force-distance curve: a so-called extend curve and a retract curve (Figure 29).

The flow of current depends on the distance between the cantilever tip and the sample. For almost every force-distance curve, the current increased for the retraction curve compared to the extend curve. This increase in current can be explained with the formation of water bridges. In ambient conditions, a thin water film forms on every polar surface. As soon as the cantilever snaps into contact, this water film is penetrated.

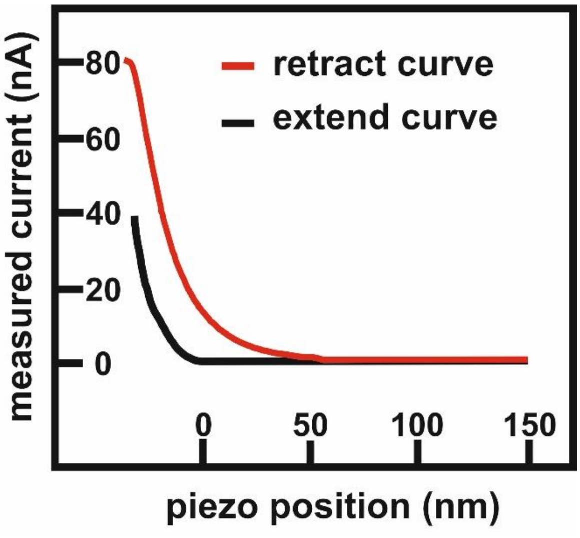

Figure 29: Example of the measured current during an extend- and a retract-curve for a single force-distance experiment during a cSFM measurement in the "QI"- mode with a setpoint force of 10 nN and an applied bias of 1.5 V.

Upon retraction of the cantilever, capillary forces form a water bridge between the surface and the cantilever. This bridge act as an additional electric contact.[115] In addition, if the applied external bias exceeds 1.2 V, water molecules can be electrochemically split and thus increase the number of conducting ions within the thin water film. Thus, it is possible that during the retract curve the conductance of the thin water film is increased. Also, the surface can be altered locally, while being in contact with the tip.[116] In order to minimize the effects of surface alteration and the influence of humidity, only the extend curves were considered for comparison with pixel times below 15 ms.

Single force-distance curves are insufficient for comparing different substrates

Many samples like commercial F:SnO_2 films possess a rough surface that must be considered when comparing the local surface conductance of different samples. A direct comparison of single force-distance curves can lead to distorted results since the local geometry strongly affects the measured adhesion and current flow (Figure 30). When the cantilever tip is positioned at a local peak at the FTO surface, the effective contact area between the cantilever tip and the surface is minimized which leads to increased contact resistance. If the cantilever tip is positioned at a local ridge at the FTO surface, the effective contact area is increased which decreases the local contact resistance. Variations in the measured current occur in the order of 5 magnitudes even on the same substrate at different pixels.

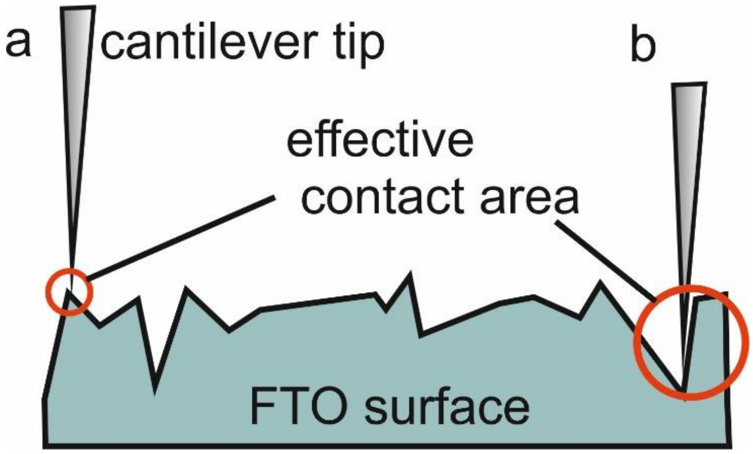

Figure 30: The effective contact area of the cantilever tip with a rough surface of FTO as an example. a) Local peaks in the surface lead to a small relative contact area and thus to high contact resistance. b) local ridges in the FTO topology can lead to a large effective contact area between the cantilever tip and the FTO substrate and thus lead to small contact resistance.

Likewise, larger effective contact areas can also lead to an increased adhesion between the tip and the surface, when the cantilever is retracted from the surface. Therefore, single force-distance curves cannot discriminate between changes of the local properties due to surface defects or local morphology. A whole image, on the other hand, represents an ensemble of single force-distance curves and therefore even out the effect of the local topology. Moreover, the roughness must be monitored as well, since changes in the surface geometry can alter the average contact area and thus the average current flow.

The median current is suited to represent the conductance of a respective area.

For each measurement, I recorded a height channel, a current channel, and an adhesion channel, that produced a height image, a current image and an adhesion image (Figure 31).

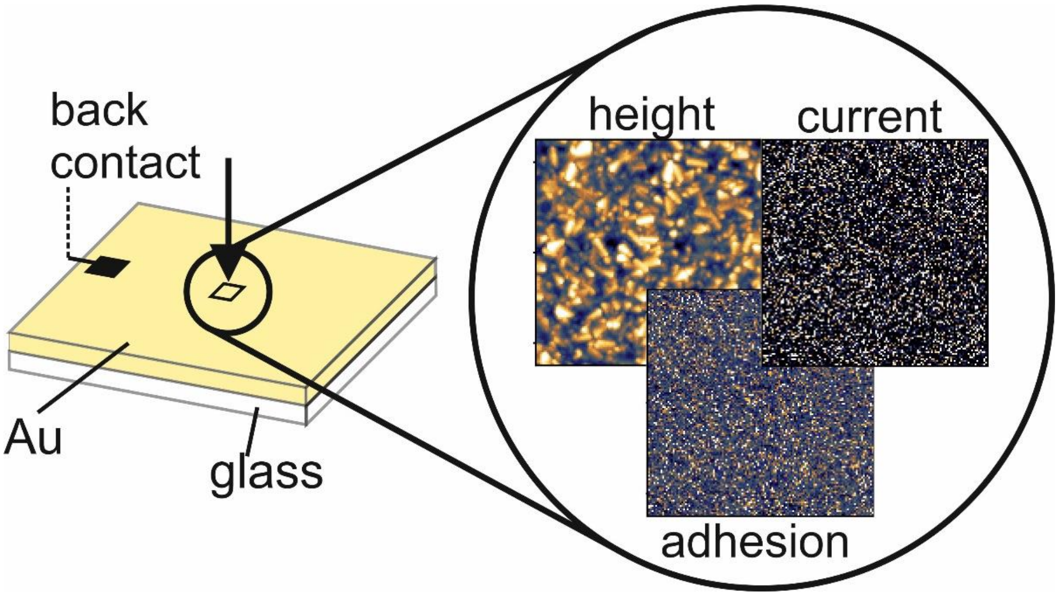

Figure 31: Measurement principle of cSFM on Au. The square represents the measured image. The cantilever tip is depicted by the arrow.

I used Gwiddion 2.53 for analysis of each channel. The height image allows analysis of the topology and roughness of different samples and reveals any potential changes after specific treatments. Changes in the local properties, like stickiness due to contaminations, can be visualized with the adhesion channel. The current image allows a comparison of the local conductance of different samples. Since single force-distance curves and the respective current flow do not transport any statistical significance, I compared the median of the distribution of currents of each pixel of a current image. Almost every sample displayed a non-Gaussian distribution of currents that spanned over five orders of magnitude for an image (Figure 32). Most of the pixels displayed a current in the low pA regime whereas a few pixels have currents up to the detection limit of 120 nA. Thus, the most commonly used arithmetic mean, or "average" is not suited to adequately describe the distribution of local conductance of an area.

$$Av = \frac{1}{n}\sum_{i=1}^{n} a_i \qquad [1]$$

Since the average (AV) is the sum of each current (a_i) divided by the number of summands (n), few very high currents distort the mean current to higher values, that not represent the conductance of respective areas (Formula 1). Therefore, I used the median of currents that separates the greater and the lesser halves of a data set and therefore acts as a threshold that half of all currents exceed.

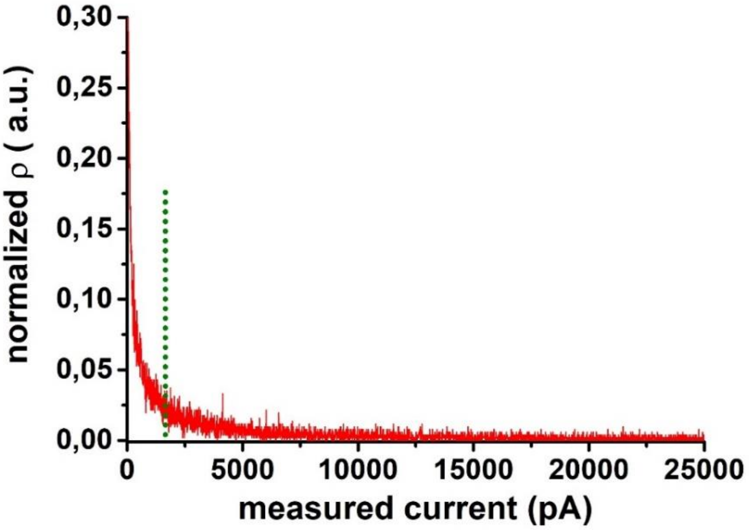

Figure 32: Exemplary normalized distribution of measured currents of a cSFM current image. The image was measured on a gold sample with a setpoint force of 20 nN, a Z-length of 300 nm, a pixel time of 10 ms and an applied external bias of 0.020 V. The image had a size of 5 x 5 µm with a resolution of 128 x 128 pixels. Thus, each mean was calculated of 16.384 individual force-distance curves. The green dotted line marks the median of the data set, and thus is used as the representation of the conductance of the respective area.

3.1.2 Sample preparation for cSFM

Copper tape and silver paste guaranteed a reproducible and low resisting electric contact

The electric contact between the sample and the sample holder drastically impact the measured currents during a cSFM experiment. A reproducible and low electric resistance between the sample surface and the cSFM module permits a quantitative comparison of different substrates.

The standard sample-holder of the JPK Nanowizard 4® has a soft clamp that secures the substrate and locks it in place. Additionally, it establishes an electric contact between the sample surface and the contact area for the cSFM module (Figure 33). This contact area is electrically connected with the cSFM module via a gold pin with a spring.

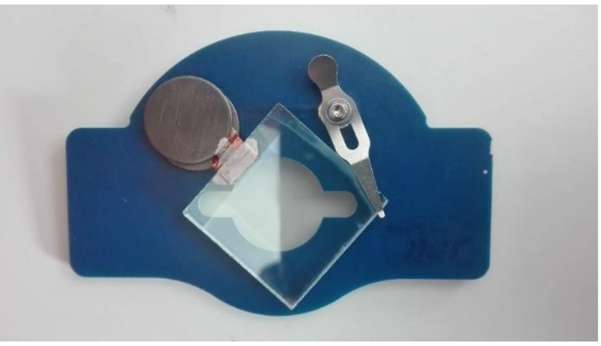

Figure 33: Sample contacting for measuring cSFM on a coated FTO substrate. Two metal discs are glued together with copper-tape and the sample surface. An additional conductor path of silver paste between the sample surface and the metal disc guaranteed a reproducible and low electric resistance.

This design is insufficient to guarantee a reproducible and low electric contact as I tested with a standard multimeter. The measured electric resistance varied from 60 Ohm to over 1000 Ohm for the same substrate.
Thus, each sample was connected to two metal discs with copper-band and silver paste. These metal discs act as a spacer to compensate for the thickness of the FTO substrates, as well as an electric bridge. An additional conductor path was painted onto the copper-tape, connecting the metal discs and the substrate surface directly. Thus, a producible electric contact below 20 Ohm could be realized between the metal discs and the substrate surfaces.

3.2 cSFM measurements on Au thin films

Macroscopic IV characteristics can be reproduced on Au films with cSFM

In order to establish a viable measurement routine, that allows comparing different thin films, I used a highly conductive thin gold film as a reference system. I conducted a cSFM measurement on a 50 nm thick gold layer on a glass slide. I conducted 27 consecutive measurements on a 50 nm thick Au film on glass with a setpoint force of 20 nN, a Z-length of 300 nm and a pixel time of 10 ms. Each image had a size of 5 x 5 µm² with a resolution of 128 x 128 pixels. For each image, a new area was measured in order to prevent any influence from previous measurements. I plotted the measured median current against the applied bias to generate a microscopic *IV*-curve (Figure 34).

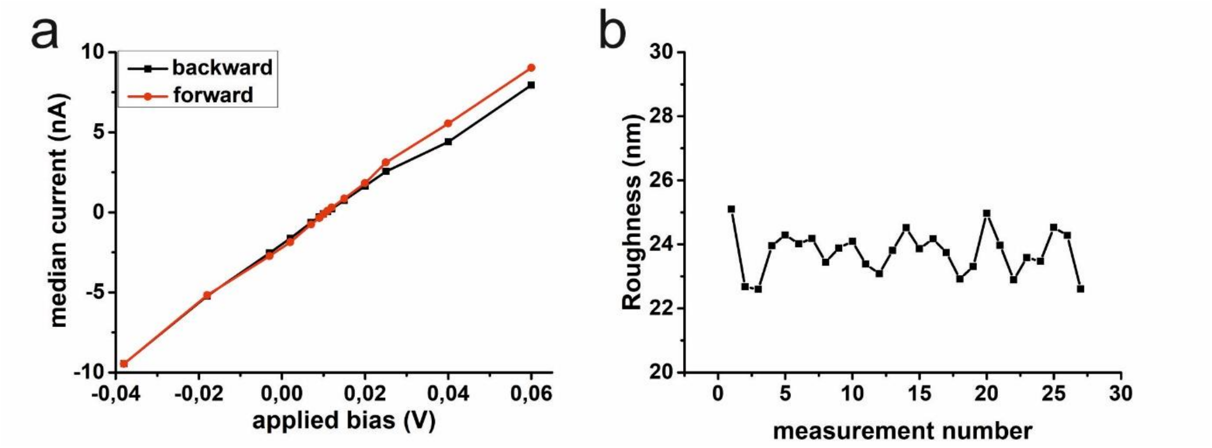

Figure 34: a) IV curve of a 50 nm thick Au film on a glass substrate. Measurements were conducted at an initial bias of +0.06 V, which was decreased stepwise to -0.038 V (black curve). Subsequently, the bias was increased stepwise again to +0.06 V (red curve). Each median current corresponds to a single image with 128 x 128 pixels. b) Development of the measured roughness of each image with progression measurement number.

Every data-point represents an ensemble of 128 x 128 individual current measurements during a force-distance curve. I plotted the median currents without error bars since they do not offer any additional and meaningful information. For most measurements, the standard deviation is two orders of magnitude higher than the respective value because the distribution of the ensemble is not Gaussian with few very conductive pixels. The median itself already possesses statistical information in separating the greater and the lesser halves of a data set. I found a reproducible metal conductor characteristic for both forward and backward scans, as expected for a gold film.

Ohm's law $U = R \cdot I$ allows calculating the resistance of the system. When plotting both curves with a linear fit $= bx + a$, the slope of the linear fit is $b = 1/R$. I found a contact resistance of 5.7 MOhm for the forward curve and 5.3 MOhm for the backward curve. This resistance is a combination of the bulk resistance of the gold layer, the electric resistance of the cantilever, the contact resistance between the tip and the surface and the contact resistance between the cantilever and the clamp that secures it in place. The bulk resistance of the gold layer is within the range of 1 Ohm since gold is an excellent conductor. Likewise, the resistance of the conducting Pt/Ir coating and the contact resistance between the cantilever and the metal clamp are expected to be orders of magnitude lower than 5 mOhm. Therefore, the main contribution to the estimated values is the contact resistance between the tip and the gold surface. These results demonstrate, that cSFM is suited in measuring an electric resistance in the M Ohm regime that is not accessible with four-point probes measurement.

It has to be mentioned, that I measured a current of approximately -1.6 nA with an applied bias of 0 V. The direction of current flow switched between an applied bias of 0.011 V and 0.010 V from +59 pA to -98 pA. This observation can be explained with a small offset within the voltage generator and amplifier of the JPK Nanowizard IV of approximately 0.01 V. Since the setup allows to apply an external bias from -10 V to +10 V, this offset corresponds to an arrow of approximately 0,05 %.

The average roughness over every image was 23.8 ± 0.7 nm. When plotting the measured roughness of each image against the measurement number, I obtained comparable values on different areas on the sample without any trend that would indicate changes of the cantilever tip of the surface morphology (Figure 34 b). Therefore, comparable current and topology images over the course of 27 consecutive measurements on a gold surface indicate that the Pt/Ir tip is not altered to a significant degree that would influence cSFM measurements.

Summary of cSFM measurements on Au thin films

The QI mode of the JPK Nanowizard IV® is suited to yield reproducible and quantitative comparable median currents and roughness on a gold film on glass substrates. Macroscopic *IV* characteristics were reproduced on a nanoscale. I did not observe a change in roughness or *IV* characteristic over the course of 442368 single force-distance curves (e.g. 27 images each with 128 x 128 pixels), which would indicate a significant tip erosion. These results indicate, that cSFM measurements yield reproducible and thus quantitatively comparable results when the sample is measured with the same cantilever. Thus, I established a set of parameters for comparing the local conductance with cSFM measurements on thin films.

3.3 cSFM measurements on FTOs

Fluorine doped tin oxide substrates used as conductive and transparent substrates for a variety of applications and are the most frequently used substrates for perovskite solar cells. Since every photon-generated electron must migrate into and through the FTO, its local microscopic electric behavior is of great interest. Thus, its surface conductance plays a crucial role for charge injection from adjacent layers.

For thin-film electronics, local electric properties can vary due to impurities, surface vacancies, pin-holes, and other surface defects. Macroscopic methods like four-probe measurements only give access to average information about a specific ensemble of areas and local properties like surface potential barriers might stay concealed. I demonstrated, that cSFM is a valuable tool for comparing the local electronic properties of semiconducting metal oxides like FTO qualitatively and quantitatively.

3.3.1 Local *IV* measurements with cSFM on FTO substrates

cSFM can measure reproducible median currents on the same FTO substrate in different areas.

In order to verify that comparable values can be measured on the same FTO substrate at different locations, I manually cleaned a substrate with Hellmanex® and Milli-Q-water (Figure 35. After 30 min of argon-plasma treatment, the sample was directly transferred to the cSFM setup.

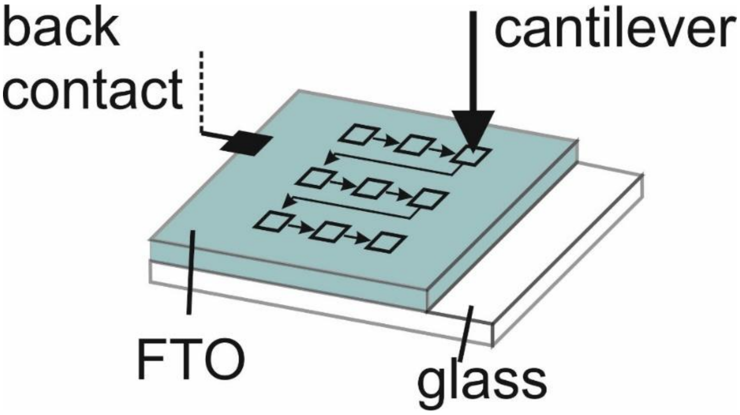

Figure 35: Series of consecutive measurements on the same FTO substrate in different areas. Each square represents a new measured area, for which each a singe current image, height image, and adhesion image were recorded. Thus, each point in Figure 36 represents the median current of one respective current image. A set of measurements was recorded with a setpoint force of 20 nN, a Z-length of 300 nm, a pixel time of 10 ms and an external bias of 1.5 V. A scanning area of 5 x 5 µm[2] *were recorded with a resolution of 128 x 128 pixels. Each image was recorded in a new area in the center of the substrate with 5µm distance to the previous measurement. Furthermore, each measurement was conducted with the same cantilever within 2 h.*

For each measurement, a new area was selected in order to demonstrate that comparable values can be obtained in different areas on the same substrate. Otherwise, a comparison of different samples would not be meaningful. Moreover, new areas for each measurement guaranteed minimal influence or crosstalk from previous measurements.

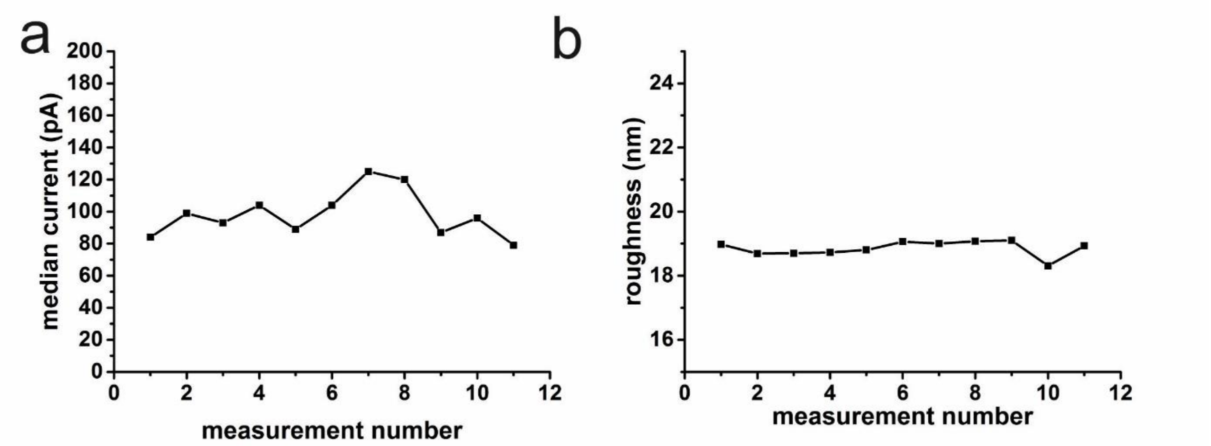

Figure 36: Development of the measured current over the course of consecutive measurements each on a new area of a manually cleaned and plasma cleaned FTO substrate. b) Development of the measured roughness on over the course of consecutive measurements each on a new area of a manually cleaned and plasma cleaned FTO substrate.

I did not observe any trend when plotting the measured median current and roughness over the number of measurements. An average of the median current of 98.2 ± 13.7 pA was measured. Therefore, cSFM can measure comparable values on semiconducting metal oxide layers like FTO. Since cSFM yields comparable values on the same substrate, when using the same cantilever over the course of several consecutive measurements, cSFM can also measure comparable values on different substrates. Moreover, I demonstrated that manual cleaning followed by 30 min of argon-plasma treatment is sufficient for creating a clean and homogeneous surface that is required for both reproducible cSFM measurements and solar cell preparation. Within the time frame of this set of measurements, no significant recontamination occurred that would influence the measured local conductance.

A very narrow distribution of roughness was measured with an average of 18.9 ± 0.2 nm without any trend over the course of consecutive measurements. Thus, I demonstrated that no significant tip alteration occurs on hard metal oxide surfaces when using the peak-force “QI” mode.

cSFM can reproduce macroscopic *IV*-behavior on a nanoscale on FTOs.

In contrast to gold, tin oxide is not a metal-like conductor but a highly doped semiconductor. In order to demonstrate, that cSFM is also suited to analyze the local I-V characteristics of a semiconducting metal oxide, I conducted consecutive cSFM measurements on a freshly cleaned and argon-plasma treated FTO substrate with varying applied external bias while recording the current. Since the cantilever is coated with a Pt/Ir layer, the contact between metal tip and semiconducting surface acts as a Schottky-diode.

The applied initial external bias of 1.5 V was decreased stepwise to 0 V and then inverted up to -1.5 V (Figure 37, black curve). Subsequently, the bias was increased stepwise again to 0 V and further on up to 1.5 V (figure 9, red curve).

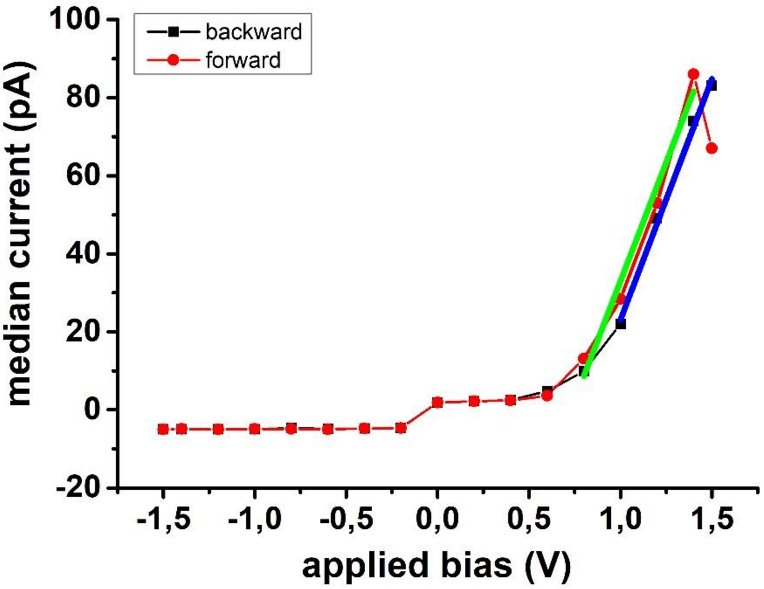

Figure 37: a) Local I-V-curves of manual cleaned and Ar-plasma treated FTO. Measurements were conducted starting at an initial bias of +1.5 V, which was decreased stepwise to 0 V and then inverted up to -1.5 V (black curve). Subsequently, the bias was reduced stepwise again to 0 V and inverted up to 1.5 V (red curve). A linear fit yields the conducting state voltage of 0.81 V for the forward scan (green line) and for the backward scan (blue line) of 0.73 V. b) The roughness did not display any trend over the course of 35 measurements.

A diode characteristic on a local scale with a conducting state voltage of 0.81 V in forward direction and 0.73 in backward direction was measured. The SFM-tip has a Pt/Ir-metal coating with a work function of ~3.9 eV.[113] M. G. Helander et al. reported a work function of 5.0 ± 0.1 eV for fluorine-doped tin dioxide.[117] Therefore, according to the Schottky-Mott rule, a Schottky barrier height of approximately 1.2 eV is expected. The measured Schottky barrier height of 0.73 V and 0.81 V below the expected value. A deeper study of the reasons for that difference is beyond the scope of this work. Nevertheless, strong variations from the Schottky-Mott rule are common for commercial diodes. It has been reported, that band bending at the interface strongly depends on the contact between the metal and the semiconductor and is further altered by surface states, oxide layers at metal surface, contamination, water bridges and other surface effects between the metal and the semiconductor.[118,119]

Therefore, my results meet the expectations and local diode characteristics can be measured with cSFM.

Plasma cleaning is crucial for measuring comparable currents

Proper preparation of an FTO substrate is important to achieve reproducible results. Simple manual cleaning removes any contamination that is visible with the naked eye. However, additional UV-ozone treatment or plasma-treatment step is crucial in order to properly clean the substrate for further thin film synthesis.

In order to demonstrate this requirement, I performed a set of measurements on an FTO substrate that was manually cleaned as described above without any further plasma cleaning. When recording a consecutive set of measurements on the same substrate at different areas for each measurement, strong variations in the measured current occurred (Figure 38). This variation in current did not display any trend that would indicate progressing modification of either the surface or the cantilever tip.

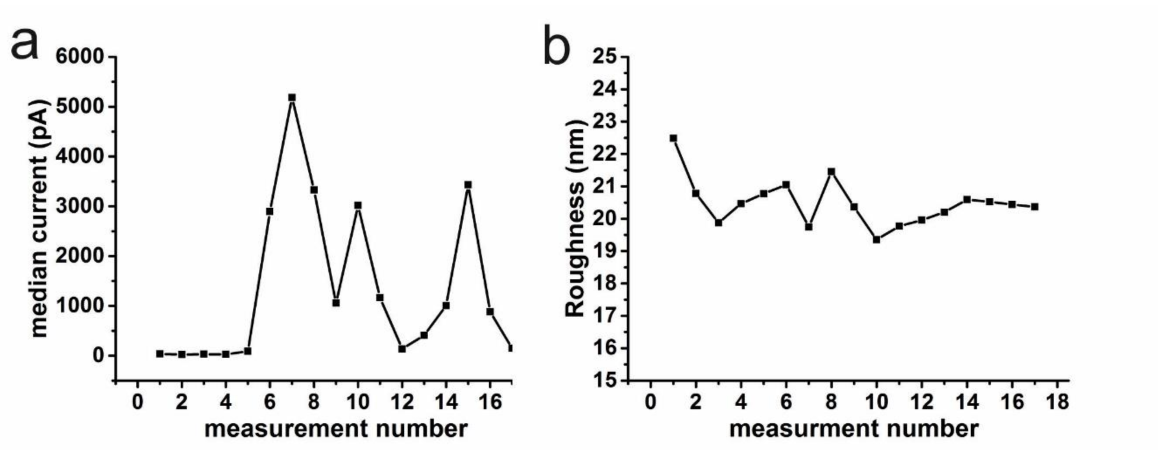

Figure 38: a) Development of the measured current over the course of consecutive measurements each on a new area of a manually cleaned FTO substrate. b) Development of the measured roughness on over the course of consecutive measurements each on a new area of a manually cleaned FTO substrate. For each measurement a new area was recorded with a setpoint force of 15 nN, a z-length of 150 nm, a pixel time of 8 ms with an applied bias of 1 V. A resolution of 50 x 50 pixels were recorded of an area of 2.5 x 2.5 µm.

The median current varied from below 100 pA to over 5500 pA for the same substrate. This strong variation in the median current can be attributed to organic contaminations at the surface. Contaminations of the surface occur either due to physical contact with the substrate's surface or due to the adsorption of organic compounds in ambient conditions. In addition, insufficient manual cleaning could lead to an accumulation of organic compounds in the cavities of the rough FTO surface. A contrasting juxtaposition of the measured median current with the measured local average adhesion displays no strict correlation of adhesion and current. Although a low adhesion was accompanied by a high median current for the 5th – 10th measurement, no such correlation was observed for the 14th – 16th measurement (Figure 39). Depending on the local properties, the organic compounds can act as an insulating layer and thus reduce the flow of current while increasing the local adhesion.

However, thin or soft patches of contamination can be penetrated by the cantilever tip and thus do not increase the electric contact resistance.

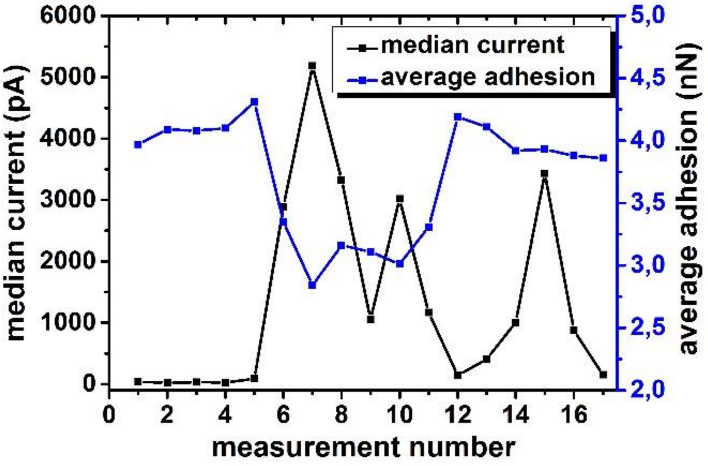

Figure 39: A contrasting juxtaposition of the measured median current with the measured local average adhesion. Low conducting areas displayed a high adhesion and vice versa.

Therefore, a post-cleaning treatment is crucial in order to prepare FTOs reproducible for further thin film synthesis. Moreover, standard SFM techniques fail to visualize thin layers of organic contaminations reliable, since neither changes the local adhesion nor in the local roughness correlate strongly with a measured median current.

3.3.2 Summary of cSFM measurements on FTO substrates.

cSFM enables the visualization of thin-film contaminations, that are not displayed by the adhesion image of standard SFM measurements.

I demonstrated, that cSFM can produce comparable current values on different areas of an FTO substrate over the course of 12 consecutive measurements. No trend was observed in the roughness, which would indicate tip erosion. Moreover, I demonstrated that cSFM can be used to measure local I-V characteristics of semiconducting metal oxides on a nano-scale. I found no strong correlation when comparing the measured median current with the local adhesion or roughness. Moreover, untreated samples did not display changes in the roughness compared to treated samples. cSFM yielded an average roughness of 20.5 ± 0.7 nm. The average adhesion only changed around 1.5 nN for high conducting pixels images compared to low conducting images. Therefore, thin contaminations are hardly visible with standard SFM techniques. However, an FTO sample without any post-cleaning treatment exhibited strong variations in the measured median current in the range of three orders of magnitude. Thus, these findings underline the necessity of plasma treatment of FTO surfaces after manual cleaning and indicate the possibility of surface modification with plasma treatment.

3.4 cSFM measurements on TiO2 samples

The electron transporting layer TiO_2 plays a key role in perovskite solar cells. It must block positive charge carriers while efficiently transporting photo-generated free electrons from the perovskite layer to the FTO substrate. Therefore, the local charge transport properties of the TiO_2 layer are of great interest for perovskite solar cells as well as for other electronic thin film applications like thin-film transistors or photocatalysts.[120,121]

I demonstrate that cSFM measurement can produce qualitatively and quantitatively comparable values on TiO_2 thin films when measured directly after synthesis. In contrast to other methods like the 4-point probes method or terahertz measurements, cSFM allows imaging the local conductance perpendicular through the TiO_2 layer instead of parallel to the surface. This direction of current is ensured by attaching the back contact of the cSFM device at the FTO substrate. The electric current flows perpendicularly from the cantilever tip through the TiO_2 layer into the FTO with such a setup (Figure 40).

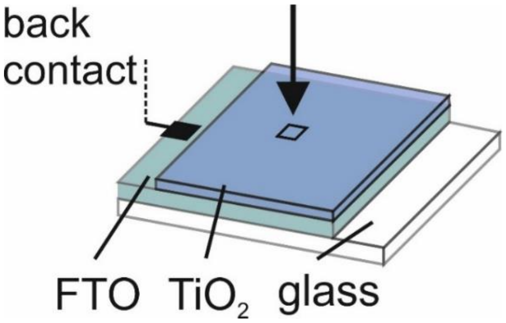

Figure 40: While spin-coating an FTO with $TiCl_4$ a small area on one side is covered with Scotch Tape. After removing the tape and annealing the film, the TiO_2 free area is contacted with the back contact. Thus, the current flows from the cantilever perpendicular through the TiO_2 into the FTO. Each measurement consists of a current image, a height image, and an adhesion image. Giving the local height, adhesion, and conductance through the TiO_2.

cSFM yields quantitatively comparable measurements for different TiO_2-coated substrates

In order to compare the effect of different synthesis routes and preparations for TiO_2 thin films on FTO, I must verify, that I can produce TiO_2 thin films reproducible and measure their conductance reliability. For that, I synthesized 12 individual samples of TiO_2 covered FTO substrates as described above (chapter 2). A 30 nm thick TiO_2 layer was spin-coated on a freshly cleaned FTO substrate that was Ar-plasma treated for 30 min. Every substrate was measured only once with a setpoint force of 20 nN, a Z-length of 150 nm, and a pixel time of 8 ms in order to minimize recontamination during exposure to ambient hydrocarbons or due to surface modification from previous measurements (chapter 5). For each image, an area of 5 x 5 µm^2 with a resolution of 128 x 128 pixels was recorded. An external bias of 2 V was applied.

A set of median currents could be obtained with an average median current of 13.85 ± 7.0 pA and a roughness of 18.45 ± 0.9 nm when measured directly after synthesis (Figure 41).

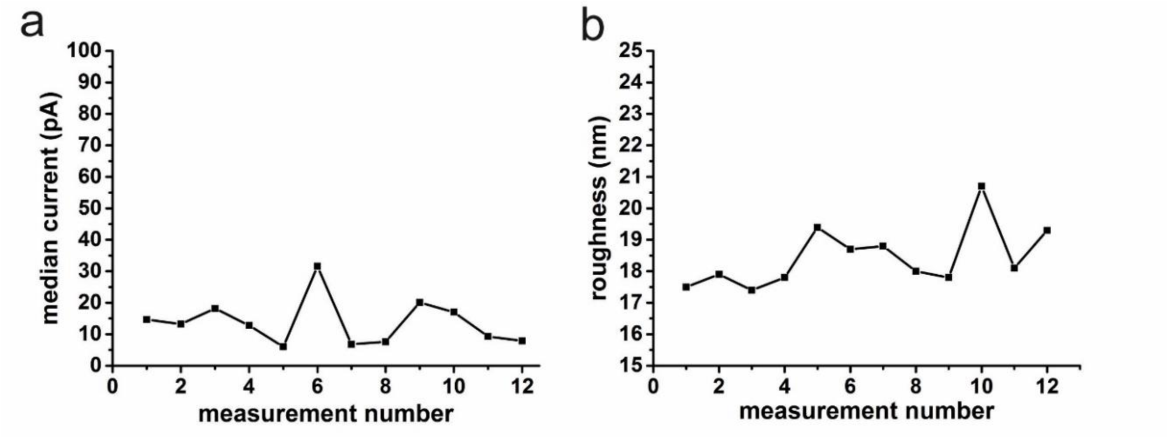

Figure 41÷: Development of the measured current over the course of consecutive measurements each on a new substrate of TiO2 film on a cleaned FTO substrate with twice the size as in Figure 10. b) Development of the measured roughness on over the course of consecutive measurements.

Therefore, the synthesis routine yields reproducible TiO_2 thin films with comparable local conductance, as verified with cSFM.

Recontamination and erosion

Recontamination of the TiO2 surface affect the conductance on a larger time scale

Freshly synthesized TiO_2 is expected to be free of contamination since organic compounds do not adsorb on the freshly formed film at 500 °C at ambient conditions. However, TiO_2 surfaces are contaminated with hydrocarbons when exposed to ambient conditions within a few hours. [122] Adsorbed hydrocarbon change surface properties like wettability and the local conductance.[123]

This recontamination might not be detectable via changes in the adhesion of a cantilever but it does critically influences the local conductance of TiO_2 thin films. Consecutive cSFM control measurements on a freshly prepared and UV-ozone treated sample on an argon-plasma cleaned FTO revealed a declining current over a period of 12 h (Figure 42).

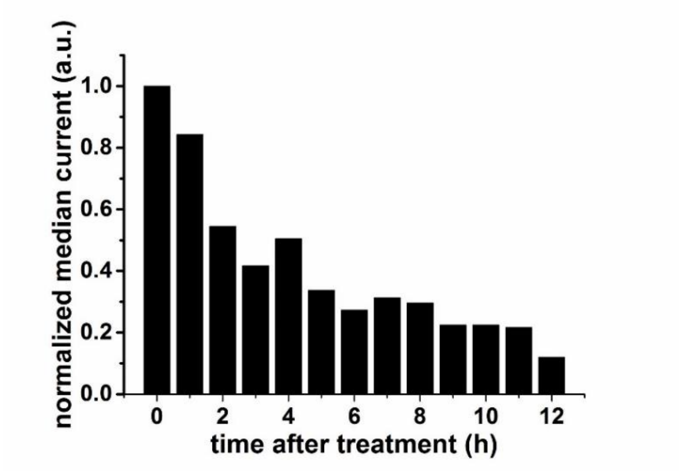

Figure 42: Development of median current overtime on a TiO_2 thin film on an argon-plasma cleaned FTO. Each image was recorded on different areas on the same substrate with a peak force of 30 nN, a z-length of 300 nm, a pixel time of 10 ms and an applied external bias of 2 V. Each image had a size of 10 µm x 10 µm with a resolution of 256 x 256 pixels.

After 12 h the median current value had dropped to 12 % of the initial value. Therefore, I conclude that TiO_2 surfaces should be processed directly after synthesis (and optional UV-ozone treatment) for electric applications as perovskite solar cells.

The influence of Tip erosion for the QI-mode

Cantilever tip erosion is negligible for the QI-mode.

Metal oxides as TiO_2 are hard materials that have strong abrasives properties.[124,125] Therefore, the cantilever tip could also take damage with progressing measurements, when imaging hard surfaces. Depending on the nature of such erosion, the contact area of the conductive coating can be increased or decreased (Figure 66).

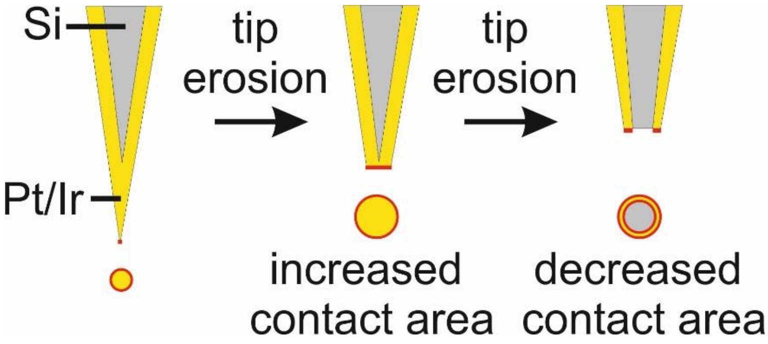

Figure 43: Tip erosion can lead to an increased or decreased contact area of the conductive coating with the surface.

Therefore, the measured median current could also be affected by tip erosion with consecutive measurement on hard surfaces as metal oxides which would render meaningful comparison of different thin films impossible. I did not observe any decrease in measured roughness with progressing measurements which would indicate a blunting cantilever tip. However, the cantilever has an average tip diameter of 20 nm. An increase of tip diameter about a few nanometers probably would not affect the measured roughness but do affect the measured current.

Therefore I conducted two measurements on a one day old, untreated sample that already was contaminated by exposure to ambient conditions. Therefore, that substrate did not change its conductance over time due to new recontamination. The first image was recorded with a fresh cantilever. The second image was measured with the same cantilever after it has been used for 12 h of constant measurement on other TiO_2 substrates (Figure 44). Within this period, over 50 images were recorded, each with a resolution of 256 x 256 pixels. This resulted in over 3 million individual force-distance curves measured with that cantilever.

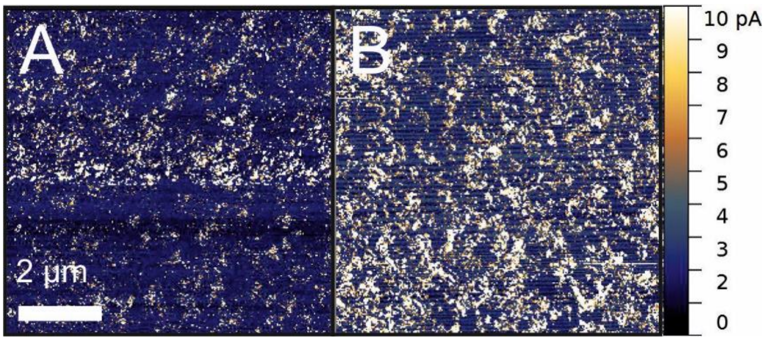

Figure 44: cSFM image of the same sample with a pristine cantilever (A) and the same cantilever after over 3 million individual force-distance curves.

With the fresh cantilever, I measured a median current of 2.9 pA, which was well above the noise level of 1.5 pA. Although the current image appeared to be changed, only a minor change of the median current was measurable when using the used cantilever. The median current rose only slightly from 2.9 pA before to 3.0 pA after. Therefore, I concluded that tip erosion plays only a minor role for the measured currents. Accordingly, peak force based cSFM techniques can be used to not only compare current images qualitatively but also quantitatively when using the same cantilever for different hard, semiconducting metal oxide samples.

Summary of cSFM measurements on TiO_2 thin films at FTO substrates

cSFM proofed to be a viable tool for analyzing semiconducting metal oxide films on a nanometer scale. I studied TiO_2 thin films on FTO substrates on a local scale and found comparable median currents on different TiO_2 thin films that have been synthesized in a similar fashion. Consecutive measurements over a period of 12 h revealed recontamination of TiO_2 in ambient conditions that resulted in a drastic decrease of local conductance. Nevertheless, comparable measurements can be conducted on TiO_2 thin films within a time window of under 1 h.

Lastly, I found no signs of tip erosion that would alter the measured local current after over 3 million individual force-distance curves on hard materials as TiO_2.

Therefore, I presented that cSFM is a viable tool to study the local conductance and I-V-characteristics of metal type conductors and metal oxide semiconductors. This tool allows both qualitative and quantitative comparison of the electronic surface properties of thin films, which enables a fast and easy evaluation of film quality for perovskite solar cells, without the need to construct a full solar cell.

Chapter 4: Defect engineering of metal oxide surfaces

Introduction

The surface of a substance crucially influences its general properties. This fact is particularly true for all kinds of nano-sized systems, be it nanoparticles, thin films, droplets, mesoporous materials since the ratio of surface-bound atoms to bulk atoms increase with decreasing film thickness, particle or droplet size.[126–128]

Surface defects are one of the main parameters that determine surface properties. Common surface defects in metal oxides are point defects as oxygen vacancies.[38] Oxygen vacancies act as reactive centers for catalytic systems or as recombination centers for light-emitting systems.[129,130] For n-type metal oxide semiconductors, oxygen vacancies also act as dopants or electron traps, depending on their location within the crystal. In order to control the surface properties of a respective material, an easy, cost-effective and reproducible tool is desired in order to engineer these surface defects for the respective purpose. Plasma treatment is such a tool.

In literature, more and more publications report the beneficial effect of plasma treatments for various applications.B. Bharti et al. reported, that air plasma treatment increases the concentration of surface oxygen vacancies in Fe and Co-doped TiO_2.[131] They found a redshift of the absorption of Fe doped TiO_2 films and a blue shift for Co-doped films after plasma treatment. S. R. Hammond et al. studied spin-coated MoO_3 films and found an increase of work function after oxygen plasma treatment.J. Pan et al. plasma modified SnO_2 nanowires and increased the concentration of surface oxygen vacancies for increasing

Within this work, I investigated how metal oxide semiconductors $F:SnO_2$ and TiO_2 can be altered with regard to their surface electronic and chemical properties. Surface treatments as argon- or oxygen-plasma treatment and UV-ozone treatment are viable tools for engineering. I demonstrate that plasma treatment is a viable tool to modify the number of surface F-dopants in F:SnOs which is reflected in a tunable surface conductance. Furthermore, I explore the possibilities of UV-ozone treatment as an easy and virtually waste-free method to modify the number of surface oxygen vacancies in TiO2 thin films and discuss the impact on the conductance of these films. Lastly, I verify the significance of these methods on actual devices on the example of perovskite solar cells.

4.1 Defect engineering of FTO surfaces - adjusting the amount of surface fluorine doping with plasma treatment

Fluorine doped tindioxid substrates are used for a wide range of applications, spanning from solar cells and light-emitting diodes to touchscreens and liquid-crystal displays.[132]
Like many metal oxides, SnO_2 is an n-type semiconductor with a bandgap above 3.2 eV.[133] Its conductance depends on the doping concentration of fluorine ions that substitute an oxygen ion within the crystal. The conductance increases with increasing doping concentration. To the best of my knowledge, no one so far has compared the impact of different plasma treatments on the surface conductance of FTO substrates and its relevance for the device.

The choice of plasma treatment influences the surface properties

Argon plasma ions remove surface ions equally; oxygen plasma ions can also react with the surface and form metal oxide bonds.

The choice of gas critically influences how the respective plasma reacts with a metal oxide surface.

Argon is an inert noble gas that has one the highest ionization energies of 15.76 eV.[134] Although it is highly reactive when ionized within a plasma, Argon does not form stable chemical bonds to any surface. Therefore, Argon plasma can oxidize and remove any surface atom, when the power output of the plasma is set high. The higher the power output of the plasma cleaner is set, the higher the average kinetic energy of the plasma ions is. Since I used the plasma cleaner close to its maximal power output of 300 W (Plasmaprozessor 200-G TePla Technics Plasma GmbH, at 0.15 mbar and 290 W), the respective argon ions possess enough kinetic energy to remove tin-, oxygen and fluorine ions equally. Thus, the surface composition and the ratio of the different ions is equal to the bulk composition. This observation was first published by S. Y. Kim et al., who confirmed with XPS measurements, that neither nitrogen nor argon based plasma alters the surface chemistry with respect to its surface composition. [135]

The picture changes with oxygen as a carrier gas. Within an oxygen-plasma, several individual oxygen ions species can be found like O_2, O_2^-, O_2^+, O^+, O^- and O_3.[136–138] Oxygen readily forms chemical bonds with almost every other element. S. Y. Kim et al. observed the formation of a thin layer of metal oxide after oxygen plasma treatment of pure metal surfaces. [135139] This ambivalent behavior also occurs when treating metal oxide surfaces.

While oxygen plasma also removes surface tin-, oxygen, and fluorine ions equally, plasma oxygen ions still form chemical bonds with surface tin ions and thus bind to the surface.

Thus, surface oxygen vacancies of the tin dioxide crystal are filled with plasma oxygen ions. As a result, surface-bound fluorine dopants are gradually removed and partially substituted with surface oxygen ions (Figure 45).

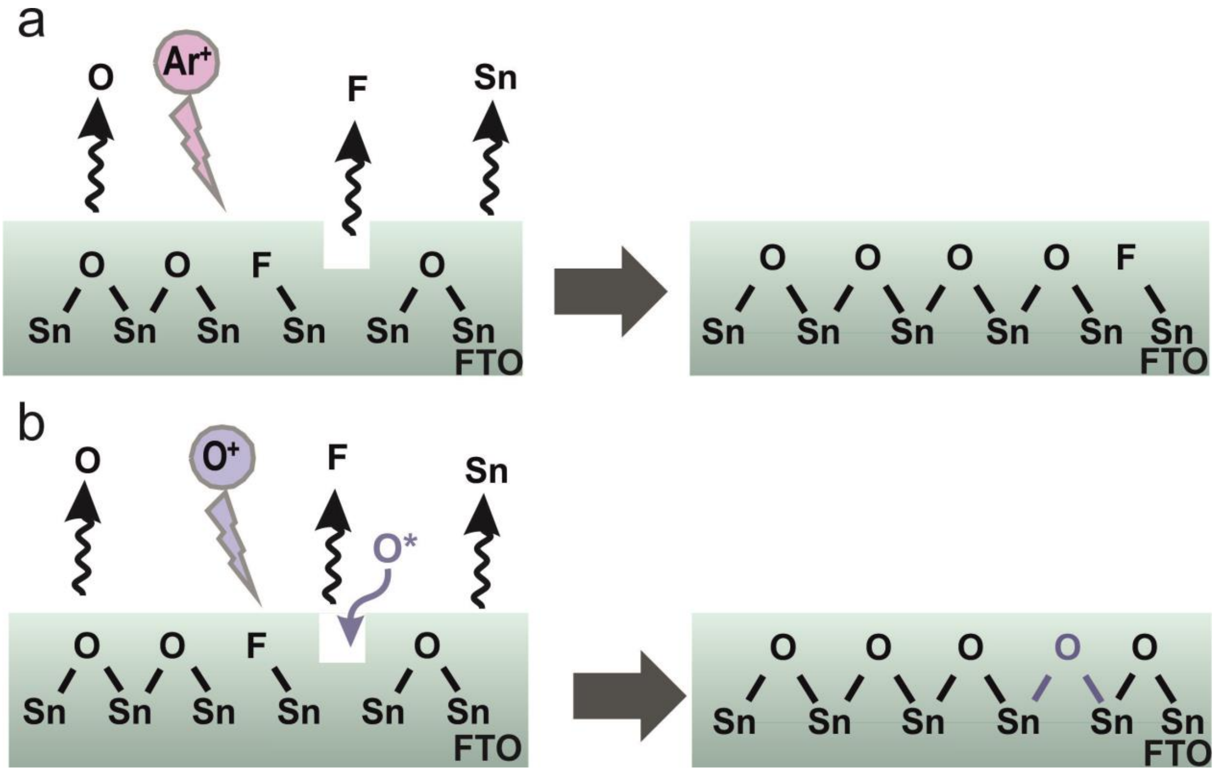

Figure 45: a) Argon plasma treatment on an FTO surface. b) Oxygen plasma treatment on an FTO surface.
Ar-Plasma treatment strips away surface ions equally and removes the first few atoms layers. The treated surface exhibits the same doping concentration as the bulk of the respective material. O-plasma also removes all surface ions at a high power output of the plasma cleaner. However, O ions can also react with the surface and form metal oxide bonds. Thus, surface fluorine dopants are statistically substituted with oxygen ions, which leads to the formation of a surface layer with a lower F-doping concentration.

Therefore, the treated surface exhibits a lower doping concentration compared to the bulk material. The power output of the plasma cleaner determines the main effect of the treatment. At a high power output, the removal of surface ions predominate. At a lower power output, the oxidizing effect predominates. H. Sun et al. recently published a very elegant approach using this phenomenon.[140] They demonstrated the formation of a thin layer of fully undoped SnO_2 after treating the surface of $F{:}SnO_2$ substrates for 15 min with an oxygen plasma. They used a power output of 150 W. Furthermore, they successfully employed this thin SnO_2 layer as an electron transport layer in PSC and achieved a power conversion efficiency of over 20 %.

XPS measurements on plasma-treated and untreated FTO substrates

XPS measurements confirm a tunable surface doping concentration via the choice of plasma treatment.

In order to demonstrate this effect, I compared the effect of argon-plasma treatment with oxygen-plasma treatment on FTO substrates. For that, I manually cleaned three individual commercial FTO substrates with an electric resistance of 10 Ohm/inch^2. Each substrate was cut from the same bigger substrate. One substrate was measured without any further treatment, one was subjected to 30 min of oxygen-plasma and one was subjected to 30 min of argon-plasma treatment. For each experiment, I used a power output between 290 – 300 eV. After 30 min of treatment, I expect that the surface fluorine doping concentration reaches an equilibrium that depends on the power output of the plasma cleaner and the bulk doping concentration.

I conducted a series of X-ray photoelectron spectroscopy in collaboration with Leon Prantl and Philipp Baumli. I plotted the intensity over the binding energy that corresponds to surface-bound fluorine dopants (Figure 46). The argon-treated sample had the highest surface fluorine doping concentration of (1.8 ± 0.3) %. For the oxygen-plasma treated sample, a surface fluorine doping concentration of (0.1 ± 0.1) % was recorded. The untreated sample showed no peak that would correspond to fluorine doping.

These measurements confirm that simple plasma treatment is suited in tailoring the surface doping concentration. As described above, argon plasma leads to the highest surface doping concentration. Since fluorine ions occur in the form of doping, their ratio compared with surface tin and oxygen was very low.

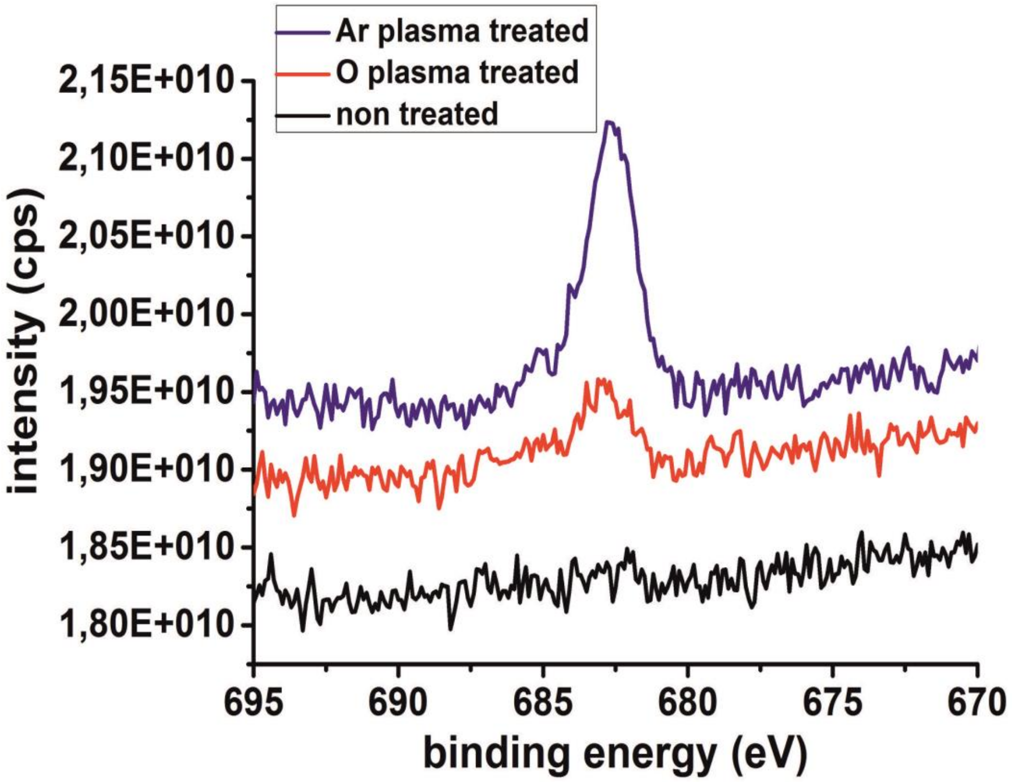

Figure 46: The influence of oxygen- and argon-plasma treatment on the surface doping concentration of F:SnO_2. F 1s orbital

. As expected, oxygen plasma treatment results in a lower doping concentration due to partial substitution of fluorine surface groups with oxygen plasma ions. The relative area under the F 1s peak was below 0.1 % and thus too small to be quantified. Otherwise, the choice of plasma treatment did not alter the ratio of tin to oxygen surface ions (Table 1). Since tin is already in the highest oxidation state of +4, an increase of surface oxygen ions due to further oxidation was not expected in any case.

Surprisingly the untreated FTO showed no measurable surface doping concentration (Figure 46). One reason for the lack of any F signal could be a thick contamination layer of hydrocarbons that mask any surface doping signal. Since the untreated substrate had only a 2% higher amount of surface carbon species compared to the plasma-treated samples, such masking is unlikely. In addition, the untreated substrates showed no significantly increased adhesion or reduced roughness that would indicate a several nanometer thick contamination layer (see below).

Table 1: The ratio of surface atoms of FTO surfaces is not significantly changed after oxygen- or argon-plasma treatment.

	C 1s [%]	O 1s [%]	Sn 2d5/2 [%]	F 1s [%]
Without treatment	24	49	27	0
With oxygen plasma treatment	22	50	28	0,1
With argon plasma treatment	22	49	27	1,8

Therefore, this low surface doping concentration is probably a result of production factors during manufacturing. A low surface fluorine concentration can be a consequence of either a high annealing step in an oxygen-containing atmosphere after the initial FTO deposition or a post-production cleaning step with oxygen-plasma. In any case, these results underline the importance of plasma treatment in order to achieve reproducible surfaces with the desired properties.

In summary, I demonstrated that the amount of surface fluorine doping is easily modified with the choice of plasma treatment. Argon plasma treatment removes all surface ions equally, which results in a surface doping concentration similar to the bulk doping concentration. Oxygen –plasma treatment substitutes surface fluorine ions, which leads to a gradual substitution of surface dopants with plasma oxygen ions. Thus, plasma treatment proofed to be an easy method for engineering surface defects of FTO substrates via changing the amount of surface fluorine doping. Compared to wet-chemical approaches, plasma treatment requires far fewer chemicals and produce far less waste. Since the doping concentration determines the conductance of a semiconductor, plasma treatment is also a viable tool in engineering the surface conductance of metal oxides. When a thin layer of undoped tin dioxide is desired, oxygen plasma treatment is an elegant tool to modify the surface fluorine doping content. H. Sun et al. recently demonstrated, that oxygen-plasma can be used to create a thin layer of undoped SnO_2 that was used as an electron transport layer for perovskite solar cells.[141] In effect, they did not need to synthesize an additional TiO_2 or SnO_2 thin film with printing or evaporation methods, which simplified the preparation of perovskite solar cells. Since the plasma approach skipped the otherwise required annealing step of the metal oxide film, their approach further renders the solar cell production cheaper and reduce the amount of waste.

cSFM measurements on plasma-treated and untreated FTO substrates

cSFM measurements confirm a tunable surface conductance via the choice of plasma treatment.

In order to study the impact of the surface doping modification on the surface conductance of the samples, I conducted a set of cSFM measurements. For that, I prepared three fresh 10 Ohm/inch² FTOs in a similar fashion as described above (see chapter 4.1). Every sample was manually cleaned and either directly measured or further plasma treated for 30 min and then directly measured. For each experiment, I used a power output between 290 – 300 eV and a gas pressure of 0.15 mbar.

The choice of post-cleaning treatment did not have a significant influence on the roughness of the substrate (Figure 47). For the untreated sample, a roughness of 33.4 nm was recorded. The oxygen-plasma treated sample had a roughness of 30.4 nm; the argon-plasma treated substrate had a roughness of 33.6 nm. All three samples showed similar average adhesion. The untreated sample had an average adhesion of 8.2 nN, the argon plasma cleaned sample had an average adhesion of 9.8 nN and the oxygen plasma cleaned sample had an adhesion of 9.2 nN. A major difference was observed in the measured median current. As expected, the untreated sample showed the lowest median current of 74 pA due to a surface F-doping concentration below the detection level. This thin interlayer of undoped SnO_2 has a low conductance and results in a low measured median current. With oxygen-plasma treatment, a median current of 800 pA was recorded, which is one order of magnitude bigger than the untreated median current. Again, this trend is reflected in the increased surface doping concentration after oxygen plasma treatment.

With argon-plasma treatment, a median current of 1719 pA was recorded, which is an additional increase of more than 100 % compared to the oxygen-plasma treated sample, reflecting the highest surface doping concentration. As S. Y. Kim et al. demonstrated, this difference in median current cannot be explained with a different amount of surface contamination since both plasma-treatments methods remove any organic contamination after 30 min. [135] S. Y. Kim et al. compared the effect of nitrogen, argon and oxygen plasma on thin metal films on glass. They observed, that every plasma removed organic compounds on the surface reliably after 15 min of treatment. [135]

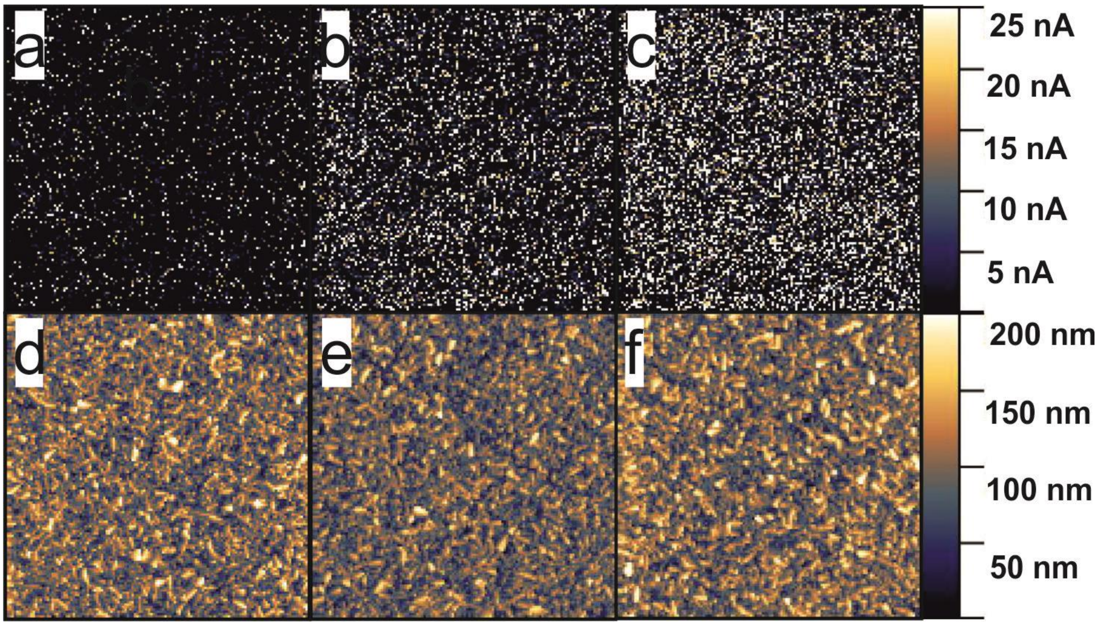

Figure 47: Current image of a) a hand-cleaned FTO without any further treatment, b) a hand-cleaned FTO with 30 min of oxygen plasma treatment and c) a hand cleaned FTO substrate with 30 min of Ar plasma treatment. Height image of d) a hand-cleaned FTO without any further treatment, e) a hand-cleaned FTO with 30 min of oxygen plasma treatment and f) a hand cleaned FTO substrate with 30 min of Ar plasma treatment. Each image was recorded with a peak force of 15 nN, a z-length of 150 nm, a pixel time of 8 ms and with an applied external bias of 1 V. Each image had a size of 10 x 10 µm with a resolution of 128 x 128 pixels.

Conclusion

Using XPS measurements, I demonstrated, that the choice of treatment method influences the amount of surface doping concentration. This surface defect engineering resulted in a tunable surface conductance through the interface layer of F:SnO_2., as cSFM measurements revealed. Argon-plasma treatment proved to be the best method for preparing high conducting FTO substrates, whereas oxygen-plasma is a viable tool for engineering the surface doping concentration. This high median current of 1719 pA can be attributed to the highest surface fluorine doping concentration after treatment since the argon plasma does not promote the substitution of surface fluorine ions. The lower measured median current of 800 pA for the oxygen plasma-treated substrate can be attributed to a decreased amount of fluorine dopant at the surface, which decreases the local conductance of the semiconductor F:SnO_2. The untreated FTO substrate showed the lowest median current of 74 pA which can be attributed to a low fluorine doping below the detection level.

Plasma treatment is a simple method, that allows modifying the conductance of semiconducting metal oxide as F:SnO_2 without any additional layer, wet-chemical reaction or high-temperature annealing. Thus, plasma treatment can be used to adjust the electric properties of metal oxides in existing applications at low cost and with low waste without the need of changing the synthesis of the respective layer or adding additional layers. Since organic LEDs use metal-oxides as MoO_3, it can be expected, that surface defect engineering can also play a vital role in these systems.

4.2 Defect engineering of TiO_2 surfaces - changing the amount of surface oxygen vacancies with UV-Ozone treatment or plasma treatment

Undoped TiO_2 is an n-type semiconductor with a low conductance.

Thin films of titanium dioxide (TiO_2) in anatase modification are applied in electronics ranging from thin-film transistors, anode materials for Lithium-ion batteries, memristors to photo-anodes for water oxidation.[142–146] For all these electronic devices a reproducible electrical resistance of TiO_2 plays a major role, particularly for the application of TiO_2 thin films as the electron transporting layers (ETL) in perovskite solar cells (PSC). For the application in perovskite solar cells, the TiO_2 films should have a high bulk electrical conductance, which enables fast and efficient charge collection rates from the perovskite photo-absorbing layer.[53,54] Since photon generated electrons have to travel through both the TiO_2 and FTO layer, a low overall conductance through both layers results in high series resistance. For solar cells, a high series resistance leads to a low fill factor and thus to low efficiency (see chapter 2). Therefore, a charge transport layer with a high conductance for the respective charge carrier is desired. Therefore, a high conductance trough TiO_2 thin films is desirable.[147] As F: $SnO2_2$, TiO_2 is an n-type semiconductor with a bandgap above 3 eV. However, unlike F:SnO_2 substrates, TiO_2 is not doped with foreign atoms as fluorine. As a result, the TiO_2 thin film possesses a far lower conductance compared to a pure F:SnO_2 surface (Figure 48).

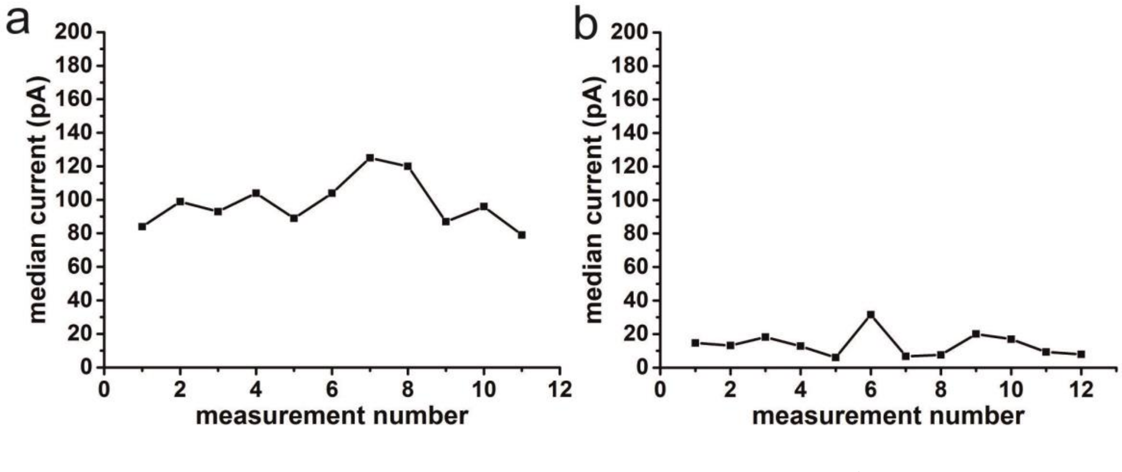

Figure 48: A contrasting juxtaposition of a set of Median currents of a) a single FTO substrate in different areas. b) 12 individual FTO substrates covered with a 30 nm thick layer of TiO_2. (see Chapter 3). TiO_2 thin films exhibit a far lower conductance than F:SnO_2

A standard route for increasing the conductance of a semiconductor is to increase the doping concentration. The most frequent defect within a TiO_2 crystal is oxygen vacancies. But in contrast to fluorine dopants in FTO, their impact on the electronic structure depends on their location within the crystal. Normally oxygen vacancies act as n-dopants in the TiO_2 lattice and thus increase the conductance.[38]

The effect of oxygen vacancies in TiO_2 depends on its location: bulk vacancies act as n-dopants, surface vacancies as electron traps.

However, oxygen surface vacancies act differently than vacancies within the bulk. Ye et al. claimed that oxygen vacancies act as electron traps at the interface and have a negative impact on the stability of PSC.[148] Mercado et al. used photoluminescence spectroscopy to study TiO_2 nanotubes and nanoparticles.[149] They found a broad green photoluminesce, which they associated with trapping of charge carriers at oxygen vacancies at surfaces. Moreover, they could show that this green luminescence disappears after filling these vacancies using a $TiCl_4$ treatment. Zhang et al. reported that surface oxygen vacancies can act as trap sites for electron-hole recombination.[150] Xing et al. studied the photoexcited charge carrier dynamics of $MAPbI_3$ in contact with different ETL and quartz. They found an increased photoluminescence lifetime on TiO_2 compared to [6,6]-phenyl-C_{61}-butyric acid methyl ester (PCBM) and quartz and concluded that TiO_2 exhibits surface states, which form dipoles with the surface states of the adjacent $MAPbI_3$ layer.[151] These dipoles act as an interfacial potential barrier, that leads to an electron accumulation within the $MAPbI_3$ layer and hinders the charge transport through the TiO_2 layer. Such potential barriers were recently confirmed by Kelvin Probe Force Microscopy for both TiO_2 and SnO_2.[17,152] The formation of dipoles at the interface of the perovskite with other transport layers have also been reported.[153]The results of the aforementioned studies suggest that oxygen vacancies at the surface of TiO_2 create surface states that are disadvantageous for charge transport through the interface.

In contrast, other research groups report a beneficial effect of oxygen surface vacancies on solar cell performance. The vacancies should create donor states just below the conduction band. Upon up-shifting the Fermi level, this should result in a better band alignment with the perovskite layer and an increase of the charge transfer to TiO_2.[154] In addition, Cojocaru et al. report an increased short-circuit photocurrent density and open-circuit voltage in PSC with increased surface oxygen vacancies.[155]

A majority of groups use TiO_2 directly after annealing, assuming that the freshly annealed surface is optimal for the fabrication of PSCs. [156–158] In essence, the role of surface oxygen vacancies is still controversial and requires further study. Strategies that primarily oxidize surfaces to study the influence of surface oxygen vacancies are needed.

UV-ozone treatment and plasma treatment of TiO_2 thin films

UV-ozone treatment decreases the concentration of surface oxygen vacancies of TiO_2 thin films. Argon plasma treatment increases the concentration of these defects.

We can identify two approaches to increase the conductance of TiO_2 thin films: I) increase of bulk vacancies and II) decrease of surface vacancies.
Bulk defects can only be created during the thin film synthesis via adjustment of the temperature and oxygen content within the atmosphere during annealing.[38] However, this approach would also affect the number of surface defects. A simpler and low-cost approach targets the adjustment of surface defects. UV-ozone treatment was used to change the concentration of surface oxygen vacancies in TiO_2 (Figure 49).[159] Several groups studied the influence of UV /UV-ozone treatments on TiO_2 and its effect on PSC efficiency.[156–158] Some possible explanations like an increased wettability originating from the UV-ozone treatment as the beneficial effect were presented. But to the best of my knowledge, I was the first to explore the effect on the local conductance, i.e. the current flow perpendicular to the TiO_2 film.[52]

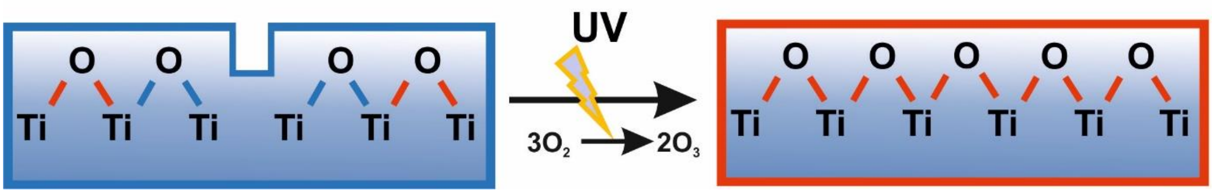

Figure 49: UV-ozone treatment of TiO_2 surfaces leads to a decreased amount of surface vacancies. Thus, simple UV-ozone treatment is an easy, low-cost clean way of engineering the surface defects of metal oxides. The red lines represent an oxygen-titanium bond where the respective titanium is saturated with oxygen ions. A blue line represents an oxygen-titanium bond where the respective titanium is also next to an oxygen vacancy. “Red” and “blue” type of bonding affect the energy of the O1s orbital differently and thus can be distinguished with x-ray photoelectron spectroscopy (Figure 51)

In other cases, a high concentration of surface defects is desired. TiO_2 surfaces have been used as a photocatalyst for various applications as water splitting for hydrogen production, sensors or oxidation of organic compounds.[160–162]

The number of surface oxygen vacancies can be increased via annealing at several hundred degrees Celsius under a nitrogen atmosphere, or radiation with a high energy electron beam.[38] However, these methods are energy-intensive and can affect underlying layers. Plasma-treatment of such a surface offers a less energy-intensive approach. M. A. A. Henderson et al. reported, that sputtering with noble gases also creates surface oxygen vacancies (Figure 50). [163]

As described above, argon plasma treatment is a simple and efficient method in stripping atoms from a metal oxide surface (see Chapter 4.1).

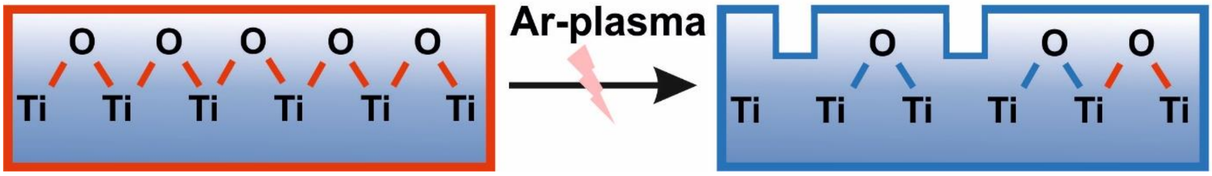

Figure 50: Argon-plasma treatment of TiO_2 surfaces leads to an increased number of surface vacancies. Thus, argon-plasma treatment is an easy, low-cost clean way of increasing the number of surface defects of metal oxides without altering the bulk properties. The red lines represent an oxygen-titanium bond where the respective titanium is saturated with oxygen ions. A blue line represents an oxygen-titanium bond where the respective titanium is also next to an oxygen vacancy.

Accordingly, the increase of surface oxygen vacancies leads to a decreased conductance through the TiO_2 thin film. Thus, the number of oxygen vacancies can either be increased or decreased with surface treatments, according to the desired properties.

XPS measurements on UV-ozone- treated and untreated TiO_2 thin films

XPS indicates that UV-ozone treatment decreases surface oxygen vacancies in TiO_2 thin films.

In order to demonstrate the easy surface defect engineering with UV-ozone treatment without changing the film thickness or roughness, I conducted a set of x-ray photoelectron spectroscopy experiments (XPS) in cooperation with and Gabriele Herrmann, who conducted with the measurement and Phillip Baumli, who was a great help in analyzing the data. XPS measurements were carried out with a Kratos Axis Ultra DLD (Kratos Ltd., Manchester, UK) using a monochromatic Al K_α X-ray source (1486.6 eV, emission current: 10 mA, anode voltage: 15 kV). The instrument base pressure remained below 1.1×10^{-9} Pa. The instrument work function was calibrated to a binding energy of 84.0 eV for metallic gold (Au $4f_{7/2}$). The charge neutralizer system was used for all measurements. The charge neutralization was monitored for adventitious carbon with the help of the C 1s peak. Survey spectra were recorded at a pass energy of 80 eV with 5 sweeps and an energy step of 1 eV. High-resolution spectra were obtained at a pass energy of 20 eV and 10 sweeps for an energy step of 0.1 eV. The analysis area was $\approx 300 \times 700\ \mu m^2$. All spectra were recorded in the spectroscopy, hybrid lens mode. For each sample, at least three independent measurements were performed.

Curve synthesis and deconvolution, *i.e.* identifying the components of the XP signals, was performed by fitting the XP signal with Gaussian/Lorentzian curves. The peak positions for individual components were compared to literature values with the help of the commercial software CasaXPS (version 2.3.16, Casa Software Ltd, Chichester, UK). We assumed that only slight deviations from the ideally expected stoichiometric composition of the surface from

TiO_2 are present (O:Ti = 2:1). For the XPS analysis, we used a TiO_2 film thickness of 60 nm, and the surface roughness determined by the underlying FTO substrate remained below 10 nm. The binding energies were calibrated using the C 1s peak for adventitious carbon at a binding energy of 284.8 eV, with an associated error of $\pm$ 0.1 – 0.2 eV.[164] No argon ion sputter cleaning has been performed prior to measurement.

O1s XPS comparison

We performed XPS analysis on samples prepared according to three different procedures: 1. Freshly prepared samples which were directly transferred to the vacuum pre-chamber of the XPS instrument, *i.e. freshly annealed* sample. 2. freshly prepared samples which were directly subjected to UV-ozone treatment and then transferred immediately to the XPS instrument, *i.e.* UV-ozone sample. 3. Samples which had been prepared 24 h earlier without UV-ozone treatment and have been subsequently exposed to the ambient atmosphere for 24 h, *i.e.* annealed sample after 24 h.

The O 1s signals are known to be affected by oxygen treatment.[158] [154] [159] The O 1s signals contain three contributions (Table 4). (i) A signal at 530.0 eV corresponds to oxygen that is bound to coordinatively saturated titanium atoms (Figure 51, red curve). (ii) At an energy of 531.1 eV, the signal is caused by oxygen that is bound to partly unsaturated titanium atoms. This signal corresponds to the number of oxygen vacancies (Figure 51, blue curve). (iii) A signal at 532.2 eV originates from oxygen in –OH groups and adsorbed CO_2 (Figure 51, green curve).[154]

For the annealed sample, the most intense contribution to the O 1s signal originates from oxygen that is bound to coordinatively saturated titanium atoms (Fig. 4a); we calculated a relative peak area of ~77 % for (i). The signal corresponding to oxygen that is bound to partly unsaturated titanium atoms covers a peak area of ~15 % (ii). The O 1s signal from –OH groups and adsorbed CO_2 corresponds to a peak area ~8 % (iii).

For the annealed and UV-ozone treated sample we calculated relative peak areas of 82% at 530.1 eV (i), ~9% at 530.9 eV (ii) and 9 % at 532.0 eV (iii). The change in relative peak area reflects a change in stoichiometry: The amount of oxygen bound to partly unsaturated titanium atoms in the lattice decreases. This decrease means that the number of surface oxygen vacancies at the surface decreases.

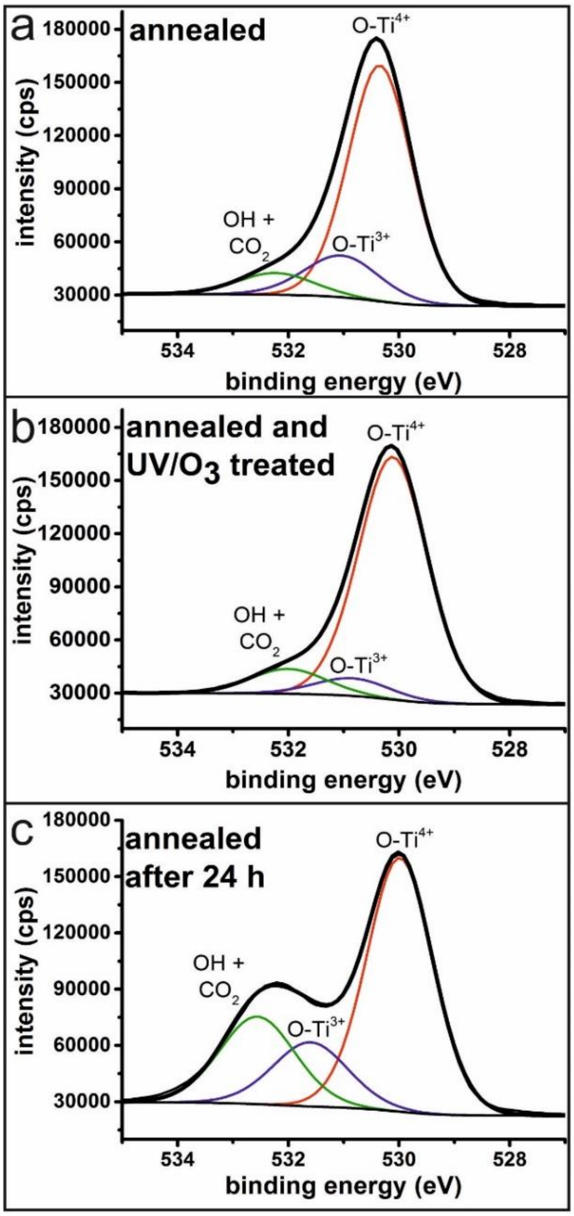

Figure 51: The effect of UV ozone treatment on the number of surface oxygen vacancies. The measured signals (black curves) were fitted with three Gaussian/Lorentzian curves. The red curves correspond to oxygen bound to coordinatively saturated titanium atoms. The blue curves correspond to oxygen that is bound to partly unsaturated titanium atoms. The green curves correspond to oxygen in –OH groups and adsorbed CO_2. a) annealed sample, b) annealed and UV-ozone treated, c) annealed after 24 h

For the freshly annealed samples, we calculated the following energies: (I) 530.0 eV, (II) 531.1 eV and 532.2 eV. For the annealed and UV-ozone treated sample, peak maxima were calculated at (I) 530.1 eV, (II) 530.9 eV and (III) 532.0 eV. For the annealed samples, that were kept in ambient for 24 h we calculated the following energies:(I) 530.1 eV, (II) 531.6 eV and 532.2 eV.

Table 4: Influence of UV-ozone treatment or storage at ambient conditions on O 1s signals.[4]

	O bound to saturated Ti (I)	O bound to unsaturated Ti (II)	-OH and CO_2 groups (III)
Annealed	77 %	15 %	8 %
Annealed and UV-ozone treated	82 %	9 %	9 %
Annealed after 24 h	59 %	15 %	26 %

For the annealed sample that was kept 24 h in ambient conditions, we calculated relative peak areas of ~ 59% at 530.1 eV (i), ~15% at 531.6 eV (ii) and 26% at 532.2 eV (iii). Compared to the annealed sample and the UV-ozone sample the contribution of oxygen that is bound to coordinatively saturated titanium atoms (i) is reduced considerably. A significantly increased amount of surface-bound -OH and CO_2 oxygen groups are found compared to both freshly annealed samples. We interpret this as an indication not only for the adsorption of water and carbon dioxide but also as a general indication for the presence of adsorbed species on the TiO_2 surface, showing the recontamination after being stored at ambient conditions after one day. The relative intensity of the contribution originating from oxygen that is bound to partly unsaturated titanium atoms (ii) remains unchanged compared to the annealed sample. The O 1s signal that corresponds to oxygen that is bound to partly unsaturated titanium atoms (i) is slightly shifted to a higher binding energy. It has been shown, that carbon species adsorb more strongly on partly reduced TiO_2 surfaces, which corresponds to more oxygen vacancies.[165]

Thus, we argue that the shift reflects surface oxygen vacancies acting as reactive centers, which react preferably with hydrocarbons and thereby changing the chemical environment locally.

C1s XPS comparison

We measured the XP C1s signals for a freshly annealed, a freshly annealed and UV-ozone treated and an annealed sample after 24 h (Figure 52). The signal at the C1s binding energy did not show significant changes of peak position nor peak shape for samples which were freshly annealed and freshly annealed and UV-ozone treated. This similarity indicates, that the nature of adsorbed carbon species is not altered significantly. However, both peak shape

---

and position changed strongly for an annealed sample, that was stored at ambient for 24 h. These changes reflect the adsorption of various carbon species on the TiO_2 surface.

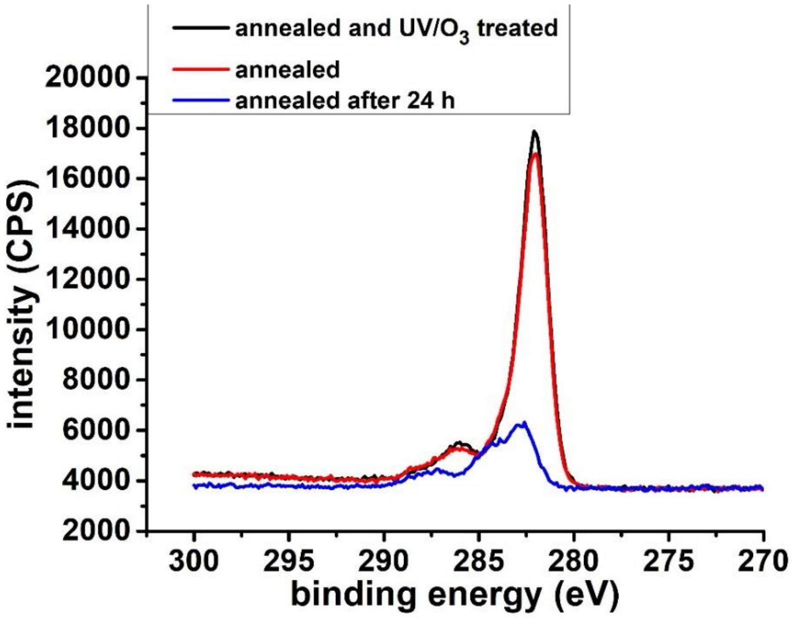

Figure 52: Comparison of the different XP spectra of a freshly annealed, a freshly annealed and UV-ozone treated and an annealed sample after 24 h.

Conclusion

The XPS results indicate that UV-ozone treatment reduces the number of surface oxygen vacancies. Moreover, significant changes in the nature of adsorbed carbon species did not occur after UV-ozone treatment on freshly annealed TiO_2 films.

Therefore, UV-ozone treatment is an efficient and easy tool in altering the surface defect concentration of semiconducting metal oxide layers and could be used for solar cells, light-emitting devices, and catalysts.

In addition, the XPS C1 peaks indicate strong changes in the surface carbon content after 24 h. This observation underlines the necessity of only using freshly prepared and annealed TiO_2 films for solar cells since it can be expected that the adsorped carbon species critically influence the properties of the TiO_2 interface. Further research has to be conducted to investigate, whether such carbon contamination can be removed with simple UV-ozone treatment.

cSFM measurements on UV-ozone- treated and untreated TiO_2 thin films on FTO substrates

UV-ozone treatment increases the local conductance of TiO_2 thin films on FTO.

In order to demonstrate the key role of the surface oxygen vacancies on the surface conductance of TiO_2 thin films, I compared treated and untreated films with cSFM measurements. For that, I synthesized two TiO_2 films on freshly cleaned and argon-plasma cleaned FTOs. I performed cSFM on 60 nm thick TiO_2 films made from 1 M $TiCl_4$ solution. The spin-coated and annealed TiO_2 film showed a maximum current of 7.3 nA at a bias voltage of 1 V over an area of 10×10 μm^2 (Figure 53 a). The surface of this film contains grains with diameters of 10 - 20 nm and has a root mean square (RMS) roughness of 6.9 nm (Figure 53 c). This RMS-roughness is lower than the roughness of the underlying FTO (RMS of 17.1 nm). After treating the second film for 30 min with UV-ozone, I measured a strong increase of the local conductance. Locally, the maximum measurable current even exceeded our maximum detection limit of 120 nA (Figure 53 c).

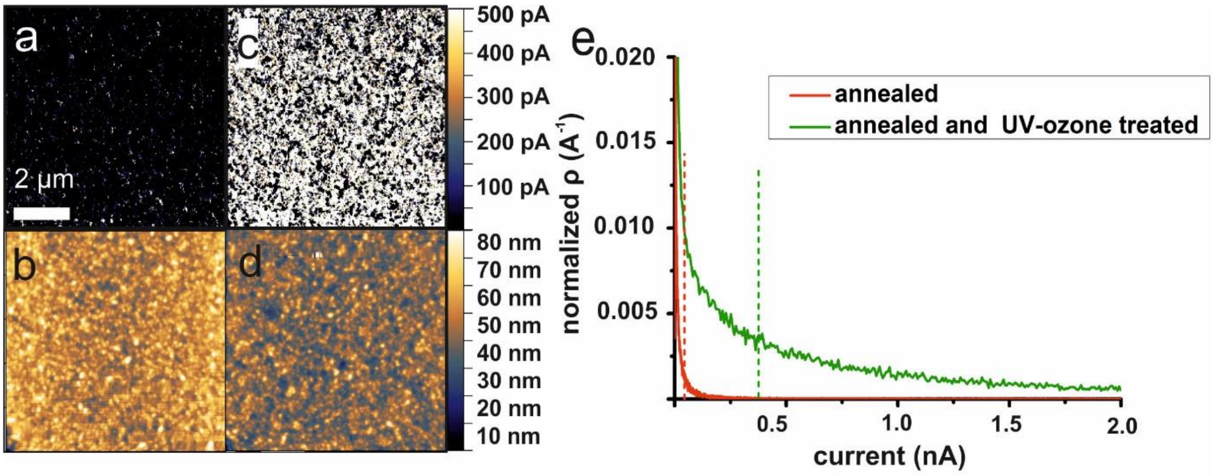

Figure 53: a) Current image and b) height image of cSFM measurement on TiO_2 thin film without UV-ozone treatment. c) Current and height image d) after 30 min of UV-ozone treatment. In order to visualize local current differences more clearly, I set the current scale to a value of 500 pA. e) Current distributions before (red data points) and after 30 min UV-ozone treatment (green data points).

In order to visualize and compare the local conductance of UV ozone treated and pristine TiO_2 films, I set the current scale to 0 - 500 pA (Figure 53 a and c). For the untreated surface I obtained < 0.1 % pixels with a current > 500 pA. For the treated surface I obtained 45.8 % pixels with a current > 500 pA. Furthermore, the conductance is distributed more homogeneously over the surface compared to the untreated film. To compare the changes in conductance after treatment, I calculated the normalized current distribution (ρ) by dividing each value by the sum (Figure 53 e). Then, I calculated the median value. For the untreated sample, the median value was 4.6 pA (red dashed lines in Figure 53 e) and for the UV-ozone treated sample, the median was 378 pA (green dashed lines in Figure 53 e). Therefore, the median increased roughly by two orders of magnitude after UV-ozone treatment.

A treatment time of 30 min guarantees a reproducible increase.

In order to determine the minimal needed treatment time for a reproducible increase of median current, I repeated the comparison of untreated and treated films several times with different samples prepared in an identical manner. I conducted three sets of measurements at different weeks, i.e. three different samples that were exposed subsequently to UV-ozone for 1, 5, 10, 15 and 30 min. For each measurement, a new sample was prepared directly in advance to the UV-ozone treatment. The cSFM measurements were performed directly after treatment and for each test series. I always used the same tip for each test series. Test series 1 showed a median current increased from 4.6 pA without UV-ozone treatment to 378 pA after 30 min of UV/ozone treatment. For the second and third sets, the median current increased from 1.6 pA and 2.2 pA to 101.6 pA and 92.6 pA, respectively. The difference in absolute values between two sets of measurements can be attributed to variations in the tip geometry and Pt/Ir coating of the individual cantilevers.

A larger contact area of the cantilever tip leads to better electric contact and thus to an overall increased local current. Despite absolute differences between two sets of measurements, I found an increase by two orders of magnitude in the median value of the conductance distribution after UV-ozone treatment for all cases (Figure 54a).

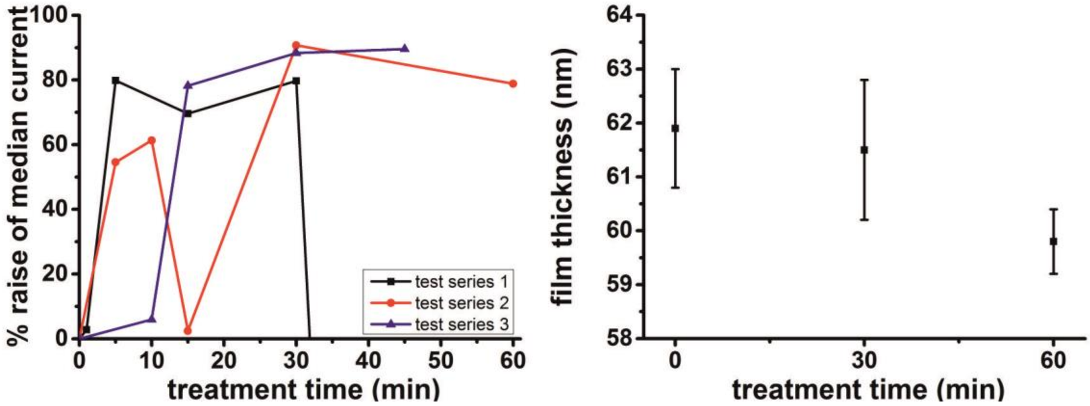

Figure 54: A) Influence of treatment time on the median current. B) Influence of treatment time on TiO2 anatase film thickness.

In order to find the minimal needed treatment time, I plotted the percentage increase of the median current with respect to the previous measurement. After 30 min, every set showed the same increase of median current. I found a varying development of median current with advancing treatment time between 0 and 15 min. This variation in conductance through just one layer demonstrates the issue of reproducibility for perovskite solar cells. Since the TiO_2 layer must be spin-coated and annealed in the air from aqueous $TiCl_4$ solution, this synthesis is prone to changes in the ambient conditions within the lab. Humidity and temperature play a crucial role in the initial film formation during spin-coating and its further crystallization. Thus, a slightly different crystallization leads to slightly different surface properties and thus different electronic properties of the resulting TiO_2.

A treatment time below 30 min is not sufficient in counteracting these differences which leads to inconsistent film quality and local conductance. Therefore I conclude that 30 min of UV-ozone treatment is the minimum time needed to achieve a reproducible increase of current and counteract potential variations between two different batches of TiO_2. Since the local conductance depends on the film thickness, I investigated the possibility of changes during the treatment.

Without treatment, I measured a film thickness of 61.8 ± 1.1 nm and 61.5 ± 1.2 nm after 30 min of UV-ozone treatment (See Figure 54 b). Thus, I excluded a reduction in TiO_2 film thickness.

In conclusion, a simple UV-ozone treatment can increase the conductance reproducible through the TiO_2 film without altering film thickness. These cSFM measurements demonstrate, that the conductance of thin films not only depends on the layer thickness but also on the surface properties. A treatment time of under 30 min. show variations in the extend of the surface modification. The differences in surface modification for different days underline the impact of ambient conditions on the properties of thin-film applications as semiconducting metal oxide films. Differences in the ambient conditions e.g. temperature, ambient light intensity and most important humidity do not only occur in different laboratories but also in different seasons and even days. However, since all TiO_2 thin films exhibited the same trend after a treatment time of 30 min, I conclude that UV-ozone treatment can compensate for the effect of different ambient conditions and create a reproducible surface independent of location and season.

Diode characteristics of treated and untreated TiO_2 thin films

UV-ozone treatment does not change the diode characteristic of TiO_2 thin films.

In order to rule out possible local short circuits or other effects such as the generation of local failure of electron transport or hole blocking behavior, I compared the I-V characteristics of two freshly annealed TiO_2 thin films on FTO: one was UV-ozone treated, the other was measured without any further treatment. (Figure 55).

For that, I measured consecutive cSFM on two substrates with varying external bias. Both substrates were manually cleaned, oxygen plasma treated and coated with an approximately 30 nm thick TiO_2 layer as described in Chapter 3. One substrate was subjected to 30 min of UV-ozone treatment directly after annealing the TiO_2 layer. The other sample was measured directly after annealing without any further treatment. I plotted the measured median current against the applied bias to generate an I-V-curve. The SFM-tip has a Pt/Ir-metal coating with a work function of ~3.9 eV.[113] The semiconducting anatase form of TiO_2 has a work function of 5.1 eV.[39] Therefore, I expect a Schottky-diode-characteristic IV behavior with a current onset at around 1.2 V. My measurements revealed a reproducible diode behavior for both forward and backward scan. A current below the noise level of my cSFM of

1.5 pA was measured at an external bias below 0.75 V. Thus, I preserve the diode properties of the TiO_2 layer during UV-ozone treatment.

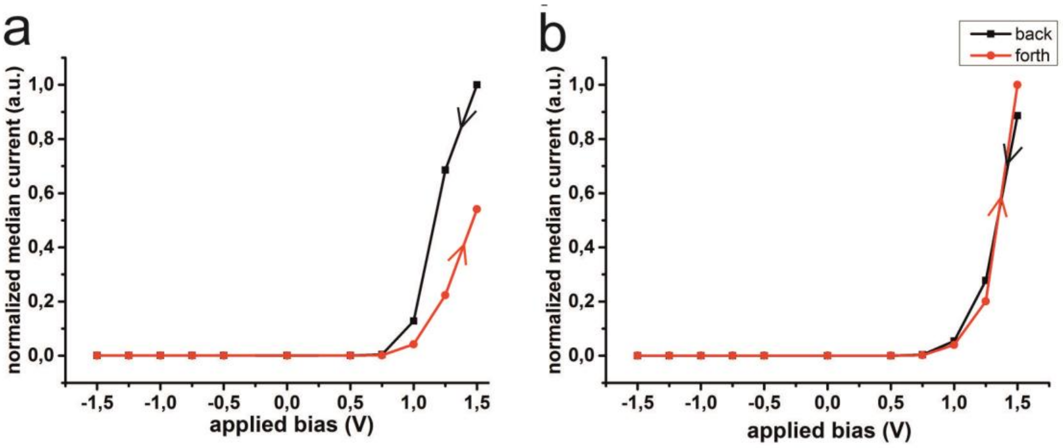

Figure 55: a) Normalized local I-V-curves of an annealed TiO_2 film and b) an annealed and UV-ozone treated TiO_2 film on FTO. Measurements were conducted starting at an initial bias of +1.5 V, which was increased stepwise to 0 V and then inverted up to -1.5 V (black curve). Subsequently, the bias was reduced stepwise again to 0 V and inverted up to 1.5 V (red curve). Please note that for every image a new area of 256x256 pixels was measured to avoid any potential influence of previous measurements. This set of measurements took approximately 1 h.

For both the treated and untreated sample, no current above the noise level of 1.5 pA could be measured with applied bias below 0.75 V. Therefore, the UV-ozone treatment did not affect the threshold voltage. I noticed a decrease of median current for the untreated sample comparing the back and forward scan (see Figure 55: a) Normalized local I-V-curves of an annealed TiO2 film and b) an annealed and UV-ozone treated TiO2 film on FTO. Measurements were conducted starting at an initial bias of +1.5 V, which was increased stepwise to 0 V and then inverted up to -1.5 V (black curve). Subsequently, the bias was reduced stepwise again to 0 V and inverted up to 1.5 V (red curve). Please note that for every image a new area of 256x256 pixels was measured to avoid any potential influence of previous measurements. This set of measurements took approximately 1 h. Figure 55a, red curve compared to the black curve). The cause of this difference is discussed in *Chapter 3.*

In conclusion, UV-ozone treatment does not alter the semiconducting properties of metal oxides. Therefore, the hole-blocking properties still occur after UV-ozone treatment of TiO_2 thin films. Accordingly, UV-ozone treatment is a mild method for changing the conductance and surface defect density of metal oxides.

Terahertz measurements of treated and untreated TiO_2 thin films

For terahertz spectroscopy, an electron is promoted from the valence band to the conduction band with a UV-pump-layer. The absorption of a Terahertzlaser probes the bulk electron impedance.

In order to show, that the beneficial effect of UV-ozone treatment is solely due to a surface effect we conducted Terahertz experiments to measure changes in the bulk conductance of TiO_2 films on fused silica (Figure 56).

We studied the influence of UV-ozone treatment on the bulk conductance of TiO_2 films by THz spectroscopy in cooperation with Qu Sheng who conducted the measurement and helped with the analysis. This optical pump THz probe setup was driven by an amplified laser system (Solstice ACE by Spectra-Physics). It can produce ultrashort laser pulses of center wavelength 800 nm and a pulse duration of ~35 fs at a repetition rate of 1 kHz. For the pump beam of this setup, an optical parametric amplifier (TOPAS-Prime and NirUVis by Light Conversion) was used to generate 310 nm pump beam. For the terahertz generation and detection, 10% of the incoming laser beam was used (90 mW). THz radiation was generated in a phase-matched manner by optical rectification on a ZnTe crystal (<110> orientation, 10 mm × 10 mm × 1 mm thickness, purchased from MaTeck). The ZnTe generation crystal was pumped with an 800nm beam. The THz light exits the ZnTe generation crystal slightly divergent and is first collimated and subsequently focused on the sample using a pair of off-axis parabolic mirrors.

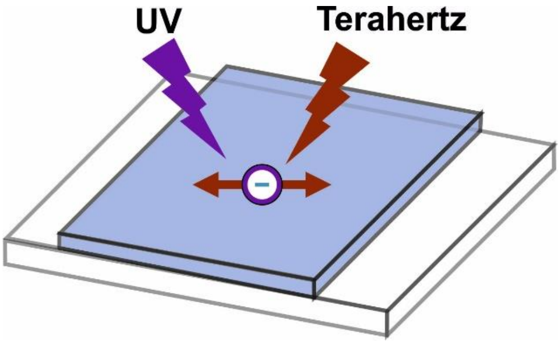

Figure 56: Working principle of a terahertz measurement of bulk conductance of TiO_2 thin films. An UV-pump laser generates a photoexcited electron. A second laser in the terahertz spectrum probes the mobility of such an electron within the bulk. The higher the absorption of the terahertz laser is, the higher the impedance of the electron within the bulk. The impedance can be used to calculate the optical conductance.

After the sample, the transmitted THz pulses are re-collimated and focused onto a second ZnTe detection crystal by another pair of parabolic mirrors, where the instantaneous THz field caused a birefringence that can be detected through electro-optical sampling.[166] In this electro-optical sampling, 800 nm laser pulses (<1 mW) with linear polarization were used as a sampling beam. All samples were all measured in a nitrogen atmosphere.

Terahertz analysis confirms, that UV-ozone treatment mainly affects the surface conductance.

Experimentally, we measured the THz field *E* in the time domain that was transmitted through the non-excited sample and the photoinduced change *ΔE* from the excited sample. The optical conductance $\Delta\sigma$ can be calculated by

$$\Delta\sigma = \frac{(n+1)}{Z_0 l}\frac{\Delta E}{E} \tag{1}$$

where *n*, $Z_{0,}$ and *l* are the refractive index of fused silica (n=1.95), the impedance of free space (Z_0 =377 Ω) and the thickness of the samples (for this experiment 250 nm), respectively~~.~~ For the sample that was only annealed we measured an optical conductance of ~51 S/m after a pump-probe delay of 1 ps. The additional UV-ozone cleaning led to a slight decrease of conductance to ~46 S/m (Figure 57). This decrease corresponds to a slight reduction in the number of n-dopants in the TiO_2 bulk material.

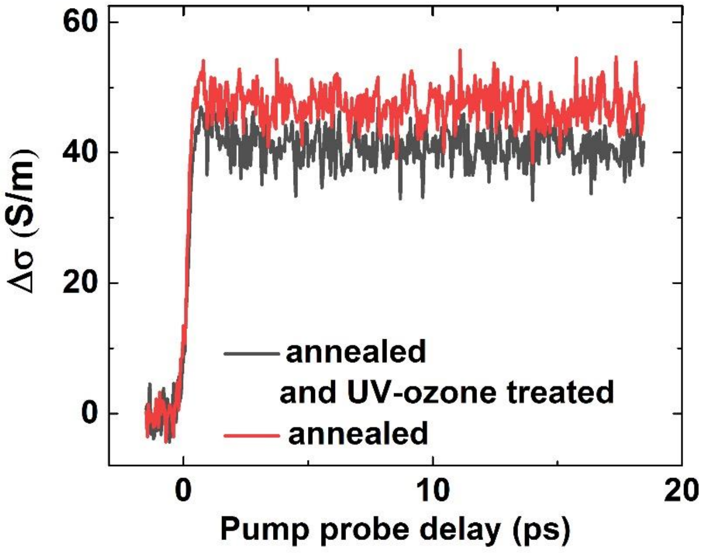

Figure 57: Influence of UV-ozone treatment on optical conductance.

In conclusion, I demonstrated that the location of an oxygen vacancy is crucial for its influence on the conductance of TiO_2 with Terahertz spectroscopy. In bulk, the non-stoichiometry leads to an n-type conductivity. However, at the interface of a TiO_2 film the oxygen vacancy act as an electron trap, that decreases the conductance. Secondly, my results suggest, that for TiO_2 film films, bulk conductance is not the dominating factor for the measured conductance. The slight decrease in bulk conductance is overcompensated by the beneficial effect of removing the surface oxygen vacancies. These findings underline the importance of interface control for thin-film applications as solar cells.

cSFM measurements on UV-ozone- treated TiO_2 thin films with additional argon-plasma treatment

An additional argon-plasma treatment on UV-ozone treated TiO_2 thin films results in an increased amount of surface oxygen vacancies and thus a low surface conductance.

As argued above, a high surface concentration of oxygen vacancies is desired for many applications. I found, that simple argon-plasma treatment is not only suited to alter the surface defect concentration of fluorine-doped tin oxide, but it is also a viable tool to increase the number of surface oxygen vacancies of TiO_2 thin films. B. Bharti et al. reported, that air plasma treatment also increases the concentration of surface oxygen vacancies in Fe and Co-doped TiO_2.[131] They found a redshift of the absorption of Fe doped TiO_2 films and a blue shift for Co-doped films after plasma treatment.

In order to demonstrate the effect on the surface conductance, I synthesized two 30 nm thick TiO_2 films on –argon plasma treated FTO substrates (Figure 58). Both films were subjected to 30 min of UV-ozone treatment. The first film was immediately measured after treatment. The second film was subjected to an additional 30 min of argon plasma treatment.

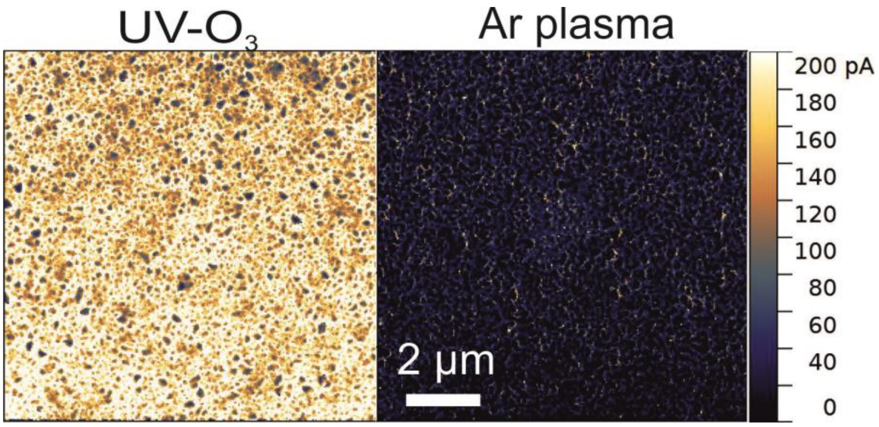

Figure 58: Influence of argon-plasma treatment on the local conductance of TiO_2 thin films on FTO. Argon-plasma treatment increases the number of surface oxygen vacancies and thus increase the number of surface electron traps. Accordingly, the argon-plasma treated sample exhibited the lowest median current. Each image was recorded with a peak force of 15 nN, a z-length of 100 nm, a pixel time of 20 ms and an externally applied bias of 2 V. each image had a size of 10 x 10 µm with a resolution of 256 x 256 pixels.

The TiO_2 thin film, that was subjected to just UV-ozone treatment showed a median current of 166 pA. With Ar-plasma treatment, the median current dropped to 15.86 pA. This decrease in median current was not reflected in a change in roughness or in a change in adhesion. Therefore, argon plasma is a viable tool for engineering the surface defects of

TiO_2. A treatment of 30 min increased the concentration of surface oxygen vacancies which leads to a decrease of surface conductance.

In conclusion, plasma treatment is a versatile tool for defect engineering the tool of semiconducting metal oxides. Argon-plasma treatment can be used to increase the surface defect density and therefore the number of catalytic sites of metal oxides like TiO_2. Moreover, this approach could be used for applications where trapping of charges and recombination is desired, as in light-emitting devices.

Influence of the UV-ozone treatment on solar cell efficiency

Increased surface conductance of TiO_2 thin films leads to a decreased series resistance and thus an increased fill factor for perovskite solar cells.

I demonstrated that compact TiO_2 thin films exhibit an increased local conductance after 30 min of UV-ozone treatment (see chapter 4.1). Surface oxygen vacancies create electron trap states that hinder the migration of electrons through the TiO_2 layer. This increase in the perpendicular conductance of compact TiO_2 thin films by the UV-ozone treatment is expected to affect the *PCE* of perovskite solar cells.

Table 1: Parameters of treated and untreated perovskite solar cells with compact TiO_2 layers as ETLs[a]

	Device	J_{sc} [mA/cm²]	V_{oc} [mV]	FF [%]	PCE [%]
annealed and UVO treated	Backward scan	(21.9±1.5)	(1061±42)	(68.2±4.0)	(15.9±1.9)
	champion	23.0	1098	75.8	19.1
annealed	Backward scan	(20.5±3.1)	(1052±58)	(63.8±8.3)	(13.8±3.1)
	champion	23.2	1088	73.4	18.5

Displayed are the mean value of the short-circuit current *Jsc*, the open-circuit voltage *Voc*, the fill factor *FF* and the power conversion efficiency *PCE*.

In order to verify the relevance for PSC, I fabricated 61 planar perovskite-based solar cells without a mesoporous TiO_2 layer.[52] Half of these cells were made with TiO_2 that was exposed for 30 min to UV-ozone. For the other half, we used TiO_2 films directly after the annealing step, a typical protocol for many of today's standard processes.[94] For all cells, we measured the short circuit current density J_{sc}, the open circuit potential V_{OC}, and the fill factor (*FF*), and we calculated the *PCE*.

Cells made with the freshly annealed TiO_2 without UV-ozone treatment showed an average J_{sc} of (20.5 ± 3.1) mA/cm² (Table 1). The cells with UV-ozone treated TiO_2 layers showed an average J_{sc} of (21.9 ± 1.5) mA/cm². Thus, the increased local conductance through the TiO_2 film led to an increased J_{sc} by approx. 10 %. We explain the increase in J_{sc} with an increasing collection probability of charge carriers into the TiO_2 layer upon removing surface traps. In addition, the standard deviation of the J_{sc} decreased, which hints to a more uniform and reproducible preparation process. The open circuit voltage changed only slightly (Table 1). We also measured an increase in the *FF* from 63.8 ± 8.3 to 68.2 ± 4.0 for the UV-ozone treated cells. We attribute the latter to a decreased internal serial resistance through the layers. The higher J_{sc} and *FF* for the UV-ozone treated cells resulted in an increase in average *PCE* from 13.8 ± 3.1 % to 15.9 ± 1.9 % (Figure 59). With UV-ozone treatment we fabricated a champion cell with an efficiency of 19.1 %. Without UV-ozone treatment, the champion cell had an efficiency of 18.5 %.

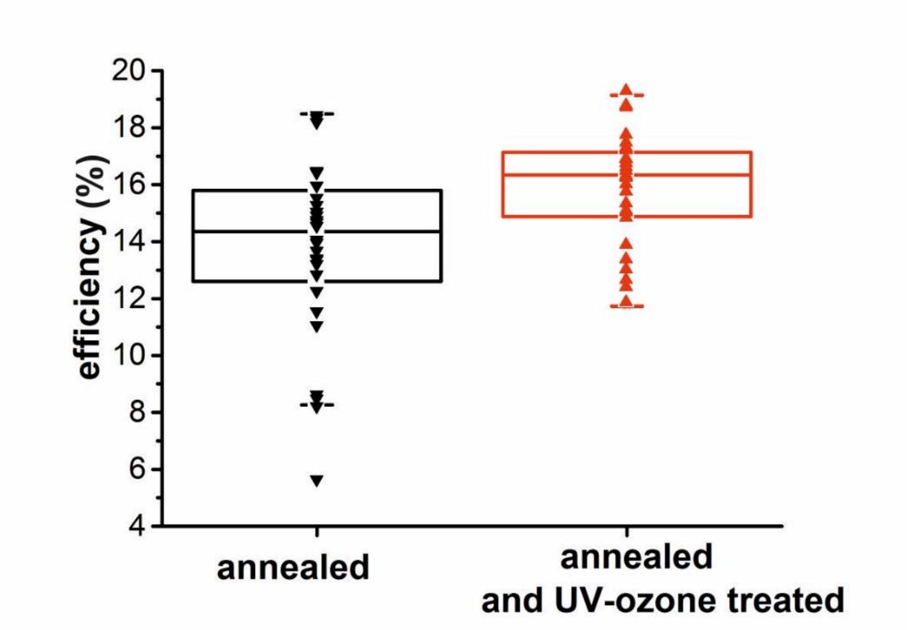

Figure 59: Distribution of cell efficiency without UV-ozone and with UV-ozone treatment for planar perovskite solar cells.

UV-ozone treatment also has a beneficial effect on mesoporous TiO_2 ETLs (Table 2) and other metal oxide-based ETLs such as SnO_2 (Table 3). For mesoporous TiO_2 films, we measured an increase of 1.2 percentage points in the average *PCE* after UV-ozone treatment with a record cell efficiency of 19.5 %. These *PCE* represents the state-of-the-art for single halide single cation perovskite solar cells, i.e. $MAPbI_3$ on mesoporous TiO_2.[167] For a compact SnO_2 ETL, UV-ozone treatment improved the average *PCE* by 1.6 % (absolute). Thus the UV-ozone treatment can also be applied to other metal-oxide based ETL.

Table 2: Parameters of treated and untreated perovskite solar cells with compact and mesoporous TiO_2 layers as ETLs.

	Device	J_{sc} [mA/cm²]	V_{oc} [mV]	FF [%]	PCE [%]
annealed and UVO treated	mean value	(23.7±0.6)	(1059±3)	(75.4±0.7)	(18.9±0.4)
	champion	24.7	1054.2	74.9	19.5
annealed	mean value	(23.6±0.5)	(1060±9)	(70.7±5.9)	(17.7±1.4)
	champion	23.9	1050.2	74.5	18.7

Table 3: Parameters of treated and untreated perovskite solar cells with compact SnO_2 layers as ETLs

	Device	J_{sc} [mA/cm²]	V_{oc} [mV]	FF [%]	PCE [%]
annealed and UVO treated	mean value	(21.2±0.3)	(1068±4)	(73.5±1.1)	(16.6±0.4)
	champion	21.2	1070	75.1	17.0
annealed	mean value	(20.4±1.8)	(1059±10)	(69.2±2.4)	(15.0±1.6)
	champion	21.9	1071	71.9	16.9

Conclusion Defect engineering with Plasma treatment and UV-ozone treatment.

Surface defects critically influence the properties of semiconducting metal oxides. Especially in thin-film applications, surface properties dominate the chemical and electrical characteristics of these materials. I demonstrated, that simple plasma treatment and UV-ozone treatment is a versatile tool in modifying the surface defects of different metal oxides.

Using XPS measurements, I demonstrated a tunable surface Fluorine-doping concentration of FTO substrates, depending on the choice of plasma treatment. The tunable surface doping concentration was reflected in a tunable surface conductance, as I verified with cSFM measurements. However, neither the topology nor the adhesion changed after 30 min of plasma treatment, which indicates, that all modifications only occur at the first few layers of atoms at the surface.

Oxygen vacancies play a key role in TiO_2 thin films, depending on their location within the crystal. Oxygen vacancies within the bulk act as n-dopants that increase the conductance through the n-type semiconductor TiO_2. In contrast, surface oxygen vacancies act as electron traps that hinder the charge transport through the thin film and thus decrease the conductance. I demonstrated, that 30 min of UV-ozone treatment reduces the concentration of surface defects, as indicated by XPS measurements. Using cSFM, I verified, that this decrease of surface defects was reflected in an increase of surface conductance. Terahertz measurements verified, that UV ozone treatment causes only a negligible decrease in bulk conductance. This decrease is overcompensated by the effect of the surface conductance. Moreover, I demonstrated the effect of surface defect engineering on perovskite solar cells. Many groups in the field are processing TiO_2 directly after annealing, assuming that the freshly annealed surface is optimal for the fabrication of *PSC*. I demonstrated that an additional UV-ozone treatment increases the local conductance through a TiO_2 anatase film, which leads to an increased fill factor and thus an increased photoconversion efficiency. This method can also be used for mesoporous TiO_2 films and SnO_2 films. Furthermore, we found that hydrocarbon contaminations play only a minor role when the samples are investigated directly after annealing or UV-ozone treatment. Recontamination of a freshly cleaned surface occurs in a matter of hours and significantly decreases the local conductance.

Chapter 5: Surface modification of semiconducting metal oxides with cSFM

Introduction

Many modern applications rely on surface patterning and local modifications on a microscopic or nanoscopic scale. Hydrophobic or omniphobic surfaces can be created with pillar structures that grow from respectively prepared surfaces.[168] Thin-film transistors strongly depend on the local arrangement and engineering of conducting properties. [142] New approaches of plasmon-enhanced optical sensors require well designed nanostructured surfaces. [169] Surface defects play a crucial role in photocatalytic water splitting of nanopillars.[170] Nanopattern structures are used to increase the outcoupling efficiency of LEDs.[171]

For all these devices, careful control over the local surface properties is important. Standard approaches in modifying a surface range from simple annealing to sputtering, wet-chemical treatment, printing or etching.[170] In the first part of this chapter, I demonstrate that cSFM can be an alternative route to locally modify and pattern surfaces without virtually any chemical waste using a conductive scanning force microscopy (cSFM) based approach. Local oxygen vacancies are created under the tip when conducting consecutive cSFM in the same area. This surface modification creates localized surface charges on semiconducting metal oxides as FTO and TiO_2. Therefore, cSFM can be used as a synthetic tool for deliberately changing local surface properties
In the second part of this chapter, I demonstrate, how the interface of an FTO / TiO_2 array is influenced by the choice of plasma-treatment of the FTO substrate. Using cSFM to both probe and alter the surface properties, I demonstrate novel memresisting properties of a TiO_2 thin film on an FTO substrate.

5.1 Local surface modification of semiconducting metal oxides with cSFM

Local charging of an F:SnO_2 surface with consecutive cSFM

Surface groups can be electrochemically cleaved by consecutive cSFM measurements.

For metal oxides as SnO_2 and TiO_2, the most common occurring surface defects are point defects as oxygen vacancies and hydroxyl groups.[172] These defects are normally formed during synthesis. However, surface metal-oxygen bonds can also be cleaved with high currents. Thus, new surface oxygen vacancies are formed as well as negatively charged deprotonated hydroxyl groups at the neighboring metal ion (Figure 60).[173] Upon further injection of electrons, the newly formed surface oxygen vacancies trap electrons and thus charge up negatively. Surface hydroxyl-groups are also deprotonated at a large enough applied bias, which further charges the surface. This surface charging can be induced locally with a conducting cantilever during a cSFM experiment. Bridging oxygen bonds are cleaved under the cantilever tip and create localized negative charges. These surface charges built up and act as a potential barrier for additional electrons from the cantilever tip.

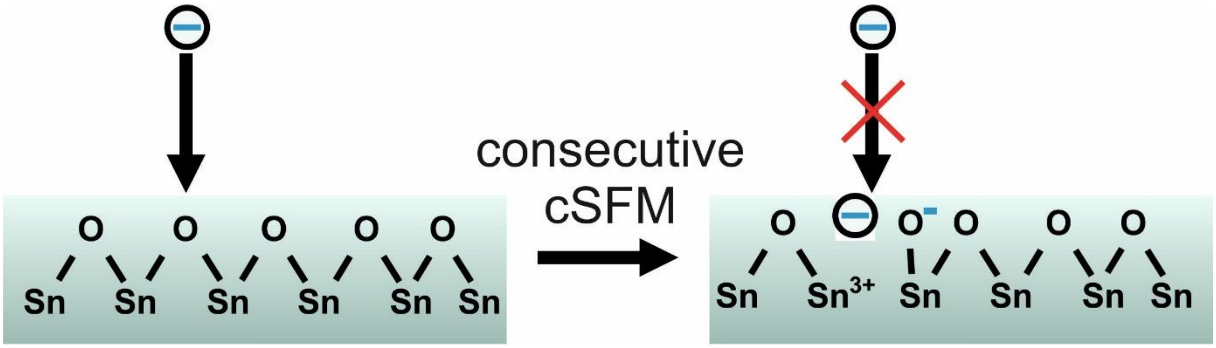

Figure 60: Schematic demonstration of electrochemical surface alteration of FTO surfaces with consecutive cSFM experiments. Surface metal-oxygen bonds are cleaned upon forming. New formed surface oxygen vacancies are filled with electrons.

Armstrong et al. published a macroscopic observation of that effect with an electrochemical surface alteration of FTO surfaces [174]. After conducting cyclovoltametry experiments on FTO substrates in an aqueous 0.5 M H_2SO_4 solution, they found a changed ratio of surface oxygen to surface tin ions. While a pristine surface showed a ratio of 2:1 oxygen to tin ratio, this increased to a ratio of 3.6:1. This increase can be explained with an electrochemical cleavage of bridging surface oxygen tin bonds and the formation of surface oxygen vacancies. In an aqueous H_2SO_4 solution, these surface oxygen vacancies are filled immediately with hydroxyl-groups coming from water molecules. Thus, the ratio of surface oxygen ions to tin ions is increased (Figure 61).

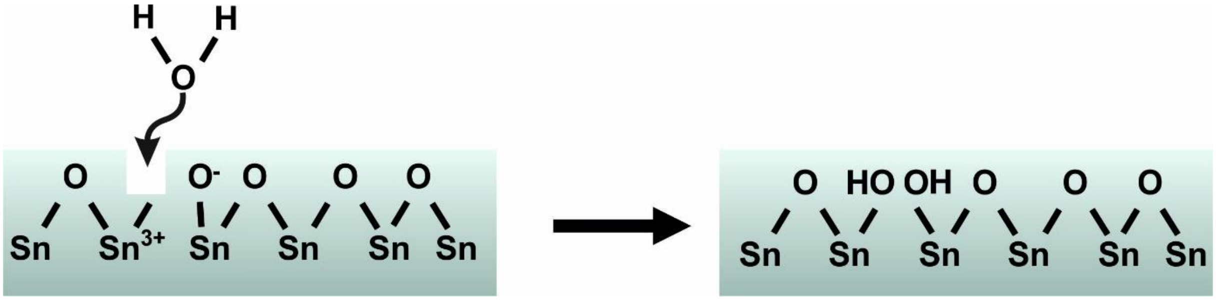

Figure 61: Water binds to surface oxygen vacancies of metal oxides and quench surface charges.

Consecutive measurements pattern the surface of fluorine-doped tin oxide surfaces.

In order to visualize this cleavage of surface bonds, I conducted cSFM experiments on FTO substrates. For that, I manually cleaned an FTO substrate and argon-plasma treated it for 30 min. Directly after the plasma treatment, I transferred the substrate to the cSFM setup and conducted consecutive measurements on the same area (Figure 61). For this set of measurements, a setpoint force of 20 nN was applied with a z-length of 300 nm, a pixel time of 10 ms and an external bias of 1.5 V. An area of 5 x 5 µm^2 was recorded with a resolution of 128 x 128 pixels using the “QI” mode.

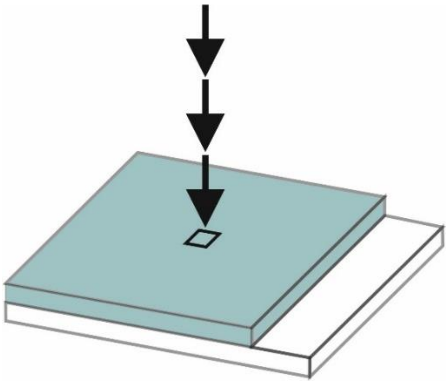

Figure 62: Consecutive cSFM experiments on the same are of a cleaned and argon plasma treated FTO.

The measured median current monotonously decreased with increasing measurement numbers in the same area (Figure 63 a). The median current decreased by 50 % from the initial current value of 88 pA for the first image to 44 pA for the fifth image. After 13 consecutive measurements, the median current dropped to 7 pA which corresponds to a decrease of 92 % compared to the initial value.

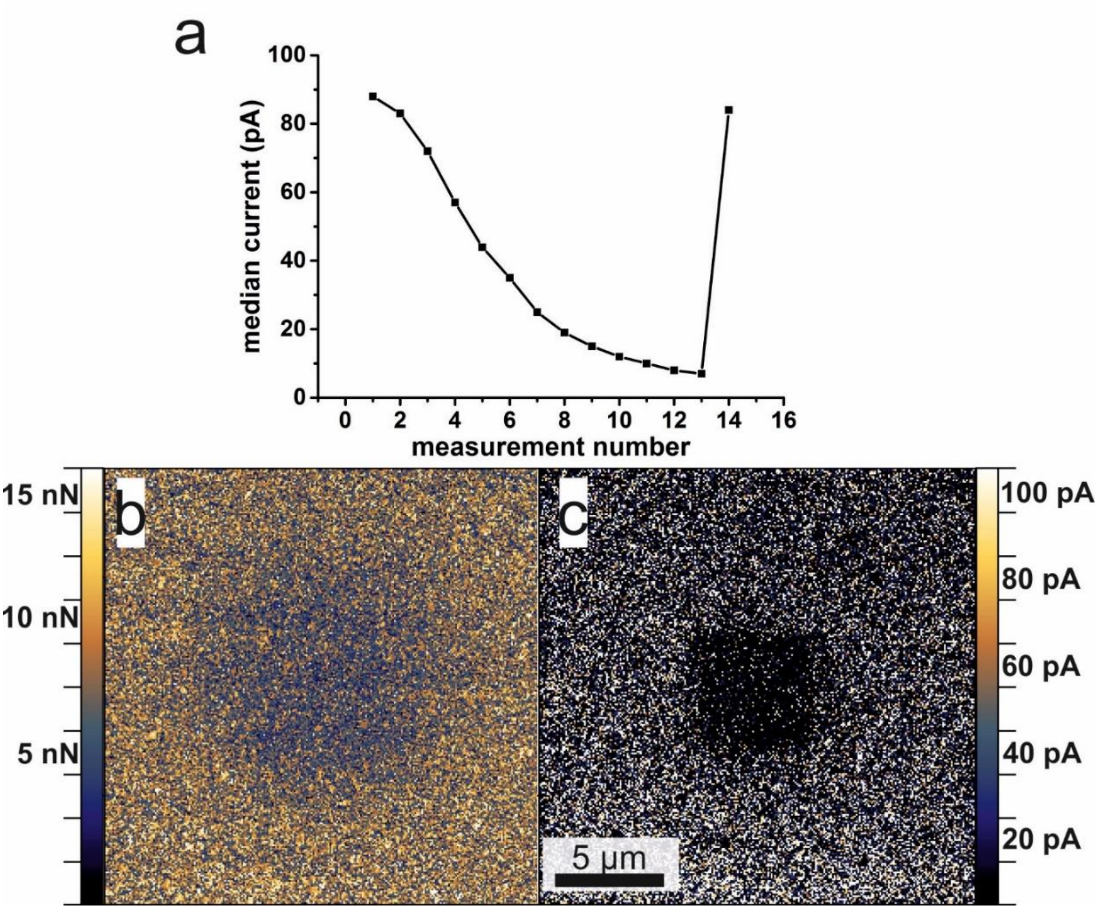

Figure 63: Development of the measured current over the course of consecutive measurements each on the same area of a manually cleaned and plasma cleaned FTO substrate. b) 20 x 20 µm Adhesion image of the previously measured area. c) 20 x 20 µm Adhesion image of the previously measured area. All images have the same scale bar.

This surface modification only occurs locally under the tip. I recorded an additional image in a new area in close proximity to the previously measured area directly after the first set of measurements. The measured median current increased again to 84 pA reaching almost the initial value of 88 pA of the first measurement. A consistent roughness of 19.1 ± 0.1 nm was measured in the same area during the set of consecutive measurements. Since the roughness did not change during the set of measurements, and since the initial current was restored at a fresh area, I concluded, that the decrease of median current was not due to changes in the conductive coating or shape of the tip.

In order to visualize this surface modification, I recorded a larger image of the measured area with a size of 20 x 20 µm². The previously measured area of 5 x 5 µm² is clearly visible in both the adhesion and current image (Figure 63 b and c). The adhesion image displays a region of reduced values, where the set of consecutive measurements has been conducted. Likewise, the median current is reduced in the area of the previous set of measurements. Both the reduced adhesion and the reduced median current can be accounted for an increased amount of local negative surface charges that repulse the negatively charged cantilever and act as an additional potential barrier for further electron.

The interaction between the cantilever tip and the surface can be described with a Lennard Jones Potential. Van-der-Waals interactions lead to an attraction with the range $\propto \frac{1}{r^6}$. The repulsive part is $\propto \frac{1}{r^{12}}$ and is called Pauli Repulsion. The Lenard Jones potential is the resulting net potential of these two parts (Figure 64 a, red curve).

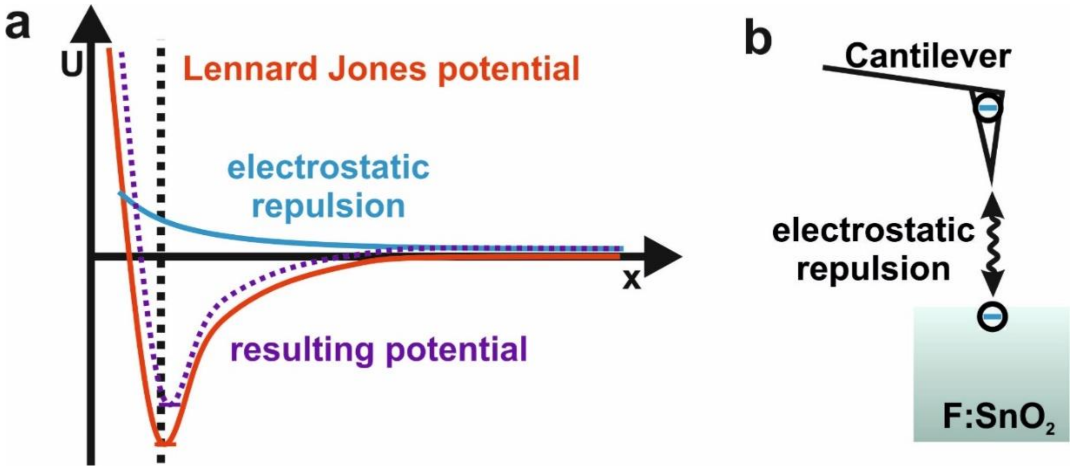

Figure 64: a) The effect of a surface charge on the interaction between the cantilever tip and the surface described with the potential over the distance. The Lennard Jones potential and the electrostatic repulsion of similar charges results in a combined potential with less attraction and the potential well. b) Schematic representation of the repulsion between the surface and the cantilever tip.

With additional surface charges on the surface and a similarly charged cantilever tip, an additional Coulomb repulsion occurs with $\propto \frac{1}{r^2}$ (Figure 64a, blue curve). The combination of both the Lennard Jones potential and the Coulomb repulsion leads to a resulting potential with a reduced net attraction at the potential well (e.g. the lowest point in Figure 64). Lower attraction leads to reduced adhesion of the cantilever to the surface (Figure 65).

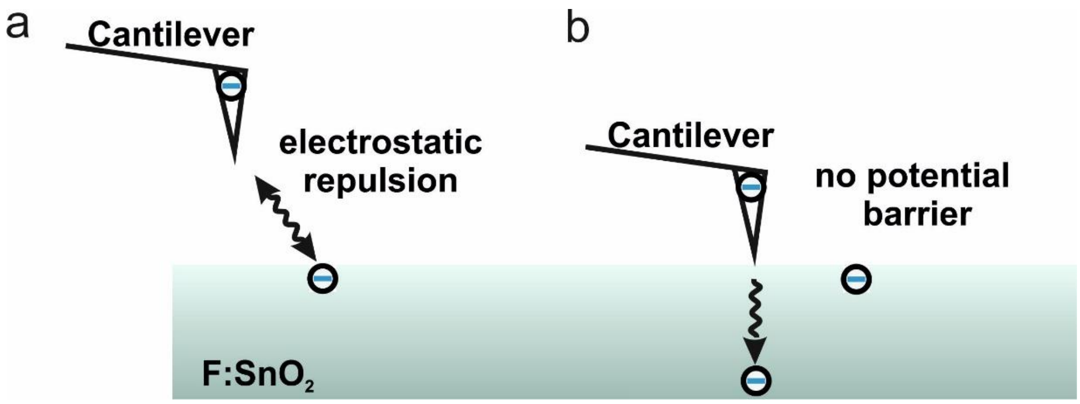

Figure 65: Localized surface charges act twofold. a) Negative surface charges also repulse the similarly charged cantilever over a certain distance when it doesn't approach directly vertical at the surface charge. b) During a cSFM measurement, an electric current only flows in direct physical contact between the cantilever and the surface. The conductance is only determined by the local surface contact resistance and the bulk resistance of the TiO_2 /SnO_2 system.

When comparing the adhesion image and the current image, it is obvious, that the effect of previous measurements is far more defined and sharp-outlined for the current image compared to the adhesion image. This observation is also rooted in the ionic nature of the surface modification. The repulsion of similar charges follows the Coulomb law with $F = \frac{1}{4\pi\varepsilon_0}\frac{q_1 q_2}{r^2}$. Therefore surface charges repulse the similarly charged cantilever over distance $\propto \frac{1}{r^2}$. In contrast, the local conductance is only measured and influenced by direct mechanical contact between the cantilever tip and the surface. Thus, only the contact resistance and the additional electric resistance of immediate surface charges affect the flow of current. Therefore, the observation that the current image is far more defined than the adhesion image support the model of localized surface charges.

cSFM induced surface modification of F:SnO_2 in humid conditions

The local metal oxide surface is also electrochemically modified in humid conditions.

This localized surface charge critically depends on the relative humidity. Ambient humidity is known to quench surface charges.[175,176] Water adsorbs at oxides surfaces in molecular form and in hydroxyl form, whereas the former demonstrates donor properties, the latter acceptor properties.[9] Likewise, the amount of cSFM induced surface charges is greatly reduced in humid conditions. Accordingly, I observed no distinguished changes in adhesion and current flow in similar experiments with relative humidity above 50 % (Figure 66 a and b).

However, surface Ti-O bonds are nevertheless cleaved with an applied external electric bias. At high relative humidity, freshly created surface oxygen vacancies are immediately filled with ambient water, which leads to an increase of surface hydroxyl groups similar to the process sketched before (Figure 61). Although this local increase of surface hydroxyl groups does not change the local conductance or adhesion, I was able to visualize the local surface modification via a change in the local work function, as I demonstrated with Kelvin probe force measurements (Figure 66 c).

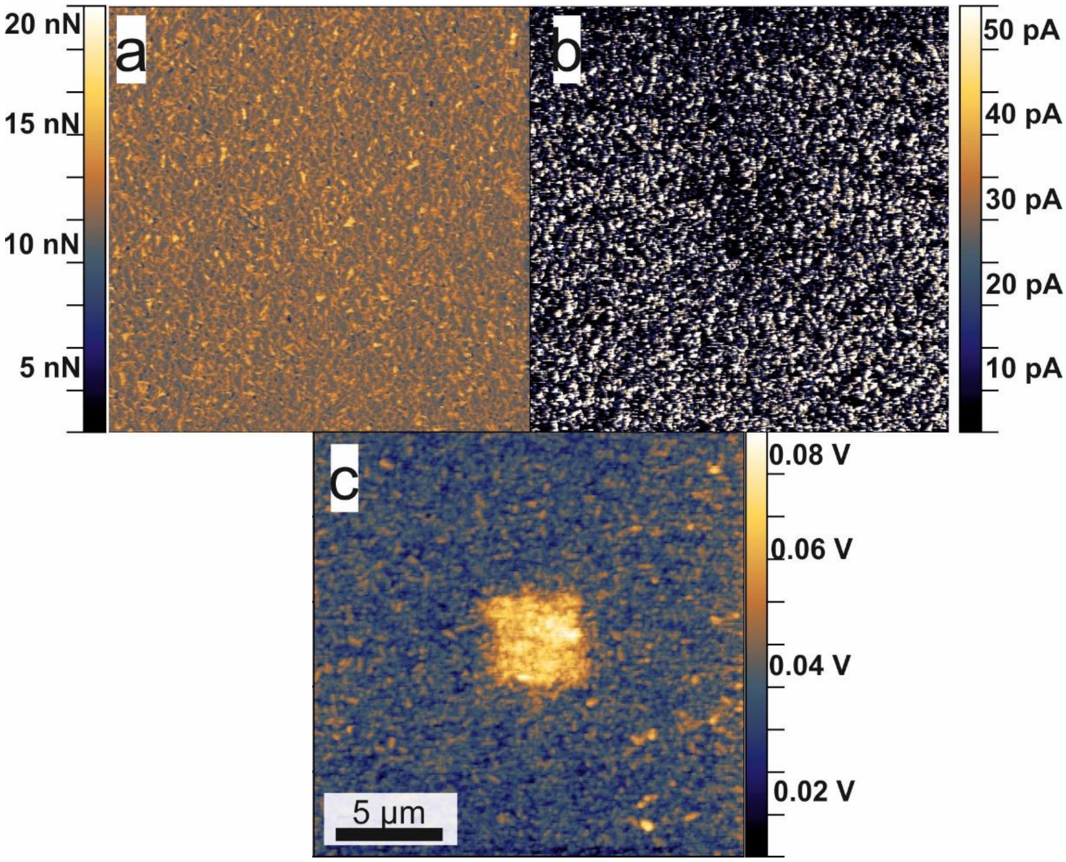

Figure 66: a) Adhesion image, b) median current and c) KPFM-surface potential image of a TiO_2 thin-film on FTO measured at ambient conditions with 50 % relative humidity. Ambient humidity quenches surface charges and prevents a reduction in measured adhesion or median current with consecutive measurements in the same area. Since the surface is nevertheless electrochemically altered, Kelvin probe force measurements demonstrate a local change in the work function, which is attributed to the increased amount of surface hydroxyl groups. All images have the same scale bar.

Since the modified area possesses an increased concentration of hydroxyl groups (-OH) compared to the pristine TiO_2 the surface modification probably creates an increased local electron density. The work function describes the energy needed in order to remove an electron from the surface into a vacuum. Accordingly, local changes in the surface electron density alter the local work function.

In summary, the lack of measurable changes in conductance and adhesion in humid conditions further promotes induced local surface charges with consecutive cSFM measurements. Moreover, the occurrence of changes in the local work function even in humid conditions support the model cleaved surface charges and addition of water.

It is worth mentioning, that I used FTOs with a surface resistance of 13 Ohm and 10 Ohm. FTOs with a surface resistance of 7 Ohm exhibited a reduced surface modification if any. I hypothesize, that this observation can be explained with a more metal conductor like behavior of the higher doped F:SnO_2 substrates. The high local conductance leads to more efficient energy dissipation and transport of electrons from the surface into the bulk. Also, 7 Ohm substrates display a higher surface F-doping concentration compared to 10 Ohm and

13 Ohm FTOs. The F-Sn bond is most likely not as easy cleaved as the O-Sn bond, which leads to surface passivation by the fluorine doping.

Local charging of a TiO_2 surface with consecutive cSFM

cSFM can alter different kinds of semiconducting metal oxide surfaces.

The cSFM-induced local surface modification is not limited to FTO but it can be applied to different semiconducting metal oxide surfaces. In order to demonstrate, that TiO_2 thin films can be modified in a similar fashion, I conducted cSFM experiments on freshly annealed TiO_2 thin films on cleaned and argon-plasma treated FTOs (Figure 67)

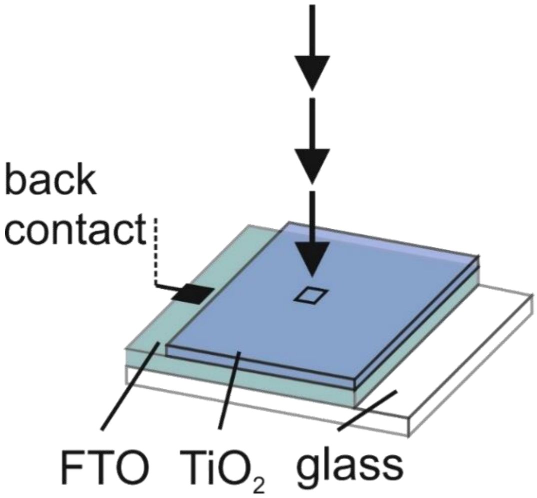

Figure 67: Consecutive cSFM experiments on the same are of a freshly annealed TiO_2 thin film on a cleaned and argon plasma treated FTO.

In a first qualitative experiment, I spin-coated a 1 M $TiCl_4$ solution on a freshly cleaned and argon-plasma treated FTO substrate. After annealing at 500 °C and cooling down to 150 °C, the sample was directly transferred to the cSFM setup. The first measurement was conducted with an image size of 1 µm². Then, an image with 10 x 10 µm² was measured immediately after the first (Figure 69).

Similar to the FTO treated sample, the morphology showed no changes after a previous measurement. The current image on the other hand clearly displays the previously measured area as a dark spot with a low conductance. The median current of that modified area was 2.7 pA; the median current of the rest of the image was 70.4 pA. This corresponds to a decrease of 3.8 % of the initial value.

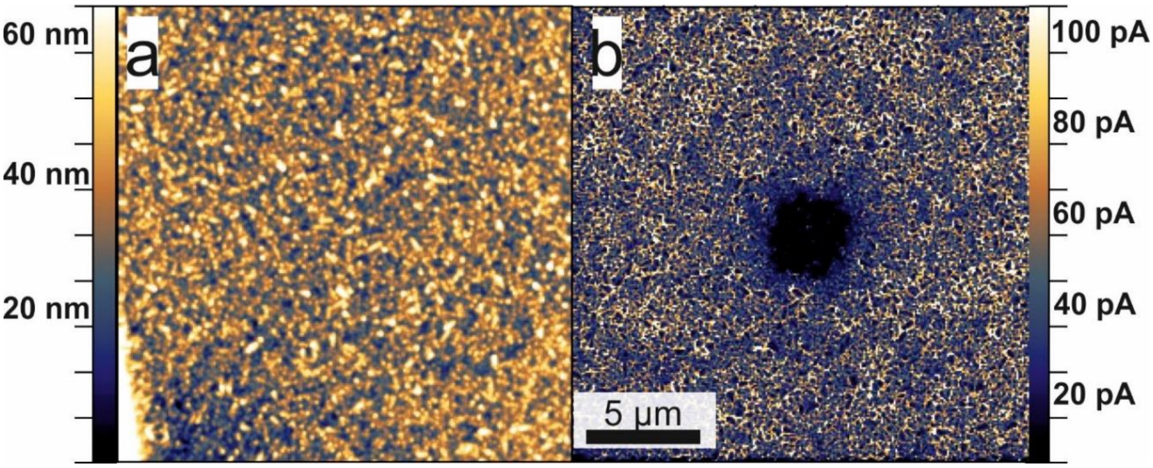

Figure 68: Influence of a previous cSFM measurement on the a) morphology and b) current image of a TiO_2 thin film on a cleaned and plasma-treated FTO substrate. The previous measurement with 1 x 1 µm and the displayed 10 x 10 µm image were conducted with a setpoint force of 40 nN a z-length of 150 nm a pixel time of 8 ms and an applied bias of 3 V. Each image has a resolution of 256 x 256 pixels. All images have the same scale bar.

The local modification is due to electrochemical stress.

In order to verify, that this effect is driven by the applied bias and not induced by mechanical pressure of the cantilever tip, I conducted a series of measurements of two fresh samples, that have not been altered by previous measurements. For the first set of measurements, I applied a constant bias of 2 V while measuring the same area repeatedly (Figure 69 red curve). For the second set of measurements, I exclusively applied an external bias of 2 V for the first and last measurements (Figure 69 black curve). Every other parameter was kept unchanged.

For the first set, the median current dropped from 134 pA to 93 pA after the first measurement, which is 69 % of the initial value. After the course of 15 consecutive measurements, a median current of 36.7 pA was measured. This decrease corresponds to a drop in median current to 27 %.
For the second set of measurements without any applied bias between the 2nd and 14th measurements, the median current dropped from 67.3 pA to 59.2 pA, which corresponds to 88 % of the initial value. Therefore, the modification of the surface depends on an applied external bias in order to cleave the surface bridging oxygen bonds. The second set of measurements showed lower decrease after 14 measurements than the first set after only one (Figure 69 red curve compared to the black curve).

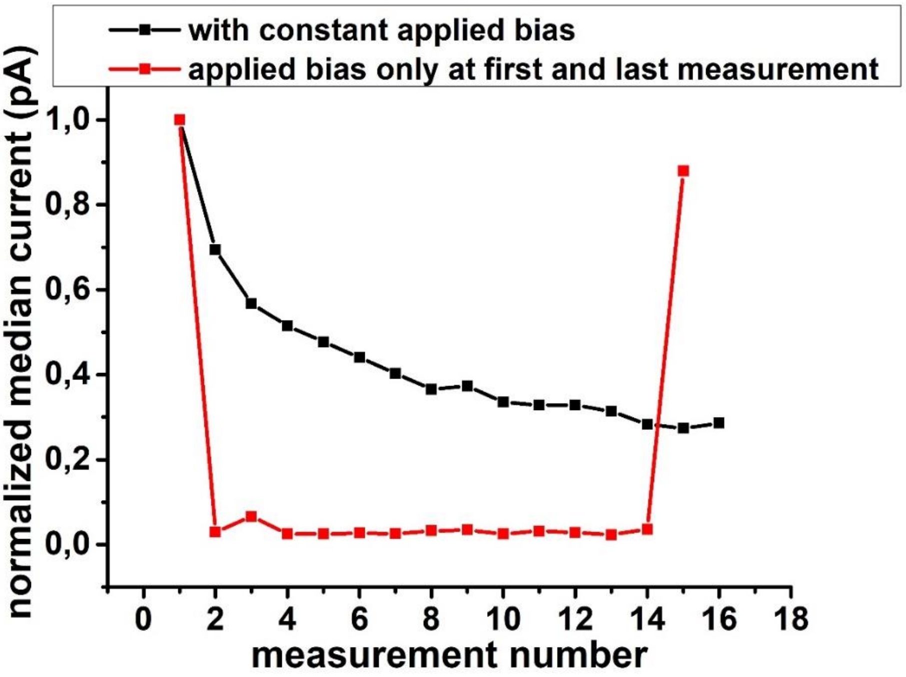

Figure 69: Development of the measured current over the course of consecutive measurements each on the same area of a freshly annealed TiO_2 thin film on a manually cleaned and plasma cleaned FTO. The black curve displays the progressing decrease of median current with a constant applied external bias. The red shows the progression of current with an applied external bias only for the first and last measurement. The far lower decrease of median current for the second measurement demonstrates, that the surface modification depends on an applied external bias and is not due to mechanical modification of the surface. Each image was recorded with a setpoint force of 25 nN, a z-length of 120 nm and a pixel time of 7 ms. Each image had a size of 5 x 5 µm with a resolution of 128 x 128 pixels.

This weaker decrease can be attributed to two effects. First, each measurement roughly took 3 min. to measure. Therefore, roughly 40 min passed between the first and last measurement. Within this time, surface charges can be quenched by ambient water in the atmosphere. During that day, relative humidity of approximately 25 % was measured. A second factor might be the cantilever itself. Since the cantilever is conducting, it can act as a pathway for electrons and thus remove surface charges.

The effect of locally induced surface charges was also reflected in my choice of image parameters. An image size of 5 µm x 5 µm with a 128 x 128 pixels yielded the highest medium current. The measured current decreased when I increased the number of pixels or decreased image size. This observation was caused most likely by overlapping pixel areas. When measuring an image 5 µm x 5 µm image with a 128 x 128 pixels, a distance of approximately 40 nm was between each pixel. The used cantilever “SCM-PIT-V2” had a typical tip radius of 25 nm. Therefore, the fringes of each pixel area start to overlap, when decreasing the image size or increasing the number of pixels per image. Accordingly, this overlapping pixel area would be in contact with the cantilever for two force-distance curves and experience the surface modification twice. Again, locally induced surface charges act as an additional potential barrier and decrease the current flow for the overlapping area and reduce the measured current for the pixel. However, I did not observe any increase in current when increasing the image size above 5 µm x 5 µm.

Conclusion

I demonstrated, that consecutive scanning force microscopy experiments alter the surface of semiconducting metal oxide surfaces as FTOs and TiO_2 thin films. This local modification is due to electrochemical cleavage of surface metal-oxygen bonds, which creates surface oxygen-vacancies and localized surface charges under the cantilever tip. This modification of surface defects is reflected in a reduced local conductance and adhesion. Accordingly, the work function is increased locally, which persists even in conditions with high ambient humidity. The surface modification is not due to mechanical stress but requires an applied external bias.

The cSFM induced local surface modification could be a promising alternative route to pattern semiconducting metal oxide surfaces. By locally increasing the number of surface charges and oxygen vacancies, this approach could be a potential route to create highly reactive areas that show an increased affinity to surfactants as silanes, Grignard reagents, and other organic or inorganic molecules. Thus, cSFM based techniques could be used synthetically for nano-pattern areas for follow-up reactions. In a broader contact, my findings further develop the toolbox of scanning probe lithography (SPL). In a recent review, R. Garncia et al. give a detailed overview of different SPL based approaches, e.g. thermal and thermochemical SPL, oxidation SPL and bias-induced SPL.[177] Bias-SPL has been applied to locally oxidize silicon semiconductors and to write an array of positive charges onto a SiO_2 surface, that act as reactive sides for selective protein adsorption.[178,179]. My work presents a novel route to locally reduce semiconductors and create an array of negative charges onto different metal oxides.

Moreover, localized surface charges could be a route for storing information. If these changes persist in a dry environment, local negative charges could be written onto the surface with a cSFM approach. Using a non-contact mode like KPFM, this stored information could be read without altering the information. However, competing with modern top-notch hard disks would challenging. Since 2015, Seagate produces a hard drive with a density of 1.23 $Tbit/in^2$ which corresponds to a bit size of approximately 22 nm x 22 nm. The diameter of a standard cantilever tip is 20-40 nm. Nevertheless, in contrast to the binary magnetic storage of a hard disc with “on” and “off”, a charge based system could have more states than two, based on the amount of charging. A non-binary storage approach could lead to a higher storage density despite larger individual “bits”.

5.2 The influence and interplay of the FTO / TiO_2 interfaces

The choice of plasma treatment not only affects the surface conductance of FTOs, but it also affects the interaction of the FTO layer with a spin-coated TiO_2 thin film. Using cSFM, I demonstrate how different treated FTO and TiO_2 layers exhibit different electrical and chemical behavior when probed and measured with cSFM. Understanding the interplay between two semiconducting metal oxides could pave the road to new thin-film transistors or memristors.

5.2.1 The choice of plasma treatment of an FTO substrate changes the surface behavior of a spin-coated TiO_2

Oxygen plasma treatment creates a thin layer of undoped SnO_2 that acts as a potential barrier for electrons from the TiO_2 layer.

As described in Chapter 4, the choice of plasma treatment modifies the surface of a treated FTO and changes its surface defects as well as the concentration of fluorine dopants. Whereas argon-plasma treated FTOs possess the same doping density at the surface as within the bulk, oxygen plasma treatment of FTOs leads to the formation of a thin layer of undoped SnO_2 (Figure 70).

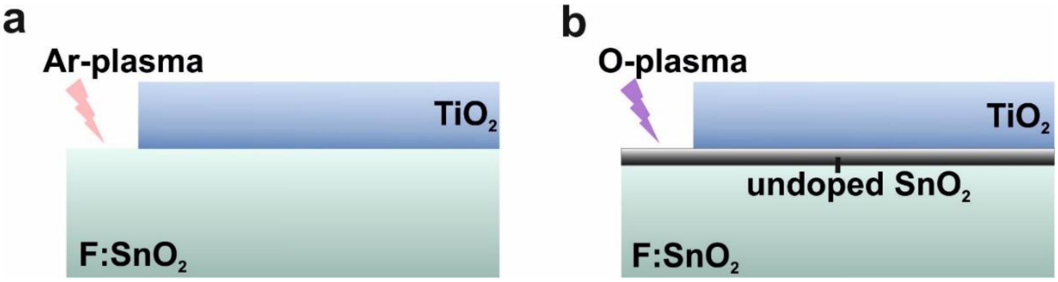

Figure 70: Schematic representation of a TiO2 thin film on a) an argon-plasma treatment FTO and b) an oxygen-plasma treated FTO.

Moreover, oxygen-plasma consists of highly reactive oxygen ions, that bind chemically to surfaces.[135,139] As a result, the freshly formed SnO_2 has a very low n-doping concentration due to a low concentration of surface Fluorine dopants or oxygen vacancies. Therefore, when spin-coating a TiO_2 thin film on an oxygen-plasma treated FTO substrate, the resulting system is an array of an $F:SnO_2$ layer, an undoped SnO_2 interlayer, and the TiO_2 layer.

The respective energy levels of this interlayer crucially influence the transport characteristics across these three layers. Electrons migrate from higher energy levels to lower energy levels. Accordingly, electrons migrate typically from materials with a high Fermi-level (smaller work function and high conduction band edges) to materials with a low Fermi-level (higher work function and low conduction band edges).

The Fermi-Level and the effective band edges depend depends on the dopant concentration of a semiconductor. In an n-type semiconductor as TiO_2 or SnO_2, the Fermi-Level rises with increasing n-doping. Additionally, recent studies demonstrate, that the work function of metals and semiconducting metal oxides strongly depend on how the surfaces have been prepared.[117,180–185] A polycrystalline gold film exhibits a work function from 4.4 - 4.7 eV in ambient conditions and 5.3 - 5.4 eV after argon-plasma cleaning.[184] For indium-tin-oxide surfaces, the work function can range from 4-3 eV to 4.8 eV depending on the nature of the surface preparation. For FTO, a work function of 4.4 – 5.0 eV has been reported. [117] Furthermore, the work function of semiconductors also depends on external factors like the temperature.[183] Direct comparison of reported values from literature is therefore difficult.

However, H.Sun et al. studied the influence of surface doping concentration on the energy levels and work function of $F:SnO_2$.[141] They directly compared the energy level of an $F:SnO_2$ layer with a very thin SnO_2 cover layer compared to an uncoated $F:SO_2$ layer. They report that the conduction band edge of undoped SnO_2 thin is approximately 0.8 eV deeper than the conduction band edge of $F:SnO_2$.[141] In contrast, it has been reported, that TiO_2 possesses a 0.36-0.44 eV higher conduction band edge compared to $F:SnO_2$.[186]

Thus, when spin-coating a TiO_2 thin film on an oxygen-plasma treated FTO, the lower SnO_2 conducting band is sandwiched between the higher conduction bands of TiO_2 and $F:SnO_2$ (Figure 71). In a solar cell, photon-excited electrons are injected from the light-absorbing perovskite layer into the TiO_2 layer. When measuring cSFM, electrons are injected the cantilever tip. These charge carriers can migrate through the TiO_2 film until they reach the SnO_2 / TiO_2 interface. Since the energy level of the conduction band edge of the SnO_2 layer is lower than the band edge of the TiO_2 layer, electrons can easily migrate into the lower energy state. But since the undoped band edge of SnO_2 is lower than the band edge of the doped $F:SnO_2$ electrons must overcome a potential barrier to migrate into the FTO. Thus, electrons are pinned at the undoped SnO_2 layer, which basically acts as an electric resistance. Accordingly, the resistance of the undoped SnO_2 interlayer increases with more pinned electrons.

Surface oxygen vacancies provide electrical pathways for electron migration across the TiO_2 surface.

Therefore, with progressing charge injection into the TiO_2 the electric resistance of this interlayer rises. Electrons always follow the path of the least resistance. The lowest energy states within the TiO_2 thin film are created by surface oxygen vacancies.

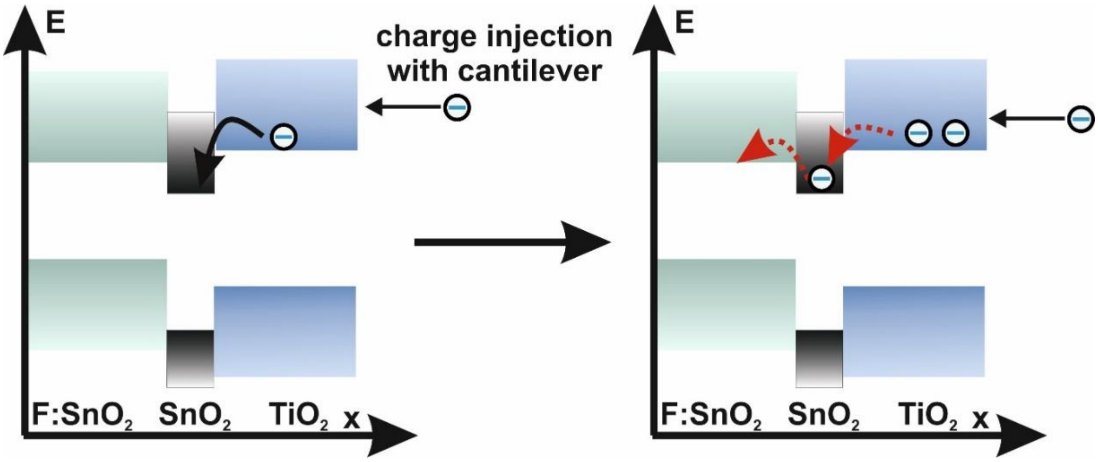

Figure 71: Band Diagram for the interface of F:SnO$_2$ / SnO$_2$ / TiO$_2$. Oxygen plasma treatment creates a thin layer of undoped SnO$_2$. This interlayer has a larger bandgap than F:SnO$_2$ and lower conduction band edge due to a low amount of dopants. Therefore, electrons must overcome a potential barrier, when migrating from the TiO$_2$ layer into the FTO.

H.Y. Chong et al reported that surface oxygen vacancies can also act as charge pathways lateral cross a TiO$_2$ surface. [159] They studied thin-film transistors utilizing thin TiO$_2$ channel layers between two Aluminium gates and found, that undesired off –current in these transistors was linked to charge transport across the surface of the TiO$_2$. Furthermore, they linked this surface charge transport with surface oxygen vacancies and saw a decreased off-current after UV-ozone treatment.

However, these surface defects create deep electron trap states and thus act as surface electron traps (chapter 4). Accordingly, these deep surface traps states are filled with electrons with continuous charge accumulation within the TiO$_2$ layer when conducting consecutive cSFM measurements. In short, surface oxygen vacancies act twofold: they facilitate charge transport in parallel across a TiO$_2$ surface but hinder charge transport vertical into the TiO$_2$ bulk. Thus, with an increased electric resistance through the TiO$_2$ thin film due to a SnO$_2$ interlayer, more electrons are transported across the TiO$_2$ surface.

Please note, that this surface charging is different from the one, that occurs only locally with consecutive measurements on the same TiO$_2$ area (chapter 5.1). Here, the SnO$_2$ interlayer acts as an additional potential barrier between the FTO and the TiO$_2$ layer and enforce the charge transport across the TiO$_2$ /air interface (Figure 72).

This migration of electrons across the surface oxygen vacancies lead to a global surface charge across the whole TiO$_2$ film and not only under the cantilever tip. Thus, consecutive measurements do not lead only to a local decrease of median current, but to a global decrease with progressing measurement Figure 72 a). Since an undoped interlayer of SnO$_2$ is created with oxygen-plasma treatment, the choice of plasma and therefore the interface between F:SnO$_2$ and TiO$_2$ also strongly affects the TiO$_2$ / air interface.

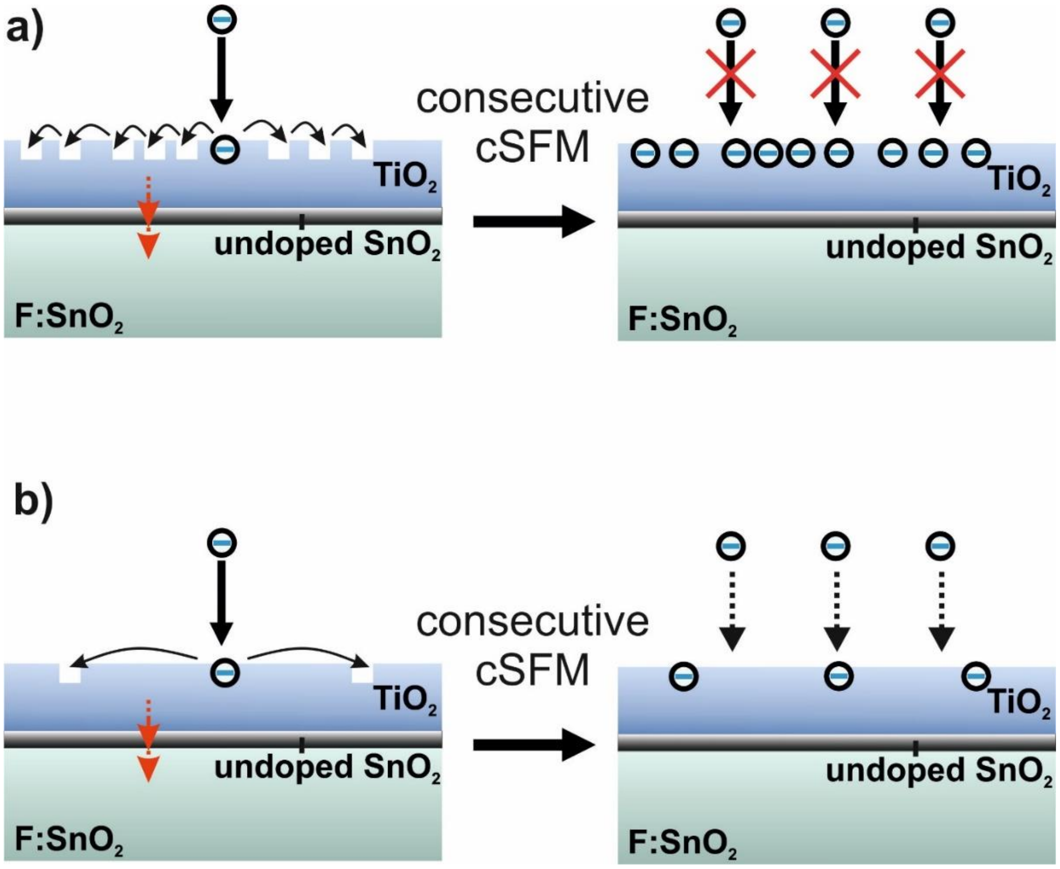

Figure 72: Oxygen plasma treatment of FTO substrates leads to the formation of a thin layer of undoped SnO_2. This interlayer hinders the transport of electrons from the TiO_2 layer into the FTO. Upon cSFM experiments, electrons are trapped at surface oxygen vacancies that create deep sub-bandgap states. Electrons can migrate from one trap site to another and thus charge up the surface across the whole substrate a) A TiO_2 thin film on an FTO substrate exhibit a high concentration of surface vacancies. Trapped electrons charge the surface and act as a potential barrier. b) UV-ozone treatment decreases the number of surface traps which leads to a lower surface charging and thus a smaller potential barrier

The TiO_2 surface charges less during consecutive cSFM with UV-ozone treatment.

In order to demonstrate, that the global charging of a TiO_2 thin film on oxygen-plasma treated FTO is mediated by surface oxygen vacancies, I prepared two spin-coated 30 nm TiO_2 films on two freshly treated FTO substrates. One sample was subjected to an additional 30 min of UV-ozone treatment, the other was directly measured after annealing.

As expected, the measured current decreases with increasing measurement number (Figure 73). After four consecutive measurements on different areas across the surface, the measured average current dropped to 40 % from 12.5 pA to 5.1 pA for the untreated TiO_2 film. After 16 consecutive measurements, the average current dropped to 15 % of the initial value to 1.8 pA, which is within the noise level. It can be expected that this decrease would be even stronger if the initial value was higher compared to the noise level. The UV-ozone treated sample showed an initial average current of 671 pA. After 16 consecutive measurements, the average current remained 58 % of the initial value by dropping to 390 pA. Therefore, a reduced number of surface oxygen vacancies lead to a reduced global surface charging of a TiO_2 thin film. Even after 16 consecutive measurements, the average current was two orders of magnitude above the noise level.

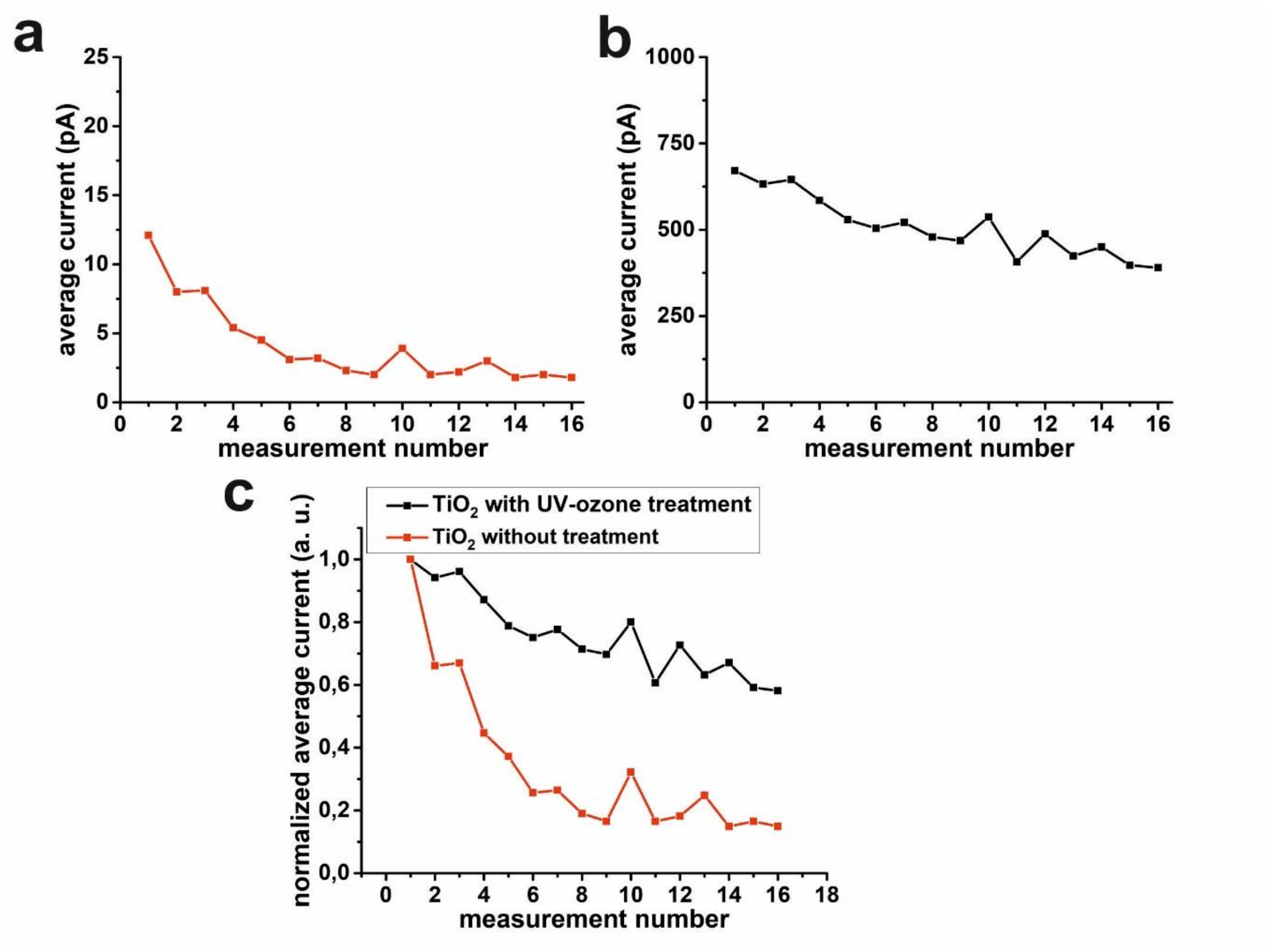

Figure 73: Development of the measured average current over the course of consecutive measurements. Each measurement was conducted on a new area of a 30 nm thick TiO_2 film on an oxygen-plasma treated FTO with a peak force of 20 nN, a z-length of 150 nm a pixel time of 8 ms and an applied external bias of 2 V. Each image had a size of 5 x 5 µm² and a resolution of 128 x 128 pixels. Between each measured area was at least 5 µm distance.
a) Development of the average current over the course of consecutive measurements for a TiO_2 thin film without UV-ozone treatment.b) Development of the average current over the course of consecutive measurements for a TiO_2 thin film without UV-ozone treatment. Please note, that the average current was used for this presentation. The median current of the untreated was slightly above noise level first measurement and dropped to noise level for the following measurements. Such low currents conceal any existing trend. Since the average current usually display the same trend with higher values, I decided to use the average current in this case.

Conclusion

Oxygen-plasma treatment of FTOs creates a thin layer of undoped SnO_2. This interlayer acts as a potential barrier and hinders the transport of electrons from the TiO_2 layer into the FTO. Accordingly, the electrons follow the pathway of least resistance and are redirected. Since surface oxygen vacancies of the TiO_2 layer create deep electron trap states, the TiO_2 / air interface charges up with continuous charge injection into the TiO_2 with a cantilever. These surface states mediate charge transport across the TiO_2 surface. Subsequently, charging up across the whole TiO_2 surface was reflected in a reduced flow of current over the course of consecutive measurements cSFM measurements on different areas across the TiO_2 film. UV-ozone treatment of the TiO_2 film reduced the number of surface oxygen vacancies and thus reduced the global charging across the TiO_2 film.

These findings offer another puzzle piece for understanding the charge transport in arrays of metal oxides such as in perovskite solar cells. Surface oxygen vacancies at the TiO_2 thin film lead to a reduced charge transport through the TiO_2 layer but increase the charge transport parallel to the surface and thus enable additional pathways for unwanted recombination or side reactions in perovskite solar cells. This charge transport parallel across the surface of TiO_2 films decreases also the on/off –ratio of thin films transistors, as first described by H Y. Chong, et al.[159] I confirmed their hypothesis on a microscopic scale, that surface oxygen vacancies enable charge transport across TiO_2 thin films and thus create unwanted high off-currents of thin-film transistors.
Even so, my findings of parallel charge transport across a semiconducting metal oxide layer could indicate a beneficial route for improving LEDs. The recombination of charge carriers is the fundamental mechanism for converting electric energy into light in LEDs. Engineering of surface oxygen vacancies could lead to well-distributed electrons, that are pinned to the interface which could promote light-emitting efficiency.

5.2.2 Mobile oxygen vacancies create memresisting properties in an FTO / TiO_2 array

A Memresistor changes its electric resistance depending on the current transported through it.

Memristors are a novel class of electronic elements, that depends on the migration of bulk oxygen vacancies. Such a memresistor changes its electric resistance depending on the history of current that was transported through that element. It was first hypothesized by L. O Chua in 1971.[187] The first example of a memresistor was published in 2007 by D. B. Strukov et al., who constructed an array of undoped and highly doped TiO_2 thin films between two platinum electrodes.[188] They could switch the electric resistance of these two TiO_2 electrodes by migrating oxygen vacancies between the two TiO_2 layers in an applied external bias of 1 V (Figure 74).

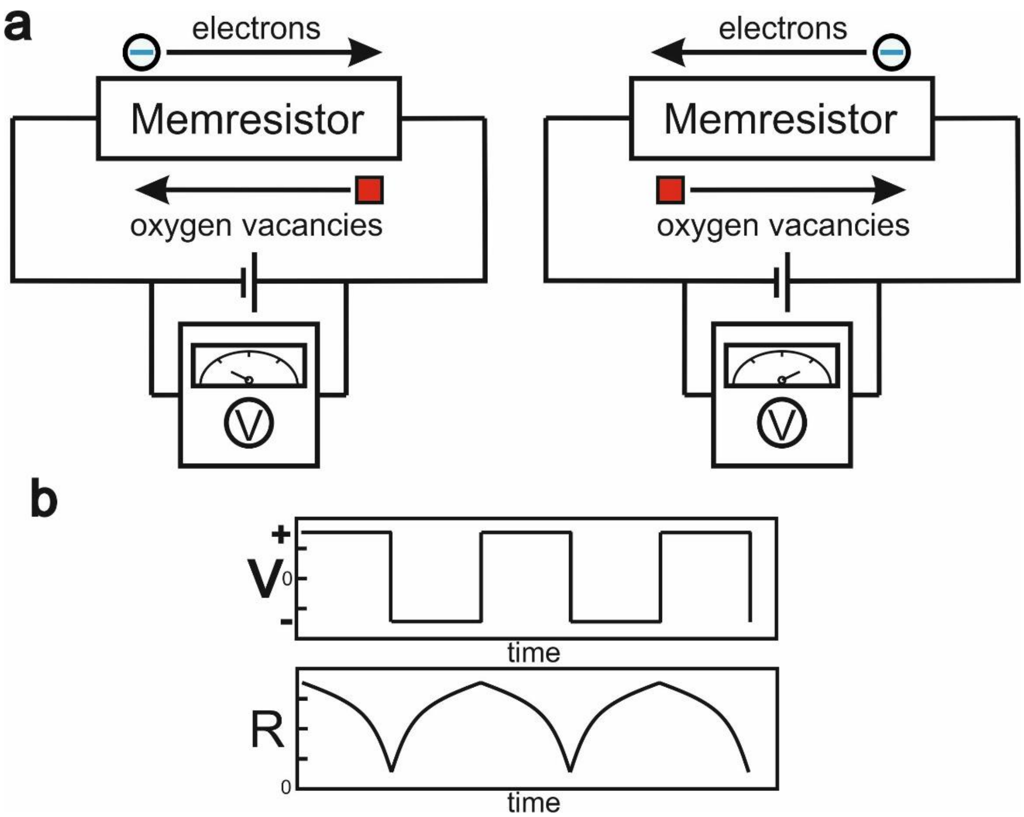

Figure 74: Working principle of a memresistor. a) The direction of current through the memresistor determines the migration of oxygen vacancies. b) The resistance changes over time depending on the applied external bias.[189]

Migrating bulk oxygen vacancies change the doping concentration in n-type semiconducting metal oxides as TiO_2, SnO_2, and WO_3.

T. Shi et al. described a thin film array of Pt/WO_3/FTO that showed memristive properties.[190] They demonstrated a switchable electric resistance with an applied external bias between 1.5 - 4 V and attributed this effect to the migration of oxygen vacancies from the FTO into the WO_3 layer. With increasing applied external bias, they observed a decreasing electric resistance that is caused by more migration of vacancies into the WO_3 layer. Similar to TiO_2, oxygen vacancies act as n-dopants within the WO_3 crystal and increase the conductance.Y. Kim et al. reported, that migration of oxygen vacancies through a TiO_2 film can also be induced locally with cSFM techniques.[191] They studied the induced crystallization of an amorphous TiO_2 thin film on Si/SiO_2 using additional electrochemical strain microscopy (ESN) transmission electron microscopy (TEM). Upon applying an external bias in the range of $\pm$ 6 V with a cantilever, oxygen vacancies migrated in the opposite direction of the flow of electrons. Although a multitude of different layered metal oxides shows memresisting properties, no actual devices have been realized to this date. Therefore, further study and easy and cost-efficient means of production are needed.

Bulk oxygen vacancies can migrate between TiO_2 thin films and argon plasma treated FTOs.

An FTO / TiO_2 array could be a new and low-cost route to memristors. FTO substrates and TiO_2 /TiO_2-precursors are widely commercially available and consist of earth-abundant elements. Many different routes have been reported for preparing homogenous TiO_2 thin films on FTO. (chapter 2). However, to the best of my knowledge, no one so far has observed the memresisting properties of a TiO_2 /FTO array. In order to achieve memresisting properties, the FTO / TiO_2 must be prepared in a way, that allows the free flow of both electrons and oxygen vacancies.

Argon-plasma treatment of an FTO efficiently removes contaminations without altering the F-doping concentration of the surface, and therefore, enables facile electron transport from the TiO_2 into the FTO (chapter 3). Moreover, argon plasma is known for creating surface oxygen defects in metal oxide surfaces.[192] Therefore, spin-coating a TiO_2 layer on an argon-plasma treated FTO leads to a defect-rich FTO / TiO_2 interface with a high concentration of oxygen vacancies within the FTO. Thus, argon plasma treatment of the FTO creates a surface that not only improves electron injection into the FTO but also enables short migration pathways for oxygen vacancies into the TiO_2 layer. For optimizing such an array for memresisting properties, not only the FTO / TiO_2 interface but also the TiO_2 / air interface must be prepared accordingly. I demonstrated, that UV-ozone treatment removes surface oxygen vacancies of the TiO_2 thin film and thus prevent a pile-up of charges at the TiO_2 / air interface (chapter 4 and chapter 5.1).

An FTO / TiO_2 array, that has been prepared in such a way, offers optimal surface properties of showing memresisting properties (Figure 75).

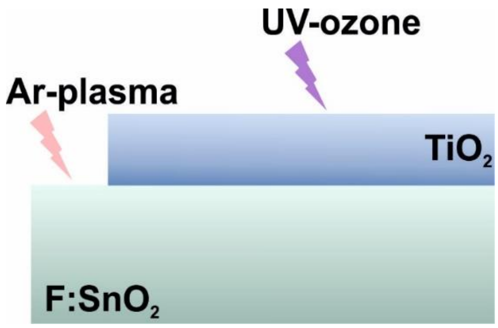

Figure 75: Preparation of a memresisting array of a TiO_2 thin film on an FTO substrate.

Upon injecting electrons via an external bias with a cantilever tip, oxygen vacancies start to migrate from the FTO interface into the TiO_2 bulk (Figure 76 a).

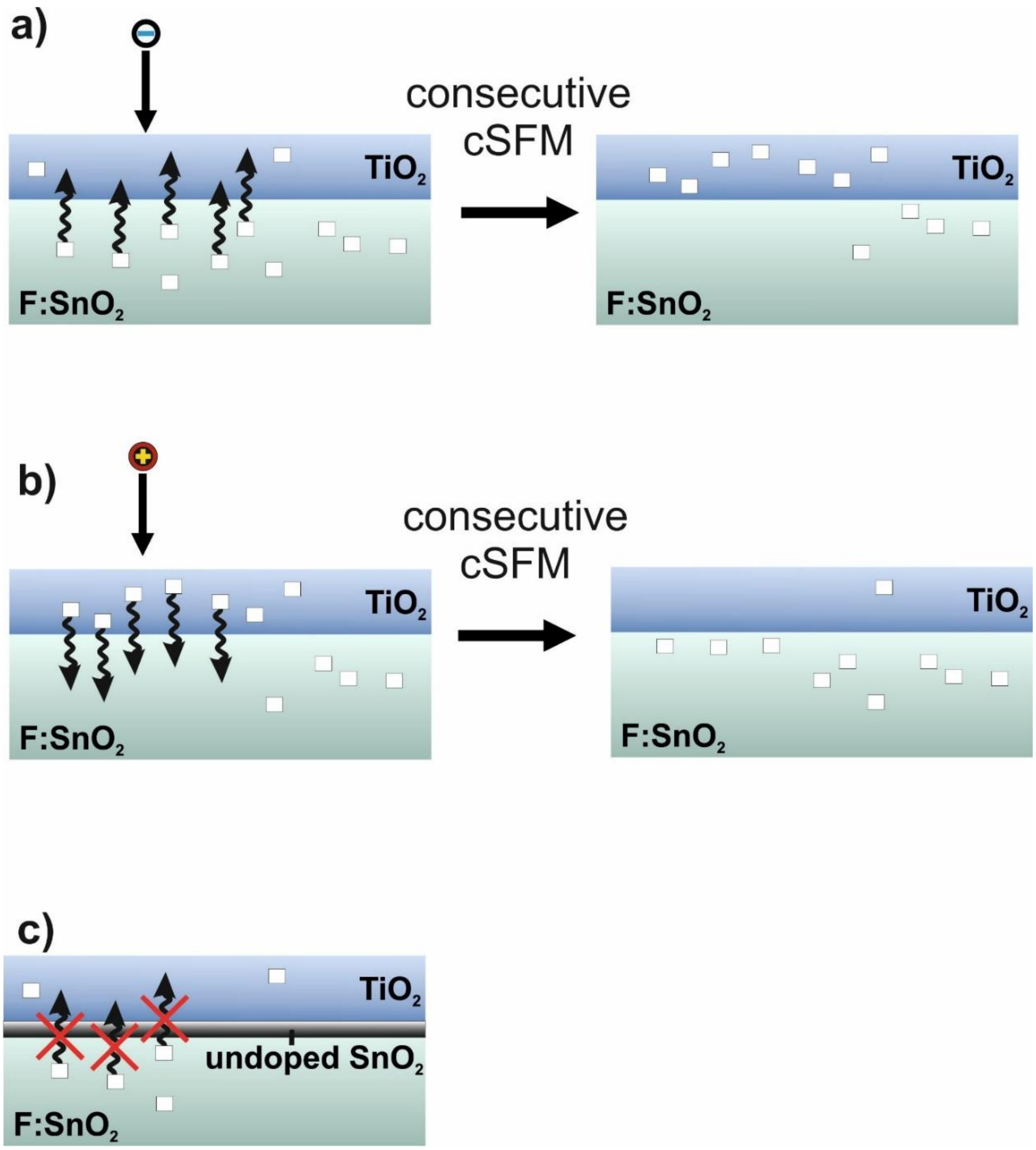

Figure 76: Bulk oxygen vacancies (V_O) naturally occur in FTO and TiO_2. They migrate with an applied external potential across the layers. The direction of flow is opposite to the direction of electron migration. (QUELLE) a) When applying a positive potential, electrons are injected with the cantilever into the TiO_2 layer. Oxygen vacancies migrate from the FTO layer into the TiO_2 while electrons move from the TiO_2 into the FTO. b) When applying a negative potential, holes cannot move through the TiO_2 layer into the FTO, since TiO_2 is an n-type semiconductor. Nevertheless, a strong local electric field drives the migration of oxygen vacancies from the TiO_2 into the FTO layer. c) Oxygen-plasma treatment creates a thin interlayer of undoped SnO_2 that acts as a potential barrier for electrons and delay the migration of oxygen vacancies from the FTO into the TiO_2.

Since oxygen vacancies act as n-dopants within the TiO2 crystal, this migration of oxygen vacancies leads to an increased n-doping of the TiO_2 thin film and thus an increased conductance. However, this migration of oxygen vacancies does not affect the conductance of the FTO layer because of two reasons. First, the FTO layer is with 1 µm thickness roughly two orders of magnitude thicker than the TiO_2 layer. Oxygen vacancies that migrate from the

FTO interface into the TiO_2 are replaced by oxygen-vacancies from the FTO bulk. Therefore, the vacancy density in the FTO is probably not altered in a significant amount. Second, the FTO is additionally doped with fluorine ions, that provide n-type semiconducting properties. Although no exact information about the surface doping ratio was available, T. Shi at al. estimated for both the F- ions and oxygen vacancies a concentration in the order of 10^{19} to 10^{20} cm^{-3}. [190] Thus, the n-type semiconducting properties remain unaffected and the FTO acts as a reservoir for oxygen vacancies.[190] T. Shi et al. also estimated a drift velocity of oxygen vacancies around $\sim 1.5 \text{ nm s}^{-1}$.
For a typical cSFM experiment, I apply an external bias of 1.5 V with a z-length of 150 nm, a pixel time of 8 ms for 128 x 128 pixels. During one single force-distance curve, the cantilever is in contact with the surface for approximately 0.8 ms. Therefore, while recording one full image, the cantilever is in contact with the sample for roughly 13 s.
Accordingly, the oxygen vacancies could migrate up to $1.5 \cdot \text{nm s}^{-1} \cdot 13 \text{ s} = 19.5 \text{ nm}$. Therefore, it is plausible that oxygen vacancies can migrate from the FTO / TiO_2 interface into the bulk of the TiO_2 thin film.

In contrast to the local surface modification under the tip described above, this migration of oxygen vacancies does not only occur directly under the cantilever tip (chapter 5.1). The driving force for the oxygen vacancies migration is the electric field, which is created by the applied bias via the cantilever tip. The origin of that field is at the contact point of the cantilever tip with the surface (Figure 77).

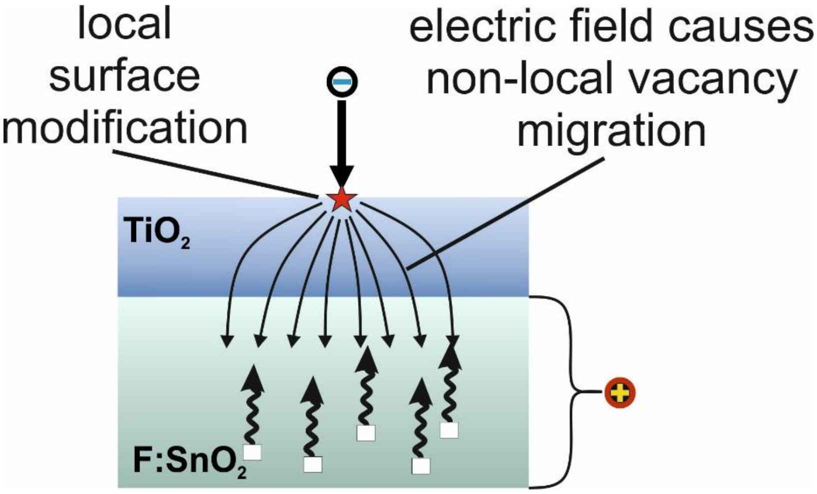

Figure 77: The oxygen vacancies migrate in the electric field that originates from the contact point of the cantilever tip. Therefore this effect does not only occur locally under the cantilever tip.

The expanse of that field is influenced by the contact resistance of the tip to the surface, as well as the electric resistance of the TiO_2 bulk and the resistance of the FTO / TiO_2 interface. Since the applied external bias also influences the extent of the electric field, further studies are needed in order to estimate the range, direction, and speed of vacancy migration.

In essence, consecutive cSFM measurements on an UV-ozone treated TiO_2 at an argon-plasma treated FTO leads to oxygen-vacancy migration from the FTO into the TiO_2 and thus to an increase of conductance of the TiO_2 layer.

TiO_2 thin films on argon plasma treated FTO demonstrate memresisting properties when measured with cSFM.

In order to demonstrate this effect, I conducted a set of measurements on a manual cleaned FTO substrate that has been exposed to 30 min of argon plasma treatment prior to TiO_2 thin film synthesis (Figure 78). Argon-plasma treatment removes any interlayer of undoped SnO_2 and thus guarantees good electric contact with the adjacent layer (chapter 4). Additionally, the TiO_2 layer was UV-ozone treated for 30 min

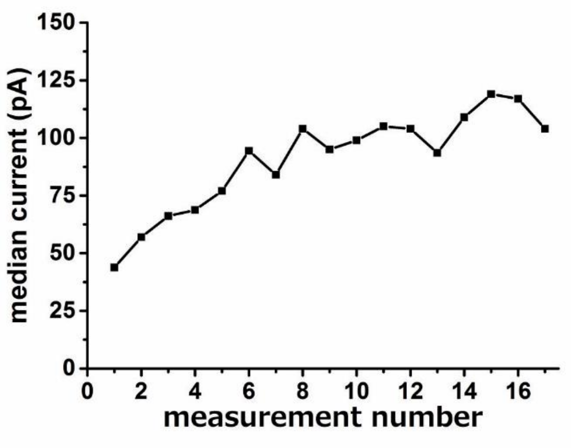

Figure 78: Development of the measured current over the course of consecutive measurements each on a new area of a UV-ozone treated TiO_2 film on a cleaned FTO substrate that has been argon-plasma treated. b) Development of the measured roughness on over the course of consecutive measurements. Each image was recorded with a setpoint force of 25 nN, a z-length of 150 nm, a pixel-time of 7 ms and an applied external bias of 2 V. Each image had a size of 5 µm x µm with a resolution of 128 x 128 pixels. Each image was measured next to the previous one with an offset of 5 µm from edge to edge.

Each image was recorded on the same substrate in different areas in order to prevent crosstalk from a local surface modification of the TiO_2. In contrast to TiO_2 films on oxygen plasma treated FTO, an increase of median current is observed with progressing cSFM measurements on a TiO_2 thin film on top of an FTO substrate. The median current plateaus at a mean median current of approximately 106 pA after 14 measurements. The roughness showed no trend with progressing measurements. An average roughness of (17.1 ±0.7) nm was measured.

The electric resistance of a TiO_2 /SnO_2 array is switchable.

This rise in current is reproducible and switchable. When conducting a set of 15 consecutive measurements with an applied bias of 2 V, I measured an increasing median current (Figure 79, first set of black dots). When conducting 3 measurements with an applied external bias of – 2V, no signal above the noise level was detected, due to the rectifying diode characteristics of the TiO_2 / FTO array (Figure 79, first three red dots). However, when applying a bias of +2 V again for the following measurements, a strongly decreased median current was recorded. The median current rose again with progressing measurements and reached almost the same level after 15 measurements as before the first switching (Figure 79, second set of black dots). The same behavior was observed for a third cycle.

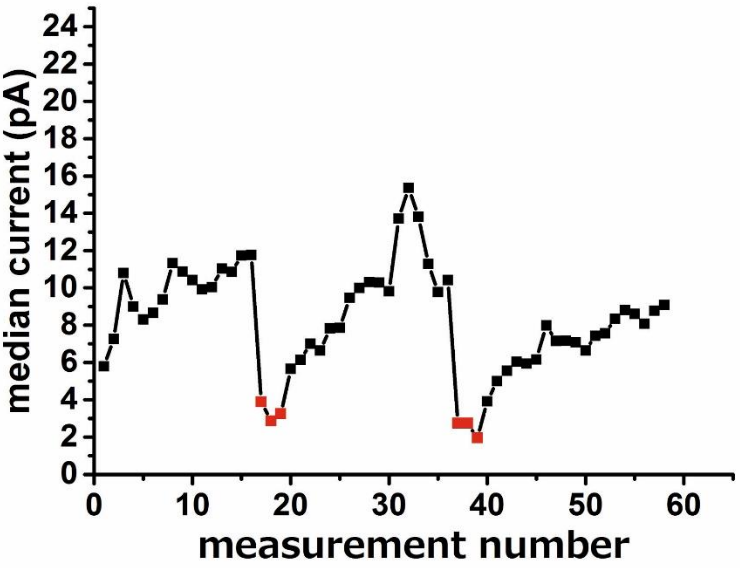

Figure 79: Development of the measured current over the course of consecutive measurements. Each image was recorded on a new area of a UV-ozone treated TiO_2 film on a cleaned FTO substrate that has been argon-plasma treated. For every 15 measurements in a row, an external bias of 2 V was applied (black dots). For the next following 3 measurements, an external bias of - 2 V was applied (red dots). The next 15 measurements again were measured with an applied bias of 2 V. Each image was recorded with a setpoint force of 25 nN, a z-length of 150 nm, a pixel-time of 7 ms and an applied external bias of 2 V. Each image had a size of 5 µm x µm with a resolution of 128 x 128 pixels. Each image was measured next to the previous one with an offset of 5 µm from edge to edge.

This increase in median current can be attributed to migrating oxygen vacancies between the two layers. Upon applying a bias of +2 V, oxygen vacancies migrate from the FTO substrate into the TiO_2 layer. These oxygen vacancies act as n-dopants within the TiO_2 crystal and thus increase the conductance of the TiO_2 thin films. Therefore, the increase of conductance is a consequence of a reduced electric resistance of the TiO_2 thin film. Upon inverting the applied potential, the oxygen vacancies migrate from the TiO_2 into the FTO. Thus, the doping concentration of the TiO_2 layer is reduced and its electric resistance increases.

Conclusion

The choice of post-cleaning treatment for the FTO substrate prior to the TiO_2 synthesis plays a crucial role in both charge transport and oxygen vacancy migration between the FTO and the TiO_2 layer. Argon plasma treatment creates an FTO surface, that enables easy oxygen vacancy migration across the FTO / TiO_2 interface. I observed a change of conductance when applying an external bias of 2 V via the cantilever tip, which is caused by oxygen vacancies migration from the FTO into the TiO_2 bulk. This migration leads to an increase of n-doping of the TiO_2 layer and thus to an increased conductance. This effect was reversible and switchable upon inverting the applied external bias. Therefore, I discovered memristive properties of an FTO / TiO_2 array that were executed with cSFM. Further research has to be conducted in order to determine the influence of applied bias, contact time and setpoint force on the migration of vacancies.

These findings demonstrate the effect of surface treatment on the properties on an array of different semiconducting metal oxides. Depending on the plasma treatment, a variety of different chemical and electrical behavior can be created for the same array of an FTO / TiO_2 interface. My experiments underline the complexity that occurs, when measuring semiconducting metal oxides with cSFM and demonstrate, that the measurement itself can alter the system when measuring semiconducting thin films. When measuring repeatedly on the same area, high currents cleave surface bridging oxygen bounds of semiconducting metal oxides like FTO and $TiO_{2.}$ This surface modification under the cantilever leads to a localized charging of the surface.
Moreover, I observed a global charging across a TiO_2 thin film on an FTO, if the FTO has been oxygen plasma cleaned. Therefore, the FTO / TiO_2 interface also affects the behavior of the TiO_2 / air interface. Furthermore, I discovered memristive properties of a simple FTO / TiO_2 array, if the FTO was argon-plasma treated. Such a memresisting array could be an easy and low-cost route for constructing future artificial neural networks.

Chapter 6: Conclusion and Outlook

Within this work, I presented a guideline for how to synthesize state-of-the-art $MAPbI_3$ based perovskite solar cells (PSC) with a record efficiency of 19.5%.

Within **chapter 2**, I elaborated the necessary key points. The $F:SnO_2$ substrate requires surface argon-plasma treatment in order to remove any occurring interface potential barrier that hinders the charge transport into the metal oxide layer. The electron transport layer needs to be hole-free for efficiently blocking photo-generated holes. Simultaneously, the electric resistance must be minimized for electrons by minimizing the layer thickness and defect engineering the surface with UV-ozone treatment. In order to achieve a reproducible film quality of the perovskite layer, the precursor solvent must be removed as fast as possible, for example with accelerated evaporation due to increased gas exchange within the spin-coater or via removal with an anti-solvent in a so-called solvent engineering process.

As I highlighted in my guideline, interfaces and the charge transport between the different layers play a critical role in perovskite solar cells. **In chapter 3**, I displayed that cSFM is indispensable for studying the interplay of the interfaces due to several reasons. In contrast to other methods as a four-point-probe measurement and terahertz measurement, cSFM measures the current flow perpendicular through a TiO_2 thin film, which is similar to the flow of charges within a working solar cell. cSFM allows to study the films on a nanoscale and thus reveal local properties that would remain obscured in averaging methods as macroscopic resistance measurements. Nevertheless, cSFM also yields statistical information with the median current and thus reduce the influence of crosstalk of the morphology affecting the current. No perovskite layer is needed to measure the effect of surface oxygen vacancies on the TiO_2 conductance.

Furthermore, I developed a measurement procedure to perform cSFM on semiconducting metal oxides and identified several critical requirements in order to obtain quantitative comparisons. The peak force based QI mode reduces lateral stress on the cantilever and thus enabled me to perform over 3 million individual force-distance curves without any significant tip erosion. I used the maximum current of the extend curve to generate the current image since the extend curve is less prone to influences by surface effects like water bridges. In order to achieve quantitatively comparable values, each sample must be measured with the same cantilever 30 min of UV-ozone treatment of the cantilever increases the measured current up to one order of magnitude compared to an untreated cantilever. Each sample must be contacted with both copper tape and silver paste in order to achieve a good and reproducible electric contact.

In **chapters 4 and 5**, I discussed several effects that have to be considered when measuring cSFM on semiconducting metal oxides as FTO and TiO_2. FTO substrates need to be argon-plasma treated to exhibit a high conducting surface. Oxygen-plasma treatment creates a thin layer of undoped SnO_2 (Figure 80 a). Surface oxygen vacancies act as electron traps and decrease the conductance perpendicular through a TiO_2 thin film. UV-ozone treatment removes surface oxygen vacancies (Figure 80 b). cSFM can cleave surface oxygen-metal bounds under the cantilever tip and thus induce a local charging (Figure 80 c). A pristine area must be recorded for each image when conducting several measurements on the same substrate. Local charging causes an additional potential barrier and reduces the measured current. Humidity quenches surface charging and thus strongly affects the cSFM measurements (Figure 80 d). However, the surface is still modified, as KPFM verified. Oxygen-plasma treatment of the FTO substrate prior to the TiO_2 film synthesis creates an undoped SnO_2 interlayer that acts as an additional potential barrier for electrons (Figure 80 e). This barrier decreases the flow of current through a perovskite solar cell as well as during a cSFM measurement. Surface oxygen vacancies promote the charge transfer parallel across the TiO_2 surface and thus cause non-local charging of the surface (Figure 80 e). Thus, each TiO_2 thin film sample must be measured only once for quantitative comparison. Bulk oxygen vacancies can migrate between the two metal oxide layers upon applying an external bias if the FTO was argon-plasma treated prior to the TiO_2 synthesis (Figure 80 f). As a result, the n-doping concentration of the TiO_2 changes with consecutive cSFM measurements and each TiO_2 thin film sample must be measured only once for quantitative comparison. Contamination of the TiO_2 surface reduces the local conductance by over 10 % after one hour of exposure to ambient conditions (Figure 80 h). Accordingly, each TiO_2 sample must be measured directly after synthesis or directly after surface treatment.

In conclusion, I demonstrated that simple UV-ozone treatment, argon-plasma, and oxygen-plasma treatment provides a valuable toolbox for engineering the surface defect properties and thus the transport properties of semiconducting metal oxide films. The choice of treatment depends on the treated surface and the desired properties. As an example, argon-plasma increases the local conductance through an FTO surface but decreases the conductance of TiO_2 thin films. However, argon plasma treatment potentially also increases the number of surface oxygen vacancies in FTO substrates. Such oxygen vacancies could act as electron traps similar to surface defects in TiO_2 surfaces. Thus, removing these surface oxygen vacancies with additional UV-ozone treatment after argon plasma treatment might even further increase the local conductance of $F:SnO_2$ films.

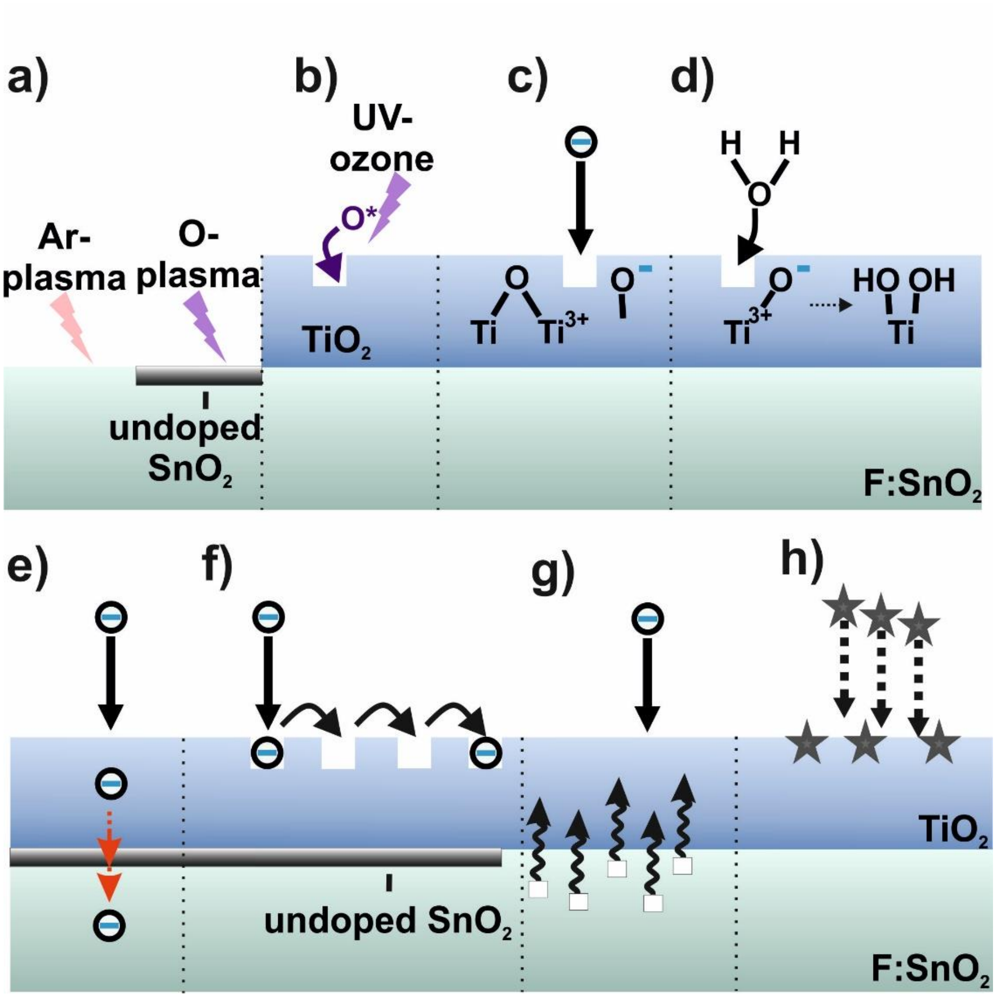

-

- *Figure 80: summary of all occurring effects when measuring the local conductance of FTO and TiO2 films with cSFM. A) Oxygen plasma treatment creates an undoped SnO_2 layer. Ar-plasma does not. b) UV-ozone treatment fills surface oxygen vacancies. c) cSFM measurement induces local charges at FTO and TiO_2 surfaces. d) recontamination decreases the measured current after 1 hour by over 10 %. e) An undoped SnO2 interlayer between the FTO and TiO2 causes an additional potential barrier. f) surface oxygen vacancies promote the electron transfer parallel across the surface. g) bulk oxygen vacancies can migrate between the two metal oxide layers.*

Moreover, oxygen vacancies act as catalytic centers at TiO_2 surfaces. Since perovskite solar cells are prone to degradation, follow up experiments could investigate, if removal of these surface catalytic centers leads to improved device stability. Additionally, the effect of UV-ozone treatment, oxygen-plasma and argon-plasma treatment on other semiconducting metal oxides such as SiO_2 or WO_3 could be investigated in a similar fashion. These surface treatments could easily be implemented as an additional low-cost step for the synthesis of any thin application that uses semiconducting metal oxides as charge transporting layers.

Further research could study the contamination over time depending on the surface treatments. I noticed, that untreated TiO_2 surfaces became hydrophobic after approximately a day which is another consequence of the adsorption of nonpolar hydrocarbons. Argon-plasma cleaned surfaces even repelled water droplets after already a few hours, which indicates faster adsorption of nonpolar molecules. In contrast, TiO_2 surfaces remained hydrophilic after UV-Ozone treatment even after one day.

cSFM induced surface modification could be a promising route to locally pattern semiconducting metal oxides on a nanoscale. My approach represents a novel route of inducing localized negative charges at a surface and add a new method to the broader context of scanning probe lithography. Negatively charged areas could exhibit a modified reactivity to surface modifications with surfactants, Grignard reagents, and other organic or inorganic molecules.

I observed, that bulk oxygen-vacancies can migrate through the FTO / TiO_2 interface. Accordingly, the number of n-dopants within the TiO_2 thin film can be changed when applying an external electric bias with a cantilever tip during a cSFM experiment. As a consequence, I demonstrated a switchable electric resistance of an $F{:}SnO_2/TiO_2$ array. This observation could lead to the development of simple and low-cost memristors, a novel class of electric elements that might be used for future processors and artificial neural networks.

References

(1) Magli, G. Sirius and the Project of the Megalithic Enclosures at Gobekli Tepe. *Nexus Netw. J.* **2016**, *18* (2), 337–346.

(2) Mohr, S. H.; Wang, J.; Ellem, G.; Ward, J.; Giurco, D. Projection of World Fossil Fuels by Country. *Fuel* **2015**, *141*, 120–135.

(3) Anderson, T. R.; Hawkins, E.; Jones, P. D. CO2, the Greenhouse Effect and Global Warming: From the Pioneering Work of Arrhenius and Callendar to Today's Earth System Models. *Endeavour* **2016**, *40* (3), 178–187.

(4) Nullis, C. WMO Greenhouse Gas Bulletin (GHG Bulletin) - No. 15: The State of Greenhouse Gases in the Atmosphere Based on Global Observations through 2018. *WMO Greenh. Gas Bull. (GHG Bull.* **2018**, *15*, 1–8.

(5) Rice, K.; Winkler, B.; Jacobs, P.; Skuce, A. G.; Cook, J.; Green, S. A.; Painting, R.; Nuccitelli, D.; Verheggen, B.; Doran, P. T.; et al. Consensus on Consensus: A Synthesis of Consensus Estimates on Human-Caused Global Warming. *Environ. Res. Lett.* **2016**, *11* (4), 048002.

(6) Nathan S. Lewis; Nocera, D. G. Powering the Planat: Chemical Challanges in Solar Energy Utilization. *PNAS* **2006**, *103* (43), 15729–15735.

(7) Battaglia, C.; Cuevas, A.; De Wolf, S. High-Efficiency Crystalline Silicon Solar Cells: Status and Perspectives. *Energy Environ. Sci.* **2016**, *9* (5), 1552–1576.

(8) Kost, C.; Schlegl, T.; Thomsen, J.; Nold, S.; Mayer, J.; Hartmann, N.; Senkpiel, C.; Philipps, S.; Lude, S.; Saad, N. Fraunhofer ISE: Levelized Cost of Electricity - Renewable Energy Technologies, March 2018. *Fraunhofer ISE Levelized Cost Electr. - Renew. Energy Technol.* **2018**, No. March.

(9) Kojima, A.; Teshima, K.; Shirai, Y.; Miyasaka, T. Organometal Halide Perovskites as Visible-Light Sensitizers for Photovoltaic Cells. *J. Am. Chem. Soc.* **2009**, *131* (17), 6050–6051.

(10) NREL Photovoltaic Research efficiency chart, accessed 20.12.2019.

(11) Green, M. A. The Path to 25% Silicon Solar Cell Efficiency: History of Silicon Cell Evolution. *Prog. Photovoltaics Res. Appl.* **2009**, *17* (3), 183–189.

(12) Hwang, K.; Jung, Y. S.; Heo, Y. J.; Scholes, F. H.; Watkins, S. E.; Subbiah, J.; Jones, D. J.; Kim, D. Y.; Vak, D. Toward Large Scale Roll-to-Roll Production of Fully Printed Perovskite Solar Cells. *Adv. Mater.* **2015**, *27* (7), 1241–1247.

(13) Petrus, M. L.; Schlipf, J.; Li, C.; Gujar, T. P.; Giesbrecht, N.; Müller-Buschbaum, P.; Thelakkat, M.; Bein, T.; Hüttner, S.; Docampo, P. Capturing the Sun: A Review of the Challenges and Perspectives of Perovskite Solar Cells. *Adv. Energy Mater.* **2017**, *1700264*, 1700264.

(14) Wu, M.; Haji Ladi, N.; Yi, Z.; Li, H.; Shen, Y.; Wang, M. Stability Issue of Perovskite Solar Cells under Real-World Operating Conditions. *Energy Technol.* **2019**, *1900744*, 1–12.

(15) Schulz, P.; Cahen, D.; Kahn, A. Halide Perovskites: Is It All about the Interfaces? *Chem. Rev.* **2019**, *119* (5), 3349–3417.

(16) Bergmann, V. W.; Guo, Y.; Tanaka, H.; Hermes, I. M.; Li, D.; Klasen, A.; Bretschneider, S. A.; Nakamura, E.; Berger, R.; Weber, S. A. L. Local Time-Dependent Charging in a Perovskite Solar Cell. *ACS Appl. Mater. Interfaces* **2016**, *8* (30), 19402–19409.

(17) Weber, S. A. L.; Hermes, I. M.; Turren-Cruz, S. H.; Gort, C.; Bergmann, V. W.; Gilson, L.; Hagfeldt, A.; Graetzel, M.; Tress, W.; Berger, R. How the Formation of Interfacial Charge Causes Hysteresis in Perovskite Solar Cells. *Energy Environ. Sci.* **2018**, *11* (9), 2404–2413.

(18) Kojima, A.; Teshima, K.; Shirai, Y.; Miyasaka, T. Organometal Halide Perovskites as Visible-Light Sensitizers for Photovoltaic Cells. *J. Am. Chem. Soc.* **2009**, *131* (17), 6050–6051.

(19) Ansari, M. I. H.; Qurashi, A.; Nazeeruddin, M. K. Frontiers, Opportunities, and Challenges in Perovskite Solar Cells: A Critical Review. *J. Photochem. Photobiol. C Photochem. Rev.* **2018**, *35*, 1–24.

(20) https://www.finanzen.net/rohstoffe https://www.finanzen.net/rohstoffe.

(21) Honsberg, C.; Bowden Stuart. www.PVeducation.com, accessed 20.12.2019.

(22) Shockley, W.; Queisser, H. J. Detailed Balance Limit of Efficiency of P-n Junction Solar Cells. *J. Appl. Phys.* **1961**, *32* (3), 510–519.

(23) Wu, N.; Wu, Y.; Walter, D.; Shen, H.; Duong, T.; Grant, D.; Barugkin, C.; Fu, X.; Peng, J.; White, T.; et al. Identifying the Cause of Voltage and Fill Factor Losses in Perovskite Solar Cells by Using Luminescence Measurements. *Energy Technol.* **2017**, *5* (10), 1827–1835.

(24) Leijtens, T.; Eperon, G. E.; Barker, A. J.; Grancini, G.; Zhang, W.; Ball, J. M.; Kandada, A. R. S.; Snaith, H. J.; Petrozza, A. Carrier Trapping and Recombination: The Role of Defect Physics in Enhancing the Open Circuit Voltage of Metal Halide Perovskite Solar Cells. *Energy Environ. Sci.* **2016**, *9* (11), 3472–3481.

(25) Li, D.; Bretschneider, S. A.; Bergmann, V. W.; Hermes, I. M.; Mars, J.; Klasen, A.; Lu, H.; Tremel, W.; Mezger, M.; Butt, H. J.; et al. Humidity-Induced Grain Boundaries in MAPbI3 Perovskite Films. *J. Phys. Chem. C* **2016**, *120* (12), 6363–6368.

(26) Ravichandran, K.; Jabena Begum, N.; Swaminathan, K.; Sakthivel, B. Fabrication of a Double Layered FTO/AZO Film Structure Having Enhanced Thermal, Electrical and Optical Properties, as a Substitute for ITO Films. *Superlattices Microstruct.* **2013**, *64*, 185–195.

(27) Kim, Y. N.; Shin, H. G.; Song, J. K.; Cho, D. H.; Lee, H. S.; Jung, Y. G. Thermal Degradation Behavior of Indium Tin Oxide Thin Films Deposited by Radio Frequency Magnetron Sputtering. *J. Mater. Res.* **2005**, *20* (6), 1574–1579.

(28) Product Specification. *Build. Res. Inf.* **1993**, *21* (1), 21–22.

(29) Riedel, E.; Janiak, C. *Allgemeine Und Anorganische Chemie*; DE GRUYTER: Berlin, New York, 2011.

(30) Jeon, N. J.; Lee, H. G.; Kim, Y. C.; Seo, J.; Noh, J. H.; Lee, J.; Seok, S. Il. O-Methoxy Substituents in Spiro-OMeTAD for Efficient Inorganic-Organic Hybrid Perovskite Solar Cells. *J. Am. Chem. Soc.* **2014**, *136* (22), 7837–7840.

(31) Zhang, F.; Liu, X.; Yi, C.; Bi, D.; Luo, J.; Wang, S.; Li, X.; Xiao, Y.; Zakeeruddin, S. M.; Grätzel, M. Dopant-Free Donor (D)–π–D–π–D Conjugated Hole-Transport Materials for Efficient and Stable Perovskite Solar Cells. *ChemSusChem* **2016**, *9* (18), 2578–2585.

(32) Dong, Q.; Fang, Y.; Shao, Y.; Mulligan, P.; Qiu, J.; Cao, L.; Huang, J. Electron-Hole Diffusion Lengths > 175 Mm in Solution-Grown CH3NH3PbI3 Single Crystals. *Science (80-.).* **2015**, *347* (6225), 967–970.

(33) Singh, T.; Singh, J.; Miyasaka, T. Role of Metal Oxide Electron-Transport Layer Modification on the Stability of High Performing Perovskite Solar Cells. *ChemSusChem* **2016**, *9* (18), 2559–2566.

(34) Zhang, P.; Wu, J.; Zhang, T.; Wang, Y.; Liu, D.; Chen, H.; Ji, L.; Liu, C.; Ahmad, W.; Chen, Z. D.; et al. Perovskite Solar Cells with ZnO Electron-Transporting Materials. *Adv. Mater.* **2018**, *30* (3), 1–20.

(35) You, J.; Meng, L.; Song, T.-B.; Guo, T.-F.; Yang, Y. (Michael); Chang, W.-H.; Hong, Z.; Chen, H.; Zhou, H.; Chen, Q.; et al. Improved Air Stability of Perovskite Solar Cells via Solution-Processed Metal Oxide Transport Layers. *Nat. Nanotechnol.* **2015**, *11*, 1–8.

(36) Dong, X.; Hu, H.; Lin, B.; Ding, J.; Yuan, N. The Effect of ALD-Zno Layers on the Formation of $CH_3NH_3PbI_3$ with Different Perovskite Precursors and Sintering Temperatures. *Chem. Commun.* **2014**, *50* (92), 14405–14408.

(37) Green, M. A.; Hishikawa, Y.; Dunlop, E. D.; Levi, D. H.; Hohl-Ebinger, J.; Yoshita, M.; Ho-Baillie, A. W. Y. Solar Cell Efficiency Tables (Version 53). *Prog. Photovoltaics Res. Appl.* **2018**, *27* (1), 3–12.

(38) Diebold, U. The Surface Science of Titanium Dioxide. *Surf. Sci. Rep.* **2003**, *48* (5–8), 53–229.

(39) Scanlon, D. O.; Dunnill, C. W.; Buckeridge, J.; Shevlin, S. A.; Logsdail, A. J.; Woodley, S. M.; Catlow, C. R. A.; Powell, M. J.; Palgrave, R. G.; Parkin, I. P.; et al. Band Alignment of Rutile and Anatase TiO2. *Nat. Mater.* **2013**, *12* (9), 798–801.

(40) Tang, H.; Prasad, K.; Sanjinès, R.; Schmid, P. E.; Lévy, F. Electrical and Optical Properties of TiO2 Anatase Thin Films. *J. Appl. Phys.* **1994**, *75* (4), 2042–2047.

(41) Rafieian, D.; Ogieglo, W.; Savenije, T.; Lammertink, R. G. H. Controlled Formation of Anatase and Rutile TiO2 Thin Films by Reactive Magnetron Sputtering. *AIP Adv.* **2015**, *5* (9), 097168.

(42) Zhu, T.; Gao, S. P. The Stability, Electronic Structure, and Optical Property of Tio2polymorphs. *J. Phys. Chem. C* **2014**, *118* (21), 11385–11396.

(43) Huang, A.; Zhu, J.; Zhou, Y.; Yu, Y.; Liu, Y.; Yang, S.; Ji, S.; Lei, L.; Jin, P. One Step Spray-Coated TiO2 Electron-Transport Layers for Decent Perovskite Solar Cells on Large and Flexible Substrates. *Nanotechnology* **2017**, *28* (1).

(44) Liang, C.; Wu, Z.; Li, P.; Fan, J.; Zhang, Y.; Shao, G. Chemical Bath Deposited Rutile TiO

2 Compact Layer toward Efficient Planar Heterojunction Perovskite Solar Cells. *Appl. Surf. Sci.* **2017**, *391*, 337–344.

(45) Mali, S. S.; Hong, C. K.; Inamdar, A. I.; Im, H.; Shim, S. E. Efficient Planar N-i-p Type Heterojunction Flexible Perovskite Solar Cells with Sputtered TiO 2 Electron Transporting Layers. *Nanoscale* **2017**, *9* (9), 3095–3104.

(46) Bergmann, V. W.; Weber, S. A. L.; Javier Ramos, F.; Nazeeruddin, M. K.; Grätzel, M.; Li, D.; Domanski, A. L.; Lieberwirth, I.; Ahmad, S.; Berger, R. Real-Space Observation of Unbalanced Charge Distribution inside a Perovskite-Sensitized Solar Cell. *Nat. Commun.* **2014**, *5* (SEPTEMBER 2014), 5001.

(47) Bahbou, M. F.; Nylén, P.; Wigren, J. Effect of Grit Blasting and Spraying Angle on the Adhesion Strength of a Plasma-Sprayed Coating. *J. Therm. Spray Technol.* **2004**, *13* (4), 508–514.

(48) Ilavsky, J.; Allen, A. J.; Long, G. G.; Krueger, S.; Berndt, C. C.; Herman, H. Influence of Spray Angle on the Pore and Crack Microstructure of Plasma-Sprayed Deposits. *J. Am. Ceram. Soc.* **1997**, *80* (3), 733–742.

(49) Chadha, S.; Jefferson-Loveday, R.; Hussain, T. Effect of Nozzle Geometry on the Gas Dynamics and Evaporation Rates of Suspension High Velocity Oxy Fuel (SHVOF) Thermal Spray: A Numerical Investigation. *Surf. Coatings Technol.* **2019**, *371* (March 2018), 78–89.

(50) Toma, S. L.; Bejinariu, C.; Baciu, R.; Radu, S. The Effect of Frontal Nozzle Geometry and Gas Pressure on the Steel Coating Properties Obtained by Wire Arc Spraying. *Surf. Coatings Technol.* **2013**, *220*, 266–270.

(51) Liang, C.; Wu, Z.; Li, P.; Fan, J.; Zhang, Y.; Shao, G. Chemical Bath Deposited Rutile TiO2 Compact Layer toward Efficient Planar Heterojunction Perovskite Solar Cells. *Appl. Surf. Sci.* **2017**, *391*, 337–344.

(52) Klasen, A.; Baumli, P.; Sheng, Q.; Johannes, E.; Bretschneider, S. A.; Hermes, I. M.; Bergmann, V. W.; Gort, C.; Axt, A.; Weber, S. A. L.; et al. Removal of Surface Oxygen Vacancies Increases Conductance Through TiO2 Thin Films for Perovskite Solar Cells. *J. Phys. Chem. C* **2019**, *123* (22), 13458–13466.

(53) Liu, C.; Wang, K.; Du, P.; Meng, T.; Yu, X.; Cheng, S. Z. D.; Gong, X. High Performance Planar Heterojunction Perovskite Solar Cells with Fullerene Derivatives as the Electron Transport Layer. *ACS Appl. Mater. Interfaces* **2015**, *7*, 1153–1159.

(54) Leijtens, T.; Lim, J.; Teuscher, J.; Park, T.; Snaith, H. J. Charge Density Dependent Mobility of Organic Hole-Transporters and Mesoporous TiO2 Determined by Transient Mobility Spectroscopy: Implications to Dye-Sensitized and Organic Solar Cells. *Adv. Mater.* **2013**, *25* (23), 3227–3233.

(55) Ohara, T.; Matsumoto, Y.; Ohashi, H. The Film Formation Dynamics in Spin Coating. *Phys. Fluids A* **1989**, *1* (12), 1949–1959.

(56) Wang, F.; Shimazaki, A.; Yang, F.; Kanahashi, K.; Matsuki, K.; Miyauchi, Y.; Takenobu, T.; Wakamiya, A.; Murata, Y.; Matsuda, K. Highly Efficient and Stable Perovskite Solar Cells by Interfacial Engineering Using Solution-Processed Polymer Layer. *J. Phys.*

Chem. C **2017**, *121* (3), 1562–1568.

(57) Jena, A. K.; Chen, H.-W.; Kogo, A.; Sanehira, Y.; Ikegami, M.; Miyasaka, T. The Interface between FTO and the TiO2 Compact Layer Can Be One of the Origins to Hysteresis in Planar Heterojunction Perovskite Solar Cells. *ACS Appl. Mater. Interfaces* **2015**, *7* (18), 9817–9823.

(58) Jeong, I.; Park, Y. H.; Bae, S.; Park, M.; Jeong, H.; Lee, P.; Ko, M. J. Solution-Processed Ultrathin TiO2 Compact Layer Hybridized with Mesoporous TiO2 for High-Performance Perovskite Solar Cells. *ACS Appl. Mater. Interfaces* **2017**, *9* (42), 36865–36874.

(59) Giordano, F.; Abate, A.; Pablo, J.; Baena, C.; Saliba, M.; Matsui, T.; Im, S. H.; Zakeeruddin, S. M.; Nazeeruddin, M. K.; Hagfeldt, A.; et al. Enhanced Electronic Properties in Mesoporous TiO2 via Lithium Doping for High-Efficiency Perovskite Solar Cells. *Nat. Commun.* **2016**, *7*, 1–6.

(60) Alcocer, M. J. P.; Leijtens, T.; Herz, L. M.; Petrozza, A.; Snaith, H. J. Electron-Hole Diffusion Lengths Exceeding 1 Micrometer in an Organometal Trihalide Perovskite Absorber. *Science* **2014**, *342* (2013), 341–344.

(61) Dong, Q.; Fang, Y.; Shao, Y.; Mulligan, P.; Qiu, J.; Cao, L.; Huang, J. Electron-Hole Diffusion Lengths > 175 m m in Solution-Grown CH 3 NH 3 PbI 3 Single Crystals. *Science (80-.).* **2015**, *347* (6225), 967–970.

(62) Sun, S.; Salim, T.; Mathews, N.; Duchamp, M.; Boothroyd, C.; Xing, G.; Sum, T. C.; Lam, Y. M. The Origin of High Efficiency in Low-Temperature Solution-Processable Bilayer Organometal Halide Hybrid Solar Cells. *Energy Environ. Sci.* **2014**, *7* (1), 399.

(63) Lin, Q.; Armin, A.; Chandra, R.; Nagiri, R.; Burn, P. L.; Meredith, P. Electro-Optics of Perovskite Solar Cells. *Nat. Photonics* **2014**, *9* (2), 106–112.

(64) Jung, H. S.; Park, N. G. Perovskite Solar Cells: From Materials to Devices. *Small* **2015**, *11* (1), 10–25.

(65) Dong, Q.; Fang, Y.; Shao, Y.; Mulligan, P.; Qiu, J.; Cao, L.; Huang, J. Electron-Hole Diffusion Lengths > 175 Mm in Solution-Grown CH3NH3PbI3 Single Crystals. *Science (80-.).* **2015**, *347* (6225), 967–970.

(66) Jeon, N. J.; Noh, J. H.; Kim, Y. C.; Yang, W. S.; Ryu, S.; Seok, S. Il. Solvent Engineering for High-Performance Inorganic–Organic Hybrid Perovskite Solar Cells. *Nat Mater* **2014**, *13* (9), 897–903.

(67) Das, S.; Yang, B.; Gu, G.; Joshi, P. C.; Ivanov, I. N.; Rouleau, C. M.; Aytug, T.; Geohegan, D. B.; Xiao, K. High-Performance Flexible Perovskite Solar Cells by Using a Combination of Ultrasonic Spray-Coating and Low Thermal Budget Photonic Curing. *ACS Photonics* **2015**, *2* (6), 680–686.

(68) Yi, C.; Li, X.; Luo, J.; Zakeeruddin, S. M.; Grätzel, M. Perovskite Photovoltaics with Outstanding Performance Produced by Chemical Conversion of Bilayer Mesostructured Lead Halide/TiO2 Films. *Adv. Mater.* **2016**, *28* (15), 2964–2970.

(69) Gardner, K. L.; Tait, J. G.; Merckx, T.; Qiu, W.; Paetzold, U. W.; Kootstra, L.; Jaysankar, M.; Gehlhaar, R.; Cheyns, D.; Heremans, P.; et al. Nonhazardous Solvent Systems for

Processing Perovskite Photovoltaics. *Adv. Energy Mater.* **2016**, *6* (14), 1–8.

(70) Xiao, J.; Shi, J.; Li, D.; Meng, Q. Perovskite Thin-Film Solar Cell: Excitation in Photovoltaic Science. *Sci. China Chem.* **2015**, *58* (2), 221–238.

(71) Li, C.; Lu, X.; Ding, W.; Feng, L.; Gao, Y.; Guo, Z. Formability of ABX 3 (X = F, Cl, Br, I) Halide Perovskites. *Acta Crystallogr. Sect. B Struct. Sci.* **2008**, *64* (6), 702–707.

(72) RINGWOOD, A. E. The Principles Governing Trace Element Distribution during Magmatic Crystallization Part I: The Influence of Electronegativity. *Geochim. Cosmochim. Acta* **1955**, *7* (3–4), 189–202.

(73) Ma, F.; Li, J.; Li, W.; Lin, N.; Wang, L.; Qiao, J. Stable α/δ Phase Junction of Formamidinium Lead Iodide Perovskites for Enhanced near-Infrared Emission. *Chem. Sci.* **2017**, *8* (1), 800–805.

(74) Niemann, R. G.; Gouda, L.; Hu, J.; Tirosh, S.; Gottesman, R.; Cameron, P. J.; Zaban, A. Cs+ Incorporation into CH3NH3PbI3 Perovskite: Substitution Limit and Stability Enhancement. *J. Mater. Chem. A* **2016**, *4* (45), 17819–17827.

(75) Saliba, M.; Matsui, T.; Domanski, K.; Seo, J.-Y.; Ummadisingu, A.; Zakeeruddin, S. M.; Correa-Baena, J.-P.; Tress, W. R.; Abate, A.; Hagfeldt, A.; et al. Incorporation of Rubidium Cations into Perovskite Solar Cells Improves Photovoltaic Performance. *Science (80-.).* **2016**, *354* (6309), 206–209.

(76) Hong, F.; Saparov, B.; Meng, W.; Xiao, Z.; Mitzi, D. B.; Yan, Y. Viability of Lead-Free Perovskites with Mixed Chalcogen and Halogen Anions for Photovoltaic Applications. *J. Phys. Chem. C* **2016**, *120* (12), 6435–6441.

(77) Jacobsson, T. J.; Pazoki, M.; Hagfeldt, A.; Edvinsson, T. Goldschmidt Rules and Strontium Replacement in Lead Halogen Perovskite Solar Cells: Theory and Preliminary Experiments on CH3NH3SrI3. *J. Phys. Chem. C* **2015**, *119* (46), 25673–25683.

(78) Wang, K.; Liang, Z.; Wang, X.; Cui, X. Lead Replacement in CH3NH3PbI3 Perovskites. *Adv. Electron. Mater.* **2015**, *1* (10), 1500089.

(79) Boix, P. P.; Agarwala, S.; Koh, T. M.; Mathews, N.; Mhaisalkar, S. G. Perovskite Solar Cells: Beyond Methylammonium Lead Iodide. *J. Phys. Chem. Lett.* **2015**, *6* (5), 898–907.

(80) Hoefler, S. F.; Trimmel, G.; Rath, T. Progress on Lead-Free Metal Halide Perovskites for Photovoltaic Applications: A Review. *Monatshefte für Chemie - Chem. Mon.* **2017**, *148* (5), 795–826.

(81) Correa-Baena, J.-P.; Abate, A.; Saliba, M.; Tress, W.; Jesper Jacobsson, T.; Grätzel, M.; Hagfeldt, A. The Rapid Evolution of Highly Efficient Perovskite Solar Cells. *Energy Environ. Sci.* **2017**, *10*, 710–727.

(82) Chen, B.; Yu, Z.; Liu, K.; Zheng, X.; Liu, Y.; Shi, J.; Spronk, D.; Rudd, P. N.; Holman, Z.; Huang, J. Grain Engineering for Perovskite/Silicon Monolithic Tandem Solar Cells with Efficiency of 25.4%. *Joule* **2019**, *3* (1), 177–190.

(83) Jung, K.-H.; Seo, J.-Y.; Lee, S.; Shin, H.; Park, N.-G. Solution-Processed SnO2 Thin Film

for Hysteresis-Less 19.2% Planar Perovskite Solar Cell. *J. Mater. Chem. A* **2017**, 24790–24803.

(84) Xiao, Z.; Dong, Q.; Bi, C.; Shao, Y.; Yuan, Y.; Huang, J. Solvent Annealing of Perovskite-Induced Crystal Growth for Photovoltaic-Device Efficiency Enhancement. *Adv. Mater.* **2014**, *26* (37), 6503–6509.

(85) Jeon, N. J.; Noh, J. H.; Kim, Y. C.; Yang, W. S.; Ryu, S.; Seok, S. Il. Solvent Engineering for High-Performance Inorganic–Organic Hybrid Perovskite Solar Cells. *Nat Mater* **2014**, *13* (9), 897–903.

(86) Lee, J.-W.; Park, N.-G. Two-Step Deposition Method for High-Efficiency Perovskite Solar Cells. *MRS Bull.* **2015**, *40* (August), 654.

(87) Schlipf, J.; Docampo, P.; Schaffer, C. J.; Körstgens, V.; Bießmann, L.; Hanusch, F.; Giesbrecht, N.; Bernstorff, S.; Bein, T.; Müller-Buschbaum, P. A Closer Look into Two-Step Perovskite Conversion with X-Ray Scattering. *J. Phys. Chem. Lett.* **2015**, *6* (7), 1265–1269.

(88) Li, X.; Bi, D.; Yi, C.; Decoppet, J.-D.; Luo, J.; Zakeeruddin, S. M.; Hagfeldt, A.; Gratzel, M. A Vacuum Flash-Assisted Solution Process for High-Efficiency Large-Area Perovskite Solar Cells. *Science (80-.).* **2016**, *353* (6294), 58–62.

(89) Peng, Y.; Jing, G.; Cui, T. High Performance Perovskite Solar Cells through Vapor Deposition with Optimized PbI2 Precursor Films. *RSC Adv.* **2015**, *5*, 95847–95853.

(90) Chen, C. W.; Kang, H. W.; Hsiao, S. Y.; Yang, P. F.; Chiang, K. M.; Lin, H. W. Efficient and Uniform Planar-Type Perovskite Solar Cells by Simple Sequential Vacuum Deposition. *Adv. Mater.* **2014**, 6647–6652.

(91) Klasen, A. Synthese von Perowskit- Dünnschichten Für Solarzellen, JGU Mainz, 2015.

(92) Kang, R.; Kim, J. E.; Yeo, J. S.; Lee, S.; Jeon, Y. J.; Kim, D. Y. Optimized Organometal Halide Perovskite Planar Hybrid Solar Cells via Control of Solvent Evaporation Rate. *J. Phys. Chem. C* **2014**, *118* (46), 26513–26520.

(93) Yang, W. S.; Park, B.-W.; Jung, E. H.; Jeon, N. J.; Kim, Y. C.; Lee, D. U.; Shin, S. S.; Seo, J.; Kim, E. K.; Noh, J. H.; et al. Iodide Management in Formamidinium-Lead-Halide–Based Perovskite Layers for Efficient Solar Cells. *Science (80-.).* **2017**, *356* (6345), 1376–1379.

(94) Saliba, M.; Correa-Baena, J. P.; Wolff, C. M.; Stolterfoht, M.; Phung, N.; Albrecht, S.; Neher, D.; Abate, A. How to Make over 20% Efficient Perovskite Solar Cells in Regular (n-i-p) and Inverted (p-i-n) Architectures. *Chem. Mater.* **2018**, *30* (13), 4193–4201.

(95) Ahn, N.; Son, D. Y.; Jang, I. H.; Kang, S. M.; Choi, M.; Park, N. G. Highly Reproducible Perovskite Solar Cells with Average Efficiency of 18.3% and Best Efficiency of 19.7% Fabricated via Lewis Base Adduct of Lead(II) Iodide. *J. Am. Chem. Soc.* **2015**, *137* (27), 8696–8699.

(96) Xu, M. F.; Zhang, H.; Zhang, S.; Zhu, H. L.; Su, H. M.; Liu, J.; Wong, K. S.; Liao, L. S.; Choy, W. C. H. A Low Temperature Gradual Annealing Scheme for Achieving High Performance Perovskite Solar Cells with No Hysteresis. *J. Mater. Chem. A* **2015**, *3* (27), 14424–14430.

(97) Saliba, M.; Matsui, T.; Seo, J.-Y.; Domanski, K.; Correa-Baena, J.-P.; Nazeeruddin, M. K.; Zakeeruddin, S. M.; Tress, W.; Abate, A.; Hagfeldt, A.; et al. Cesium-Containing Triple Cation Perovskite Solar Cells: Improved Stability, Reproducibility and High Efficiency. *Energy Environ. Sci.* **2016**, *9* (6), 1989–1997.

(98) Cho, K. T.; Paek, S.; Grancini, G.; Roldán-Carmona, C.; Gao, P.; Lee, Y.; Nazeeruddin, M. K. Highly Efficient Perovskite Solar Cells with a Compositionally Engineered Perovskite/Hole Transporting Material Interface. *Energy Environ. Sci.* **2017**, *10* (2), 621–627.

(99) Yu, H.; Lee, J. W.; Yun, J.; Lee, K.; Ryu, J.; Lee, J.; Hwang, D.; Kim, S. K.; Jang, J. Outstanding Performance of Hole-Blocking Layer-Free Perovskite Solar Cell Using Hierarchically Porous Fluorine-Doped Tin Oxide Substrate. *Adv. Energy Mater.* **2017**, *1700749*, 1–9.

(100) Vivo, P.; Salunke, J. K.; Priimagi, A. Hole-Transporting Materials for Printable Perovskite Solar Cells. *Materials (Basel).* **2017**, *10* (9), 1–45.

(101) Snaith, H. J.; Grätzel, M. Enhanced Charge Mobility in a Molecular Hole Transporter via Addition of Redox Inactive Ionic Dopant: Implication to Dye-Sensitized Solar Cells. *Appl. Phys. Lett.* **2006**, *89* (26).

(102) Schölin, R.; Karlsson, M. H.; Eriksson, S. K.; Siegbahn, H.; Johansson, E. M. J.; Rensmo, H. Energy Level Shifts in Spiro-OMeTAD Molecular Thin Films When Adding Li-TFSI. *J. Phys. Chem. C* **2012**, *116* (50), 26300–26305.

(103) Malinauskas, T.; Tomkute-Luksiene, D.; Sens, R.; Daskeviciene, M.; Send, R.; Wonneberger, H.; Jankauskas, V.; Bruder, I.; Getautis, V. Enhancing Thermal Stability and Lifetime of Solid-State Dye-Sensitized Solar Cells via Molecular Engineering of the Hole-Transporting Material Spiro-OMeTAD. *ACS Appl. Mater. Interfaces* **2015**, *7* (21), 11107–11116.

(104) Lee, J.; Park, N. Chemical Approaches for Stabilizing Perovskite Solar Cells. *Adv. Energy Mater.* **2019**, *1903249*, 1–21.

(105) Li, Z.; Xiao, C.; Yang, Y.; Harvey, S. P.; Kim, D. H.; Christians, J. A.; Yang, M.; Schulz, P.; Nanayakkara, S. U.; Jiang, C. S.; et al. Extrinsic Ion Migration in Perovskite Solar Cells. *Energy Environ. Sci.* **2017**, *10* (5), 1234–1242.

(106) Jeon, N. J.; Na, H.; Jung, E. H.; Yang, T. Y.; Lee, Y. G.; Kim, G.; Shin, H. W.; Il Seok, S.; Lee, J.; Seo, J. A Fluorene-Terminated Hole-Transporting Material for Highly Efficient and Stable Perovskite Solar Cells. *Nat. Energy* **2018**, *3* (8), 682–689.

(107) Christians, J. A.; Schulz, P.; Tinkham, J. S.; Schloemer, T. H.; Harvey, S. P.; Tremolet De Villers, B. J.; Sellinger, A.; Berry, J. J.; Luther, J. M. Tailored Interfaces of Unencapsulated Perovskite Solar Cells for >1,000 Hour Operational Stability. *Nat. Energy* **2018**, *3* (1), 68–74.

(108) Seo, J. Y.; Kim, H. S.; Akin, S.; Stojanovic, M.; Simon, E.; Fleischer, M.; Hagfeldt, A.; Zakeeruddin, S. M.; Grätzel, M. Novel P-Dopant toward Highly Efficient and Stable Perovskite Solar Cells. *Energy Environ. Sci.* **2018**, *11* (10), 2985–2992.

(109) Krantz, J.; Stubhan, T.; Richter, M.; Spallek, S.; Litzov, I.; Matt, G. J.; Spiecker, E.;

Brabec, C. J. Spray-Coated Silver Nanowires as Top Electrode Layer in Semitransparent P3HT:PCBM-Based Organic Solar Cell Devices. *Adv. Funct. Mater.* **2013**, *23* (13), 1711–1717.

(110) Behrouznejad, F.; Shahbazi, S.; Taghavinia, N.; Wu, H.-P.; Diau, E. W.-G. A Study on Utilizing Different Metals as the Back Contact of CH3NH3PbI3 Perovskite Solar Cells. *J. Mater. Chem. A* **2016**, *00*, 1–11.

(111) Domanski, K.; Correa-Baena, J. P.; Mine, N.; Nazeeruddin, M. K.; Abate, A.; Saliba, M.; Tress, W.; Hagfeldt, A.; Grätzel, M. Not All That Glitters Is Gold: Metal-Migration-Induced Degradation in Perovskite Solar Cells. *ACS Nano* **2016**, *10* (6), 6306–6314.

(112) Yavari, M.; Mazloum-Ardakani, M.; Gholipour, S.; Marinova, N.; Delgado, J. L.; Turren-Cruz, S.-H.; Domanski, K.; Taghavinia, N.; Saliba, M.; Grätzel, M.; et al. Carbon Nanoparticles in High-Performance Perovskite Solar Cells. *Adv. Energy Mater.* **2018**, *1702719*, 1702719.

(113) Sharma, A.; Untch, M.; Quinton, J. S.; Berger, R.; Andersson, G.; Lewis, D. A. Nanoscale Heterogeniety and Workfunction Variations in ZnO Thin Films. *Appl. Surf. Sci.* **2016**, *363*, 516–521.

(114) Johannes, E. Local Conductivity of Compact Titanium Dioxide and Its Influence on Hybrid Perovskite Solar Cells, Mainz, 2017.

(115) Sacha, G. M.; Verdaguer, A.; Salmeron, M. Induced Water Condensation and Bridge Formation by Electric Fields in Atomic Force Microscopy. *J. Phys. Chem. B* **2006**, *110* (30), 14870–14873.

(116) García, R.; Calleja, M.; Pérez-Murano, F. Local Oxidation of Silicon Surfaces by Dynamic Force Microscopy: Nanofabrication and Water Bridge Formation. *Appl. Phys. Lett.* **1998**, *72* (18), 2295–2297.

(117) Helander, M. G.; Greiner, M. T.; Wang, Z. B.; Tang, W. M.; Lu, Z. H. Work Function of Fluorine Doped Tin Oxide. *J. Vac. Sci. Technol. A Vacuum, Surfaces, Film.* **2011**, *29* (1), 011019.

(118) Tung, R. T. Formation of an Electric Dipole at Metal-Semiconductor Interfaces. *Phys. Rev. B - Condens. Matter Mater. Phys.* **2001**, *64* (20), 1–15.

(119) Bardeen, J. Surface States and Rectification at a Metal Semi-Conductor Contact. *Phys. Rev.* **1947**, *71* (10), 717–727.

(120) Chong, H. Y.; Kim, T. W. Electrical Characteristics of Thin-Film Transistors Fabricated Utilizing a UV/Ozone-Treated TiO2 Channel Layer. *J. Electron. Mater.* **2012**, *42* (3), 398–402.

(121) Wang, G.; Wang, H.; Ling, Y.; Tang, Y.; Yang, X.; Fitzmorris, R. C.; Wang, C.; Zhang, J. Z.; Li, Y. Hydrogen-Treated TiO $_2$ Nanowire Arrays for Photoelectrochemical Water Splitting. *Nano Lett.* **2011**, *11* (7), 3026–3033.

(122) Park, K. H.; Dhayal, M. High Efficiency Solar Cell Based on Dye Sensitized Plasma Treated Nano-Structured TiO2 Films. *Electrochem. commun.* **2009**, *11* (1), 75–79.

(123) Lacasa, J. S.; Almonte, L.; Colchero, J. In Situ Characterization of Nanoscale

Contaminations Adsorbed in Air Using Atomic Force Microscopy. *Beilstein J. Nanotechnol.* **2018**, *9* (1), 2925–2935.

(124) Van Acker, K.; Vercammen, K. Abrasive Wear by TiO2 Particles on Hard and on Low Friction Coatings. *Wear* **2004**, *256* (3–4), 353–361.

(125) Hu, W.; Wan, L.; Liu, X.; Li, Q.; Wang, Z. Effect of TiO 2 /Al 2 O 3 Film Coated Diamond Abrasive Particles by Sol-Gel Technique. *Appl. Surf. Sci.* **2011**, *257* (13), 5777–5783.

(126) Butt, H. J.; Kappl, M. *Surface and Interfacial Forces*; 2010.

(127) Butt, H.; Graf, K.; Kappl, M. *Physics and Chemistry of Interfaces WILEY-VCH GmbH & Co . KGaA*; 2003.

(128) Lüth, H. *Solid Surfaces, Interfaces and Thin Films*; Graduate Texts in Physics; Springer International Publishing: Cham, 2015.

(129) Knorr, F. J.; Zhang, D.; McHale, J. L. Influence of TiCL4 Treatment on Surface Defect Photoluminescence in Pure and Mixed-Phase Nanocrystalline TiO2. *Langmuir* **2007**, *23* (17), 8686–8690.

(130) Rahman, M. A.; Bazargan, S.; Srivastava, S.; Wang, X.; Abd-Ellah, M.; Thomas, J. P.; Heinig, N. F.; Pradhan, D.; Leung, K. T. Defect-Rich Decorated TiO2 Nanowires for Super-Efficient Photoelectrochemical Water Splitting Driven by Visible Light. *Energy Environ. Sci.* **2015**, *8* (11), 3363–3373.

(131) Bharti, B.; Kumar, S.; Lee, H. N.; Kumar, R. Formation of Oxygen Vacancies and Ti3+ State in TiO2 Thin Film and Enhanced Optical Properties by Air Plasma Treatment. *Sci. Rep.* **2016**, *6* (August), 1–12.

(132) Hecht, D. S.; Hu, L.; Irvin, G. Emerging Transparent Electrodes Based on Thin Films of Carbon Nanotubes, Graphene, and Metallic Nanostructures. *Adv. Mater.* **2011**, *23* (13), 1482–1513.

(133) Koo, B. R.; Oh, D. H.; Riu, D. H.; Ahn, H. J. Improvement of Transparent Conducting Performance on Oxygen-Activated Fluorine-Doped Tin Oxide Electrodes Formed by Horizontal Ultrasonic Spray Pyrolysis Deposition. *ACS Appl. Mater. Interfaces* **2017**, *9* (51), 44584–44592.

(134) Hagstrum, H. D. Metastable Ions of the Noble Gases. *Phys. Rev.* **1956**, *104* (2), 309–316.

(135) Shun'ko, E. V.; Belkin, V. S. Cleaning Properties of Atomic Oxygen Excited to Metastable State 2 S2 2 P4 (S1 0). *J. Appl. Phys.* **2007**, *102* (8).

(136) Berezhnoj, S. V.; Shin, C. B.; Buddemeier, U.; Kaganovich, I. Charged Species Profiles in Oxygen Plasma. *Appl. Phys. Lett.* **2000**, *77* (6), 800–802.

(137) Stoffels, E.; Stoffels, W. W.; Vender, D.; Kando, M.; Kroesen, G. M. W.; De Hoog, F. J. Negative Ions in a Radio-Frequency Oxygen Plasma. *Phys. Rev. E* **1995**, *51* (3), 2425–2435.

(138) Belostotsky, S. G.; Economou, D. J.; Lopaev, D. V.; Rakhimova, T. V. Negative Ion Destruction by O(3P) Atoms and O2(a 1Δg) Molecules in an Oxygen Plasma. *Plasma Sources Sci. Technol.* **2005**, *14* (3), 532–542.

(139) Kim, S. Y.; Hong, K.; Kim, K.; Yu, H. K.; Kim, W. K.; Lee, J. L. Effect of N2, Ar, and O2 Plasma Treatments on Surface Properties of Metals. *J. Appl. Phys.* **2008**, *103* (7), 1–4.

(140) Sun, H.; Zhou, Y.; Xin, Y.; Deng, K.; Meng, L.; Xiong, J.; Li, L. Composition and Energy Band–Modified Commercial FTO Substrate for In Situ Formed Highly Efficient Electron Transport Layer in Planar Perovskite Solar Cells. *Adv. Funct. Mater.* **2019**, *29* (11).

(141) Sun, H.; Zhou, Y.; Xin, Y.; Deng, K.; Meng, L.; Xiong, J.; Li, L. Composition and Energy Band–Modified Commercial FTO Substrate for In Situ Formed Highly Efficient Electron Transport Layer in Planar Perovskite Solar Cells. *Adv. Funct. Mater.* **2019**, *29* (11), 1–9.

(142) Fathil, M. F. M.; Adzhri, R.; Arshad, M. K. M.; Hashim, U.; Ruslinda, A. R.; Ayub, R. M.; Nuzaihan, M. N. M.; Azman, A. H.; Zaki, M. Preparation and Characterization of Titanium Dioxide Thin Film for Field-Effect Transistor Biosensor Application. *Proc. - 2015 2nd Int. Conf. Biomed. Eng. ICoBE 2015* **2015**, No. 1, 30–31.

(143) S. Hu; M. R. Shaner; J. A. Beardslee; M. Lichterman; B. S. Brunschwig; N. S. Lewis. Amorphous TiO2 Coatings Stabilize Si, GaAs, and GaP Photoanodes for Efficient Water Oxidation. *Science* **2014**, *344* (6187), 1005–1009.

(144) Li, M.; Li, X.; Li, W.; Meng, X.; Yu, Y.; Sun, X. Atomic Layer Deposition Derived Amorphous TiO2 Thin Film Decorating Graphene Nanosheets with Superior Rate Capability. *Electrochem. commun.* **2015**, *57*, 43–47.

(145) Dongale, T. D.; Shinde, S. S.; Kamat, R. K.; Rajpure, K. Y. Nanostructured TiO2 Thin Film Memristor Using Hydrothermal Process. *J. Alloys Compd.* **2014**, *593*, 267–270.

(146) Yu, J.; Zhao, X.; Zhao, Q. Effect of Surface Structure on Photocatalytic Activity of TiO2 Thin Films Prepared by Sol-Gel Method. *Thin Solid Films* **2000**, *379* (1–2), 7–14.

(147) Kawakami, R.; Yuasa, T.; Sato, Y.; Mori, Y. Effects of Particle Size on Properties of TiO 2 Nanoparticle Thin Films Deposited by Electrophoresis. **2013**, *566*, 199–203.

(148) Ye, T.; Xing, J.; Petrović, M.; Chen, S.; Chellappan, V.; Subramanian, G. S.; Sum, T. C.; Liu, B.; Xiong, Q.; Ramakrishna, S. Temperature Effect of the Compact TiO2 Layer in Planar Perovskite Solar Cells: An Interfacial Electrical, Optical and Carrier Mobility Study. *Sol. Energy Mater. Sol. Cells* **2017**, *163*, 242–249.

(149) Mercado, C. C.; Knorr, F. J.; McHale, J. L.; Usmani, S. M.; Ichimura, A. S.; Saraf, L. V. Location of Hole and Electron Traps on Nanocrystalline Anatase TiO2. *J. Phys. Chem. C* **2012**, *116* (19), 10796–10804.

(150) Zhang, Z.; Yates Jr., J. T. Direct Observation of Surface-Mediated Electron-Hole Pair Recombination in TiO2 (110). *J. Phys. Chem. C* **2010**, *114* (7), 3098–3101.

(151) Xing, G.; Wu, B.; Chen, S.; Chua, J.; Yantara, N.; Mhaisalkar, S.; Mathews, N.; Sum, T. C. Interfacial Electron Transfer Barrier at Compact TiO2CH3NH3PbI3 Heterojunction. *Small* **2015**, *11* (29), 3606–3613.

(152) Hermes, I. M.; Hou, Y.; Bergmann, V. W.; Brabec, C. J.; Weber, S. A. L. The Interplay of Contact Layers: How the Electron Transport Layer Influences Interfacial Recombination and Hole Extraction in Perovskite Solar Cells. *J. Phys. Chem. Lett.* **2018**, *9* (21), 6249–6256.

(153) Olthof, S.; Meerholz, K. Substrate-Dependent Electronic Structure and Film Formation of MAPbI 3 Perovskites. *Nat. Publ. Gr.* **2017**, *7*, 1–10.

(154) Ma, X.; Tang, P.; Liu, D.; Wu, L.; Zhang, J.; Feng, L. Interface Engineering of Perovskite Solar Cells with Air Plasma Treatment for Improved Performance. *ChemPhysChem* **2017**, *18* (20), 2939–2946.

(155) Liu, G.; Yang, B.; Liu, B.; Zhang, C.; Xiao, S.; Yuan, Y.; Xie, H.; Niu, D.; Yang, J.; Gao, Y.; et al. Irreversible Light-Soaking Effect of Perovskite Solar Cells Caused by Light-Induced Oxygen Vacancies in Titanium Oxide. *Appl. Phys. Lett.* **2017**, *111* (15), 1–6.

(156) Cojocaru, L.; Uchida, S.; Sanehira, Y.; Nakazaki, J.; Kubo, T.; Segawa, H. Surface Treatment of the Compact TiO2 Layer for Efficient Planar Heterojunction Perovskite Solar Cells. *Chem. Lett.* **2015**, *44* (5), 674–676.

(157) Ke, W.; Fang, G.; Wan, J.; Tao, H.; Liu, Q.; Xiong, L.; Qin, P.; Wang, J.; Lei, H.; Yang, G.; et al. Efficient Hole-Blocking Layer-Free Planar Halide Perovskite Thin-Film Solar Cells. *Nat. Commun.* **2015**, *6*, 6700.

(158) Kim, I. S.; Haasch, R. T.; Cao, D. H.; Farha, O. K.; Hupp, J. T.; Kanatzidis, M. G.; Martinson, A. B. F. Amorphous TiO2 Compact Layers via ALD for Planar Halide Perovskite Photovoltaics. *ACS Appl. Mater. Interfaces* **2016**, *8* (37), 24310–24314.

(159) Chong, H. Y.; Lee, S. H.; Kim, T. W. Effect of an Ultraviolet-Ozone Treatment on the Electrical Properties of Titanium-Oxide Thin-Film Transistors Fabricated by Using a Sol-Gel Process. *J. Electrochem. Soc.* **2012**, *159* (7), B771–B774.

(160) Yu, W.; Liu, X.; Pan, L.; Li, J.; Liu, J.; Zhang, J.; Li, P.; Chen, C.; Sun, Z. Enhanced Visible Light Photocatalytic Degradation of Methylene Blueby F-Doped TiO 2. *Appl. Surf. Sci.* **2014**, *319* (1), 107–112.

(161) Chen, X.; Liu, L.; Huang, F. Black Titanium Dioxide (TiO2) Nanomaterials. *Chem. Soc. Rev.* **2015**, *44* (7), 1861–1885.

(162) Nowotny, M. K.; Bak, T.; Nowotny, J. Electrical Properties and Defect Chemistry of TiO $_2$ Single Crystal. I. Electrical Conductivity †. *J. Phys. Chem. B* **2006**, *110* (33), 16270–16282.

(163) Henderson, M. A. A Surface Perspective on Self-Diffusion in Rutile TiO2. *Surf. Sci.* **1999**, *419* (2–3), 174–187.

(164) Miller, D. J.; Biesinger, M. C.; McIntyre, N. S. Interactions of CO2 and CO at Fractional Atmosphere Pressures with Iron and Iron Oxide Surfaces: One Possible Mechanism for Surface Contamination? *Surf. Interface Anal.* **2002**, *33* (4), 299–305.

(165) Petrik, N. G.; Zhang, Z.; Du, Y.; Dohna, Z.; Lyubinetsky, I.; Kimmel, G. A. Chemical Reactivity of Reduced TiO 2 (110): The Dominant Role of Surface Defects in Oxygen Chemisorption. **2009**, *2* (110), 12407–12411.

(166) Jensen, S. A. Charge Carrier Dynamics in Photovoltaic Materials, Universiteit van Amsterdam, 2014.

(167) Grätzel, M.; Hagfeldt, A.; Saliba, M.; Tress, W.; Correa-Baena, J.-P.; Abate, A.; Buonassisi, T. Promises and Challenges of Perovskite Solar Cells. *Science* **2017**, *358*

(6364), 739–744.

(168) Yeo, J.; Choi, M. J.; Kim, D. S. Robust Hydrophobic Surfaces with Various Micropillar Arrays. *J. Micromechanics Microengineering* **2010**, *20* (2).

(169) Li, M.; Cushing, S. K.; Wu, N. Plasmon-Enhanced Optical Sensors: A Review. *Analyst* **2015**, *140* (2), 386–406.

(170) Elbersen, R.; Vijselaar, W.; Tiggelaar, R. M.; Gardeniers, H.; Huskens, J. Fabrication and Doping Methods for Silicon Nano- and Micropillar Arrays for Solar-Cell Applications: A Review. *Adv. Mater.* **2015**, *27* (43), 6781–6796.

(171) Liang, H.; Zhu, R.; Dong, Y.; Wu, S.-T.; Li, J.; Wang, J.; Zhou, J. Enhancing the Outcoupling Efficiency of Quantum Dot LEDs with Internal Nano-Scattering Pattern. *Opt. Express* **2015**, *23* (10), 12910.

(172) Papageorgiou, A. C.; Beglitis, N. S.; Pang, C. L.; Teobaldi, G.; Cabailh, G.; Chen, Q.; Fisher, A. J.; Hofer, W. A.; Thornton, G. Electron Traps and Their Effect on the Surface Chemistry of TiO2(110). *Proc. Natl. Acad. Sci.* **2010**, *107* (6), 2391–2396.

(173) Du, Y.; Kumar, A.; Pan, H.; Zeng, K.; Wang, S.; Yang, P.; Wee, A. T. S. The Resistive Switching in TiO 2 Films Studied by Conductive Atomic Force Microscopy and Kelvin Probe Force Microscopy. *AIP Adv.* **2013**, *3* (8).

(174) Armstrong, N. R.; Lin, A. W. C.; Fujihira, M.; Kuwana, T. Electrochemical and Surface Characteristics of Tin Oxide and Indium Oxide Electrodes. *Anal. Chem.* **1976**, *48* (4), 741–750.

(175) Korotchenkov, G.; Brynzari, V.; Dmitriev, S. Electrical Behavior of SnO2 Thin Films in Humid Atmosphere. *Sensors Actuators, B Chem.* **1999**, *54* (3), 197–201.

(176) Boyle, J. F.; Jones, K. A. The Effects of CO, Water Vapor and Surface Temperature on the Conductivity of a SnO2 Gas Sensor. *J. Electron. Mater.* **1977**, *6* (6), 717–733.

(177) Garcia, R.; Knoll, A. W.; Riedo, E. Advanced Scanning Probe Lithography. *Nat. Nanotechnol.* **2014**, *9* (8), 577–587.

(178) Garcia, R.; Martinez, R. V.; Martinez, J. Nano-Chemistry and Scanning Probe Nanolithographies. *Chem. Soc. Rev.* **2006**, *35* (1), 29–38.

(179) Blanco, E. M.; Nesbitt, S. A.; Horton, M. A.; Mesquida, P. A Multiprotein Microarray on Silicon Dioxide Fabricated by Using Electric-Droplet Lithography. *Adv. Mater.* **2007**, *19* (18), 2469–2473.

(180) Korjenic, A.; Raja, K. S. Electrochemical Stability of Fluorine Doped Tin Oxide (FTO) Coating at Different PH Conditions. *J. Electrochem. Soc.* **2019**, *166* (6), C169–C184.

(181) Feng, H. Electrochemically Reduced Polycrystalline Tin Oxide Thin Films. *J. Electrochem. Soc.* **2006**, *143* (6), 2048.

(182) Major, S.; Kumar, S.; Bhatnagar, M.; Chopra, K. L. Effect of Hydrogen Plasma Treatment on Transparent Conducting Oxides. *Appl. Phys. Lett.* **1986**, *49* (7), 394–396.

(183) Kahn, A. Fermi Level, Work Function and Vacuum Level. *Mater. Horizons* **2016**, *3* (1), 7–10.

(184) Sugiyama, K.; Ishii, H.; Ouchi, Y.; Seki, K. Dependence of Indium-Tin-Oxide Work Function on Surface Cleaning Method as Studied by Ultraviolet and x-Ray Photoemission Spectroscopies. *J. Appl. Phys.* **2000**, *87* (1), 295–298.

(185) Gubbala, S.; Chakrapani, V.; Kumar, V.; Sunkara, M. K. Band-Edge Engineered Hybrid Structures for Dye-Sensitized Solar Cells Based on SnO2 Nanowires. *Adv. Funct. Mater.* **2008**, *18* (16), 2411–2418.

(186) Jiang, L.; Yu, H.; Shi, L.; Zhao, Y.; Wang, Z.; Zhang, M.; Yuan, S. Optical Band Structure and Photogenerated Carriers Transfer Dynamics in FTO/TiO2 Heterojunction Photocatalysts. *Appl. Catal. B Environ.* **2016**, *199*, 224–229.

(187) Leon O. Chua. Memristor. *IEEE Trans. Circuit Theory,* **1971**, *CT-18* (5), 507–519.

(188) Strukov, D. B.; Snider, G. S.; Stewart, D. R.; Williams, R. S. The Missing Memristor Found. *Nature* **2008**, *453* (7191), 80–83.

(189) Sarwar, S. S.; Saqueb, S. A. N.; Quaiyum, F.; Rashid, A. B. M. H. U. Memristor-Based Nonvolatile Random Access Memory: Hybrid Architecture for Low Power Compact Memory Design. *IEEE Access* **2013**, *1* (January), 29–34.

(190) Shi, T.; Yin, X. B.; Yang, R.; Guo, X. Pt/WO 3 /FTO Memristive Devices with Recoverable Pseudo-Electroforming for Time-Delay Switches in Neuromorphic Computing. *Phys. Chem. Chem. Phys.* **2016**, *18* (14), 9338–9343.

(191) Kim, Y.; Jang, J. H.; Park, S. J.; Jesse, S.; Donovan, L.; Borisevich, A. Y.; Lee, W.; Kalinin, S. V. Local Probing of Electrochemically Induced Negative Differential Resistance in TiO2memristive Materials. *Nanotechnology* **2013**, *24* (8).

(192) Han, J. B.; Wang, X.; Wang, N.; Wei, Z. H.; Yu, G. P.; Zhou, Z. G.; Wang, Q. Q. Effect of Plasma Treatment on Hydrophilic Properties of TiO2 Thin Films. *Surf. Coatings Technol.* **2006**, *200* (16–17), 4876–4878.

List of Figures